

# ABSTRACT

TYLER II, TALMAGE. Characterization of Isolated Nanodiamond Particles. (Under the direction of Dr. John J. Hren)

As the use of materials of increasingly smaller dimensions grows, for applications ranging from electronics to micro-electromechanical systems, so does the need to better understand the properties of materials at these small scales. Technology is driven towards the use of *the small*, and nano-scale materials will soon become standard. Methods to study materials of nanometer scale dimensions are thus necessary to better understand and exploit materials at the nanoscale.

The focus of this work was to demonstrate a technique for the isolation and characterization of nanometer-sized particles of diamond. In order to effectively study nanoscale amounts of diamond using a number of characterization techniques, a system had to be developed that allowed for 1) nanoscale amounts of diamond to be isolated and 2) these samples to be transferred to and from various systems (e.g. field emission vacuum system, electron microscope, etc.) for characterization. This was accomplished using ultra-sharp metal needles (curvature radii less than 100nm; both molybdenum and aluminum were used) as substrates onto which nanodiamond particles were deposited using electrophoresis. This technique yielded isolated diamond particles on *the tips of needles*. The *needle* is an ideal sample geometry for a number of characterization techniques, including transmission electron microscopy (TEM), field emission, and field emission microscopy (FEM), all of which were employed in this study, along with electron energy

loss spectrometry (EELS), scanning electron microscopy (SEM), and x-ray energy dispersive spectroscopy (EDS).

An isolated nanodiamond particle (~3 nm in size) was deposited on the tip of a molybdenum needle. Field emission current versus voltage measurements were taken from the isolated diamond particle and compared to that of the bare molybdenum needle and the same needle with a thicker *coating* of nanodiamond particles. Furthermore, transmission electron microscopy and electron energy loss spectrometry were used to investigate both the morphology and composition of the diamond. The diamond was determined to be *pure* (free of any non-diamond carbon phase, i.e. graphite) and its size was accurately determined. The field emission behavior observed from the isolated diamond particle, termed the *anomalous thickness effect*, was described as being a result of size-dependent materials properties (namely bandgap increase due to quantum effects) and size-dependent electrostatic effects.

Additional diamond deposition experiments were carried out using aluminum substrates, yielding promising results. The aluminum needles were capable of serving as field emission cathodes, allowing for more than one microamp of current to be extracted from the aluminum without tip failure. Furthermore, diamond nanoparticles were deposited in varying amounts and characterized, similar to the experiments using molybdenum.

**CHARACTERIZATION OF ISOLATED  
NANODIAMOND PARTICLES**

by

**TALMAGE TYLER II**

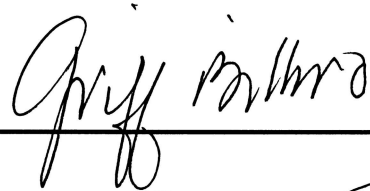
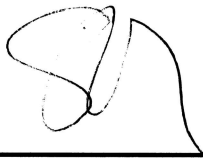
A dissertation submitted to the Graduate Faculty of  
North Carolina State University  
in partial fulfillment of the  
requirements for the Degree of  
Doctor of Philosophy

**MATERIALS SCIENCE AND ENGINEERING**

Raleigh

2004

**APPROVED BY:**



Chair of Advisory Committee



## **BIOGRAPHY**

Talmage Tyler II was born in Charlotte, North Carolina in 1977. He received his Bachelor of Science in physics from the University of North Carolina at Chapel Hill in 1999 and was married to Hope Greene that same year. He then moved to Raleigh and enrolled in North Carolina State University to pursue the degree of Doctor of Philosophy in Materials Science and Engineering. He and Hope have a son, Trey.

## ACKNOWLEDGMENTS

I thank Dr. John Hren for his guidance and countless discussions while serving as my thesis advisor; his knowledge and experience have been great assets. My sincere thanks also go to Dr. Victor Zhirnov for his enthusiasm for research, his passion for exploring the unknown, and his constant eagerness for scientific discussion. I thank Dr. Zlatko Sitar and Dr. Griff Bilbro for serving as my committee members and I thank Dr. Klaus Bachmann for sharing his expertise in electrochemistry. I also wish to thank Dr. Alex Kvit for his assistance with TEM, and my fellow research group members: David Jaeger and Danielle Elswick.

My most heartfelt thanks go to my wife, Hope, for her patience and support. Finally, I wish to express my deepest appreciation to my father, who has been a constant source of inspiration and encouragement.

# TABLE OF CONTENTS

	Page
List of Tables	vii
List of Figures	viii
<b>1. INTRODUCTION AND BACKGROUND</b>	<b>1</b>
1.1 Overview of Dissertation	1
1.2 Size Dependent Material Properties	2
1.3 Properties of Diamond	6
1.4 Field Electron Emission	8
1.5 Field Emission from Diamond	16
1.6 Summary	18
1.7 References	19
<b>2. SAMPLE PREPARATION</b>	<b>28</b>
2.1 Introduction	28
2.2 Etching	28
2.3 Diamond Deposition	36
2.4 Diamond Powder Characterization	43
2.5 Summary	46
2.6 References	48

<b>3. CHARACTERIZATION TECHNIQUES</b>	<b>51</b>
3.1 Introduction	51
3.2 Field Emission Measurements	53
3.3 Scanning Electron Microscopy	61
3.4 Field Emission Microscopy	61
3.5 Transmission Electron Microscopy	65
3.6 Electron Energy Loss Spectrometry	66
3.7 Summary	67
3.8 References	68
<b>4. NANODIAMOND ON MOLYBDENUM</b>	<b>70</b>
4.1 Abstract	70
4.2 Introduction	71
4.3 Experimental	72
4.4 Results	74
4.5 Discussion	77
4.6 Conclusion	85
4.7 References	87
<b>5. NANODIAMOND ON ALUMINUM</b>	<b>90</b>
5.1 Abstract	90
5.2 Introduction	91
5.3 Experimental	93

5.4	Results	94
5.5	Discussion	115
5.6	Conclusion	116
5.7	References	118
<b>6. SUMMARY, CONCLUSIONS, AND FUTURE WORK</b>		<b>120</b>
6.1	Summary and Conclusions	120
6.2	Suggested Future Work	121
6.3	References	124
<b>APPENDIX</b>		<b>125</b>

**LIST OF TABLES**

	Page
1.1 Summary of various properties of diamond.	7
2.1 Summary of various types of detonation-produced nanodiamond (reproduced from [14]).	38
4.1 Geometrical and emission characteristics of molybdenum field emitter with varying amounts of nanodiamond.	79
5.1 Comparison of physical properties of aluminum and aluminum oxide.	93
5.2 Geometrical and emission characteristics of aluminum field emitter with varying amounts of nanodiamond.	113
A.1 Summary of aluminum etching conditions and corresponding platinum deposition onto aluminum.	135

## LIST OF FIGURES

		Page
1.1	Bandgap as a function of size, Eqn. (1.1), for diamond with bulk bandgap of 5.4 eV, $m_e^*=0.2m_0$ , and $m_h^*=0.7 m_0$ .	5
1.2	Percent of atoms found at surface for spherical diamond particle.	6
1.3	Surface potential barrier for electrons in a metal.	9
1.4	Schematic of concentric sphere geometry for approximating field enhancement and a corresponding <i>real</i> tip-to-hemisphere geometry.	12
1.5	Plot of $g(\phi)$ illustrating maximum error of 10% in the range of 3.5-11.5 eV.	15
2.1	Schematic of electrochemical etching of metal wire to form sharp needles.	30
2.2	Scanning electron micrographs of several molybdenum samples etched under identical conditions, but yielding varying results.	32
2.3	Scanning electron micrograph of etched molybdenum wire illustrating the formation of oxide.	33
2.4	X-ray energy-dispersive spectrum taken from sample in Figure 2.3. Oxygen peaks indicate oxide formation, while potassium is residue (from etching in KOH) trapped in the cracked oxide.	34
2.5	Current-voltage measurements for an aluminum field emitter. Maximum current exceeded one microamp (failure occurred at ~5 microamps).	35
2.6	Schematic of electrophoretic deposition of diamond nanoparticles via	38

	pulsed bias.	
2.7	Scanning electron micrographs of four molybdenum needles with varying amounts of nanodiamond deposits. The four samples were coated using identical parameters except for number of pulses; the top 2 samples underwent 10 pulses (1ms at +5V), while the bottom 2 samples underwent ~1000 pulses (1ms at +5V).	39
2.8	Transmission electron micrographs of several different molybdenum samples illustrating the deposition of nanodiamond particles on the surface, both isolated particles and agglomerates are seen.	40
2.9	Scanning electron micrograph of diamond-coated array of silicon tips (inset shows array at lower magnification).	41
2.9	Current-voltage data taken from an un-coated silicon array ( <i>untreated</i> ) and the same array coated with nanodiamond ( <i>treated</i> ).	41
2.11	Transmission electron micrograph of nanodiamond powder.	45
2.12	Electron energy loss spectrum taken from nanodiamond powder imaged in Figure 2.11. Shoulder at ~287 eV indicates presence of $sp^2$ bonding, while peaks from ~290 eV to ~340 eV are characteristic of diamond bonding ( $sp^3$ ).	46
3.1	Flowchart illustrating the arbitrary order in which the various characterization techniques can be performed.	53
3.2	Schematic of <i>diode</i> configuration of field emission measurement setup.	56
3.3	Field emission current voltage curves calculated for various values of	57

	resistance in series. Significant deviations from the ideal (zero resistance) do not occur for a resistance less than 10 Mega Ohms.	
3.4	Molybdenum field emission tip after undergoing irreversible damage (generation of excessive heat at high current densities melted the emitter).	58
3.5	Field emission <i>break-in</i> period for a molybdenum field emitter.	59
3.6	Schematic of vacuum chamber and components used for field emission and field emission microscopy measurements.	60
3.7	Schematic of field emission microscope, indicating emitter, bias, and imaging screen.	62
3.8	Schematic of custom sample holder used for non-destructive TEM analysis of needle-shaped field emitters.	65
4.1	High-resolution transmission electron micrograph of an isolated nanoparticle of diamond on the surface of a molybdenum tip of radius of curvature $r=50\text{nm}$ .	73
4.2	EELS spectrum of nanodiamond particles, compared to standard carbon reference spectrum.	75
4.3	Field emission characteristics from a bare metal tip (i), the tip with a single nanodiamond particle (ii), and the same tip with a nanodiamond film (iii). Inset: schematic of tip-to-anode geometry.	77
4.4	Energy band diagram for a nanometer-size semiconductor; ground state and first excited state for holes and electrons are illustrated	81

- schematically. The increase in bandgap due to quantum confinement effects is shown.
- 4.5 Ideal field emission current from two hypothetical emitters differing only 82  
by their emission barriers, i) 4 eV and ii) 4.7 eV.
- 4.6 Surface electrostatic field profile (top) computed for a *particle-on-tip* 84  
geometry (bottom) indicating the reduction of fields due to *screening*  
effects. Fields are plotted for a) particle-vacuum, b) metal-vacuum, and  
c) metal-particle interfaces.
- 5.1 Transmission electron micrograph of electrochemically etched aluminum 97  
needle after field emission.
- 5.2 Scanning electron micrograph of aluminum needle with 98  
electrophoretically deposited nanodiamond.
- 5.3 Transmission electron micrograph of aluminum needle with 100  
electrophoretically deposited nanodiamond. Inset marks areas where  
higher magnification images were taken, which correspond to the  
micrographs in Figure 5.4.
- 5.4 Transmission electron micrographs of diamond-deposited aluminum 100  
needle, corresponding to areas marked in the inset in Figure 5.3.
- 5.5 Transmission electron micrograph of aluminum needle after undergoing 101  
nanodiamond deposition and field emission. Labels indicate areas where  
higher magnification images were taken, which correspond to the  
micrographs in Figures 5.6 and 5.7.

5.6	Transmission electron micrographs corresponding to areas (a) – (d) marked on the image in Figure 5.5.	102
5.7	Transmission electron micrographs corresponding to areas (e) – (h) marked on the image in Figure 5.5.	103
5.8	Electron energy loss (core loss) from platinum nanoparticles in Figure 5.5. Experimental data and reference spectrum are plotted.	104
5.9	X-ray energy-dispersive spectrum taken from aluminum needle after field emission (sample in Figure 5.5). Presence of platinum is apparent; inset: spectrum normalized to height of aluminum peak.	105
5.10	Transmission electron micrograph of aluminum emitter following a second diamond deposition and field emission. Labels indicate areas where higher magnification images were taken, which correspond to the micrographs in Figure 5.11.	106
5.11	Transmission electron micrographs corresponding to areas (a) – (c) marked on the image in Figure 5.10.	107
5.12	Transmission electron micrograph of the apex of the needle seen in Figure 5.10. The presence of a thin diamond <i>film</i> (~6-8 nm) is apparent.	108
5.13	Field emission current voltage measurements taken from an aluminum emitter before and after diamond deposition: i) bare aluminum, ii) single deposition, and iii) two depositions.	111
5.14	Field emission microscopy images taken from aluminum emitter a) before diamond deposition (Figure 5.1), b) after diamond deposition	112

- (Figures 5.3 and 5.5), and c) after a second diamond deposition (Figure 5.12).
- 5.15 Comparison of change in emission parameters (relative to bare metal emitter) for molybdenum emitter with diamond (data from table 4.1) and aluminum emitter with diamond (data from table 5.2). Depositions are as follows: 0 = bare metal emitter, 1 = single diamond coating (isolated nanoparticle(s)), and 2 = thin diamond *film*. Emission parameters considered are: threshold voltage (“ $V_{th}$ ”), emission barrier (“ $\phi$ ”), and integral transconductance (“ $g$ ”). 114
- A.1 X-ray energy-dispersive spectrum taken from an *as prepared* aluminum needle (electrochemically etched, with no field emission or diamond deposition). Presence of platinum is apparent; inset: spectrum normalized to height of aluminum peak. . 128
- A.2 Scanning electron micrograph of *pulsed DC-etched* (AC bias half-wave rectified) aluminum wire. The “+” symbol indicates region from which energy dispersive x-ray spectrum was taken (Figure A.4), region enclosed by rectangle indicates where higher magnification image was taken (Figure A.3). 129
- A.3 Scanning electron micrograph of region denoted in Figure A.2. The “+” symbol indicates region from which energy dispersive x-ray spectrum was taken (Figure A.5). 130
- A.4 Energy dispersive x-ray spectrum taken from region marked by “+” in 131

- Figure A.2, aluminum peak (1.5 keV) is the only feature observed. Vertical axis is scaled to illustrate the absence of a weak platinum peak; inset: spectrum normalized to height of aluminum peak.
- A.5 Energy dispersive x-ray spectrum taken from region marked by “+” in 132  
Figure A.3, aluminum peak (1.5 keV) is the dominant feature; a very weak oxygen peak (0.5 keV) from aluminum-oxide is also seen. Vertical axis is scaled to illustrate the absence of a weak platinum peak; inset: spectrum normalized to height of aluminum peak.
- A.6 Scanning electron micrograph of aluminum wire electrochemically 133  
etched using *AC* bias followed by a *pulsed DC* etch (half-wave rectified). The “+” symbol indicates region from which energy dispersive x-ray spectrum was taken (Figure A.7).
- A.7 Energy dispersive x-ray spectrum taken from region marked by “+” in 134  
Figure A.6, aluminum peak (1.5 keV) is the dominant feature; a very weak oxygen peak (0.5 keV) from aluminum-oxide is also seen. Vertical axis is scaled to illustrate the absence of a weak platinum peak; inset: spectrum normalized to height of aluminum peak.

# CHAPTER 1

## INTRODUCTION AND BACKGROUND

### 1.1 OVERVIEW OF DISSERTATION

The chief goal of the work contained within this thesis is to examine the properties of diamond of nanometer-scale dimensions. The motivation for this study originated in the context of optimizing vacuum microelectronic performance, but has broader implications, as nanoscale materials are attracting increasing attention in numerous fields. The research that lead up to the current study of nanodiamond began with work on silicon arrays, a collaboration between N.C. State University and MCNC; in a natural progression to improve field emission properties, various coatings were investigated, including SiC, diamond (deposited via plasma techniques), and diamond powders; references 1-13 summarize these developments. The use of diamond coatings for improving field emitter performance eventually evolved into the use of field emitters as *tools* with which to study nanoscale amounts of diamond, the idea upon which this research is based.

The bulk properties of diamond, being well known and quite unique, have made it a popular candidate for use in vacuum microelectronics; in particular, it's electronic properties combined with its thermal and chemical properties have generated much interest in the use of diamond films for coating field emission cathodes. The nature of diamond films used as coatings, being multi-crystalline complex structures with grain boundaries

and non-diamond (e.g. graphite) inclusions, makes a fundamental understanding of the specific properties of the diamond, and how those properties affect cathode performance, extremely difficult. One purpose of this work is thus to isolate *minimal* amounts of *pure* diamond with less complex structures for characterization and study; and furthermore, to compare these results with those from larger amounts of diamond.

In order to effectively study nanoscale amounts of diamond using a number of characterization techniques, a system must be developed that allows for 1) nanoscale amounts of diamond to be isolated 2) these samples to be transferred to and from various systems (e.g. field emission vacuum system, electron microscope, etc.) for characterization. These requirements were met using ultra-sharp (curvature radii less than 100nm) metal needles as substrates, onto which nanodiamond was deposited via electrophoresis from a suspension of nanodiamond powder in ethanol.

## **1.2 SIZE DEPENDENT MATERIAL PROPERTIES**

The electronic properties that distinguish one material from another (e.g. bandgap or dielectric constant) and determine a given material's usefulness in applications and devices are a result of the bulk band structure of the material. However, as material dimensions approach the nanometer scale, the *rules* of the bulk regime no longer apply. At sufficiently small sizes (~5nm), quantized motion of electrons (and holes) becomes apparent, resulting in changes in material properties when compared to those of the bulk.

Consider the bandgap of a material; by definition, the bandgap is the energy needed to create an electron-hole pair separated by a sufficient distance so that Coulomb interaction is negligible. For a bulk material, this is a constant value  $E_g$ . However, as

dimensions decrease, the lattice can no longer be considered *infinite*; that is, electrons (and holes) in the lattice will begin to *see* the finite size of the material (i.e. the abrupt change in potential at the surface). The effect of size on the bandgap of a material can be described by the effective mass approximation, where the band structure is approximated by two opposing potential square-wells (one for electrons and one for holes) separated by an energy  $E_{g,confined}$ . As size decreases, the *walls* of the square well confine the electrons and holes, the result is an increase in the minimum energy allowed for electrons (and a decrease for holes) and as a result an increase in the bandgap energy [14,15]; the size dependent bandgap for a spherically symmetric particle is described as follows:

$$E_{g,confined} = E_{g,bulk} + \frac{\hbar^2 \pi^2}{2R^2} \left[ \frac{1}{m_e^*} + \frac{1}{m_h^*} \right] \quad (1.1)$$

where R is the radius of the spherical particle. Equation (1.1) considers only kinetic energy shifts, neglecting Coulomb interactions and polarization, which will cause further (although smaller) shifts in the bandgap [15]. Clearly, the bandgap will increase at sufficiently small sizes as illustrated in Figure 1.1. Although Equation (1.1) illustrates the increase in bandgap as a function of size, which has been demonstrated experimentally [16-20], it has limited applicability when used quantitatively [21]. Clearly, as R decreases to the lower limit (the radius of a single atom), the *bandgap* would equal the ionization energy of the atom.

It is also important to note that the effective mass approximation (even when considering Coulomb and polarization effects) does not include effects due to

rearrangement of surface atoms. At nanometer scales, the surface becomes more important due to the fact that an increasingly larger percentage of atoms appear at the surface, which affects the entire band structure of the nano-solid [22]. For example, the percent of surface atoms is significant for a spherical diamond particle with diameter less than 10nm (Figure 1.2). It is apparent that determining material properties at such small scales requires intimate knowledge of the surface.

Other properties known to vary with size include electron affinity [14], dielectric constant [23-26], as well as other physical properties such as melting point and hardness [18]. It is therefore not simply desired, but necessary, that characterization be done at the sub-nanometer scale when materials of interest are on the order of only a few nanometers in size.

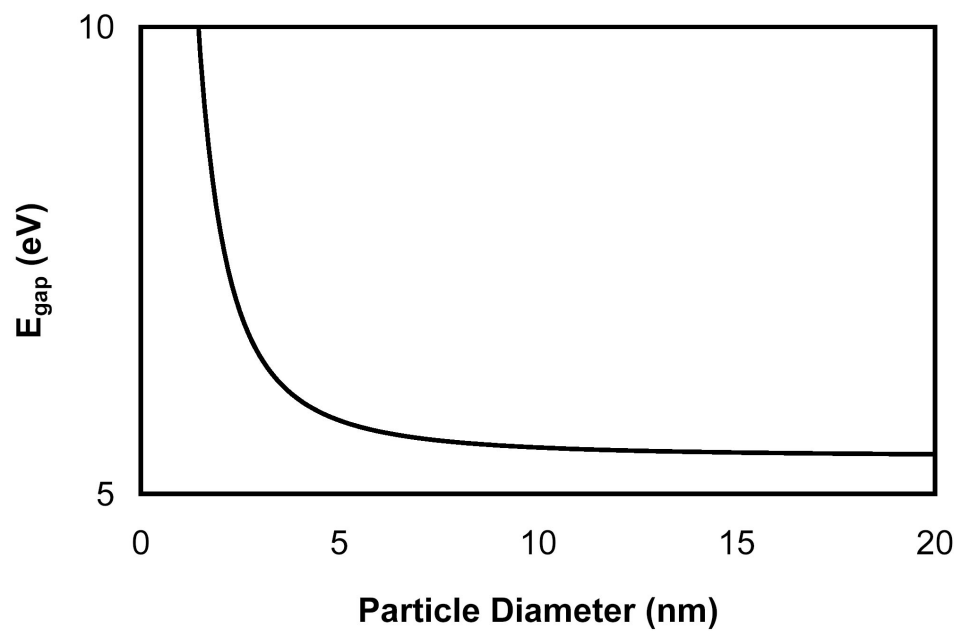


**FIGURE 1.1** Bandgap as a function of size, Eqn. (1.1), for diamond with bulk bandgap of 5.4 eV,  $m_e^*=0.2m_0$ , and  $m_h^*=0.7 m_0$ .

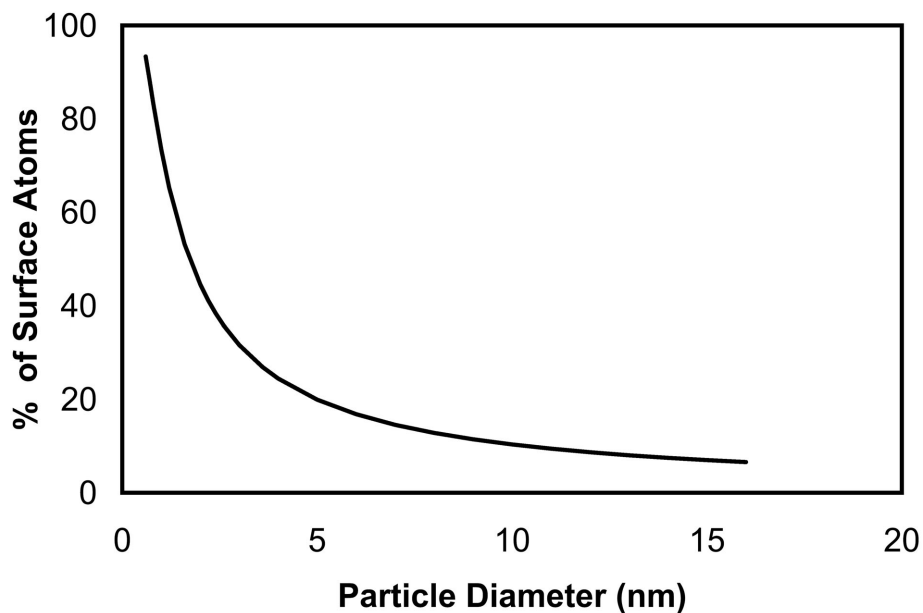


**FIGURE 1.2** Percent of atoms found at surface for spherical diamond particle.

### 1.3 PROPERTIES OF DIAMOND

Diamond is the hardest material in nature and has a high elastic modulus [27,28]. It has a high resistivity, while having high thermal conductivity and a low thermal expansion coefficient. Diamond is also extremely inert, chemically, making it resistant to most chemical attacks [28]. A summary of the properties of bulk diamond is given in Table 1.1 [27-31].

**Table 1.1** Summary of various properties of diamond.

<b>Property</b>	<b>Value</b>	<b>Units</b>
Hardness	10	Mohs scale
Young's Modulus	$10.5 \cdot 10^{11}$	N/m <sup>2</sup>
Density	3.52	g/cm <sup>3</sup>
Unit Cell Spacing	0.3567	nm
Nearest Neighbor	0.1545	nm
Thermal Conductivity	20	W/K/cm
Thermal Expansion Coeff.	$0.8 \cdot 10^{-6}$ (298K)	1/K
Dielectric Constant	5.7	-----
Bandgap	5.45	eV
Resistivity	$>10^{16}$	Ohm·cm

The unique properties of diamond (e.g. hardness and high thermal conductivity) are what make it so attractive for industrial uses such as grinding, sawing, and drilling [28]; in recent years it has been the unique combinations of properties that have made diamond attractive to the electronics community (e.g. high resistivity with high thermal conductivity) [32-34]. Applications ranging from heat sinks to vacuum microelectronic field emitters have been demonstrated [35-39]. Furthermore, with recent progress in the development of micro-electromechanical systems (MEMS), the exploitation of diamond for improved electrical, mechanical, and chemical behavior continues [32,40]. However, with application dimensions shrinking down to the nanometer scale, changes in the physical and electrical properties of materials occur. Bulk values for bandgap, resistivity, dielectric constant, thermal conductivity, etc. can change significantly as dimensions approach a few nanometers. It is therefore necessary to better understand material properties as a function of size if successful use of nanoscale materials is to be made. Such

size dependent studies can be extended to other nanoscale materials systems such as carbon nanotubes and similar structures (nano-wires, etc), which currently receive a great deal of attention in scientific and engineering communities.

## 1.4 FIELD ELECTRON EMISSION

### 1.4.1 Surface Barrier

Electrons within a metal are bound at the surface by an energy barrier  $\phi$ , known as the work function. In order for electrons to escape into vacuum, this barrier must be overcome. An electron can acquire enough energy to surmount the work function by several means, including thermal energy (thermionic emission), electromagnetic energy (photoemission), and kinetic energy (secondary electron emission). The square shape of the surface barrier (Figure 1.3) is a simplification; in reality the presence of the *image potential* causes the surface barrier to be *smoother*. When an electron is near the surface of a metal it experiences what is known as the *image force*. The image force is the attractive force felt by an electron near (at distance  $z$ ) a metal surface [41,42].

$$f = \frac{-e^2}{4\pi(2z)^2 \epsilon_0} \quad (1.2)$$

where  $e$  is the electron charge and  $\epsilon_0$  is the permittivity of free space. The energy of an electron transferred from infinity to a distance  $z$  from the surface is given by

$$E(x) = \int_z^{\infty} f \cdot dx = -\frac{e^2}{16\pi\epsilon_0 z} \quad (1.3)$$

In the presence of an electric field  $F$ , the total surface potential for an electron at a metal surface is

$$V(z) = \phi - \frac{e^2}{16\pi\epsilon_0 z} - eFz \quad (1.4)$$

Equation (1.4) is generally accepted to be valid in the range of  $z > 3\text{\AA}$  [43].

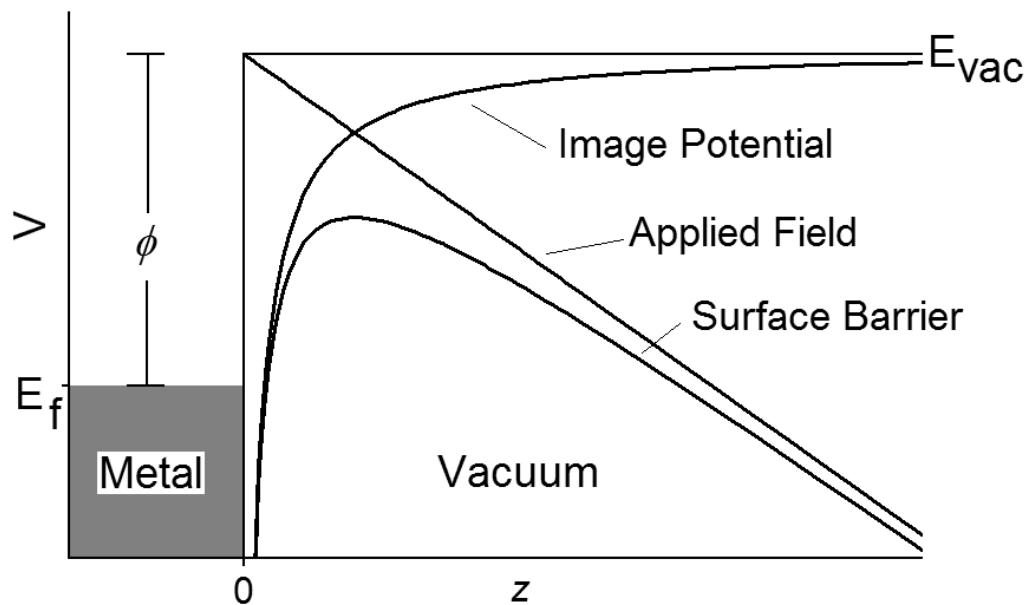


**Figure 1.3** Surface potential barrier for electrons in a metal.

### 1.4.2 Field Emission Current

When under the influence of an intense electric field, the surface barrier for electrons in a metal can be sufficiently distorted from the unperturbed state (see Figure 1.3), allowing for the tunneling of electrons from the surface into the vacuum. Fowler and Nordheim derived an expression that relates the applied electric field to the current density of electrons extracted from a planar metal electrode subjected to the field [44]. Electron emission from the metal surface into the vacuum can be described by considering two terms: 1) the supply of electrons to the surface and 2) the emission probability of an electron at the surface. The number of electrons impinging the surface is described by the *electron supply function*,  $N(E,T)$ , which depends on the electron energy and temperature. Emission probability,  $D(E,F)$ , is a function of the incident electron energy,  $E$ , and the electric field,  $F$  (which in turn determines the shape of the surface barrier). The number of electrons per unit area per time (i.e. the current density) is thus expressed as [43]

$$j(F,T) = e \int N(E,T)D(E,F)dE \quad (1.5)$$

For the above integral to be solved in closed form, it is necessary to make the *zero K* approximation, which assumes the energy distribution of electrons to be the same as that at 0 degrees Kelvin. The 0K approximation is acceptable for most metals, where  $\phi \sim 4-6\text{eV} \gg kT$  [43]. With the integral now solvable, the current density equation becomes

$$J = \frac{e^3}{8\pi h} \cdot \frac{F^2}{\phi t^2(y)} \exp\left(-\frac{8\pi(2m)^{1/2}}{3eh} \cdot \frac{\phi^{3/2}}{F} v(y)\right) \quad (1.6)$$

in amps per square meter, where  $t^2(y) \approx 1.1$  and  $v(y) \approx 0.95 - y^2$ , with  $y = (e^3 F / 4\pi\epsilon_0)^{1/2} / \phi$  [43,45,46]. With constants defined as

$$A = \frac{e^3}{8\pi h}, \quad B = \frac{8\pi(2m)^{1/2}}{3eh} \quad (1.7)$$

the current density can be rewritten as

$$J = \frac{A}{1.1\phi} \exp\left(\frac{9.84}{\phi^{1/2}}\right) F^2 \exp\left(-\frac{(.95)B\phi^{3/2}}{F}\right) \quad (1.8)$$

Experimentally, however, it is usually current that is measured as a function of applied voltage, rather than current density versus electric field. Therefore, it is convenient to define the electric field in terms of applied voltage. This requires knowledge about the geometry of the experimental setup.

### 1.4.3 Geometric Field Enhancement

In practice, there are two basic shapes of field emission devices, planar and pointed [47]. In order to produce electric fields of sufficient magnitude ( $\sim 5\text{V/nm}$  or  $5 \cdot 10^7\text{V/cm}$ ) to extract measurable current from materials with work functions of four to five electron volts, it is usually necessary to take advantage of geometrical field enhancement. The use of *needle* shaped emitters allows for substantial field enhancement at the apex of the tip.

The use of planar emitters, with very small tip-to-anode spacing to achieve high fields, has been demonstrated with little success. Planar emitters suffer from several inherent problems; they are not designed to offer geometric field enhancement and are thus subject to extremely irregular emission areas and non-uniform emission sights, for example due to *protrusions*; and the relatively large areas over which emission can occur make determination of variables such as work function, surface/interface roughening, and adsorbates more difficult. Furthermore, planar emitters are in fact not perfect planes; there exist natural variations in surface topology (i.e. roughness), which affect emission and complicate interpretation of emission data. Pointed emitters, whose geometry ensures the maximum field at the tip apex, are preferred because local fields can be determined more accurately, and emission is more predictable. A simple concentric sphere model closely approximates the field for a *tip-to-hemispherical anode* geometry (Figure 1.4 ) as  $F=VRr/((R-r)x^2)$ , where V is the applied voltage, x is the distance from the center of the spheres, and R and r are the radii of the large and small spheres, respectively.

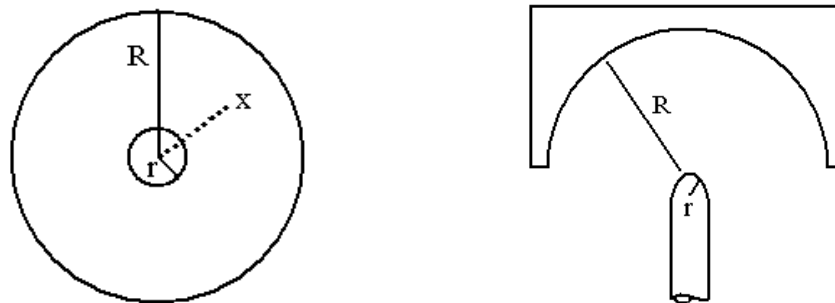


**Figure 1.4** Schematic of concentric sphere geometry for approximating field enhancement and a corresponding *real* tip-to-hemisphere geometry.

When  $R \gg r$ , which is usually the case for a needle-shaped emitter (e.g. radius  $< 100\text{nm}$ ) used in conjunction with a hemispherical anode (e.g. radius  $\sim 1\text{cm}$ ), the field at the tip apex approaches

$$F = \beta V \quad (1.9)$$

where  $\beta = 1/kr$ , with  $r$  being the radius of curvature of the emitter and  $k \sim 5$  is an empirical constant whose value depends on the exact geometry of the system (the fact that  $k > 1$  is a consequence of the geometry not being ideal concentric-spheres).

Making use of equation (1.9), the expression for current density (equation (1.8)) can be multiplied by the emission area ( $\alpha$ ) to give an expression for current as a function of applied voltage ( $V$ ):

$$\begin{aligned} I &= aV^2 \exp\left(-\frac{b}{V}\right); \\ a &\equiv \alpha \frac{A\beta^2}{1.1\phi} \exp\left(\frac{9.84}{\phi^{1/2}}\right) \\ b &\equiv \frac{.95B\phi^{3/2}}{\beta} \\ A &= 1.54 \cdot 10^{-6}, A eV V^{-2} \\ B &= 6.831 \cdot 10^7, eV^{-3/2} V cm^{-1} \end{aligned} \quad (1.10)$$

where  $\alpha$  is the emission area in  $\text{cm}^2$ ,  $\beta$  is the field enhancement factor in  $\text{cm}^{-1}$ , and  $\phi$  is the work function in eV. Equation (1.10) is the form of the Fowler-Nordheim equation

commonly used in experiment. It can be seen that plotting current and voltage field emission data in what is termed *Fowler-Nordheim coordinates*, namely  $\ln(I/V^2)$  versus  $1/V$ , yields a straight line, with slope  $(-)\mathbf{b}$  and an intercept of  $\ln(\mathbf{a})$ . Further, the experimentally determined values of  $\mathbf{a}$  and  $\mathbf{b}$  can be multiplied together to yield

$$ab^2 = \alpha \frac{.95AB^2\phi^2}{1.1} \exp\left(\frac{9.84}{\phi^{1/2}}\right) \equiv \alpha(6.206 \cdot 10^9)\mathbf{g}(\phi) \quad (1.11)$$

Clearly, if the work function is known, then emission area can be determined from equation (1.11). However, even if the exact value of the work function is unknown (e.g. variations in work function due to different surface orientations), the emission area can be determined to within an error of 10% or less; it is only necessary that a material have a work function within the range of 3.5-11.5 eV. This can be illustrated by plotting  $\mathbf{g}(\phi)$  from equation (1.11) (Figure 1.5). With the proper choice of  $\mathbf{g}$  (i.e.  $\mathbf{g}=2200$ ), emission area is determined with 10%, or less, error if the work function is within the specified limits [48].

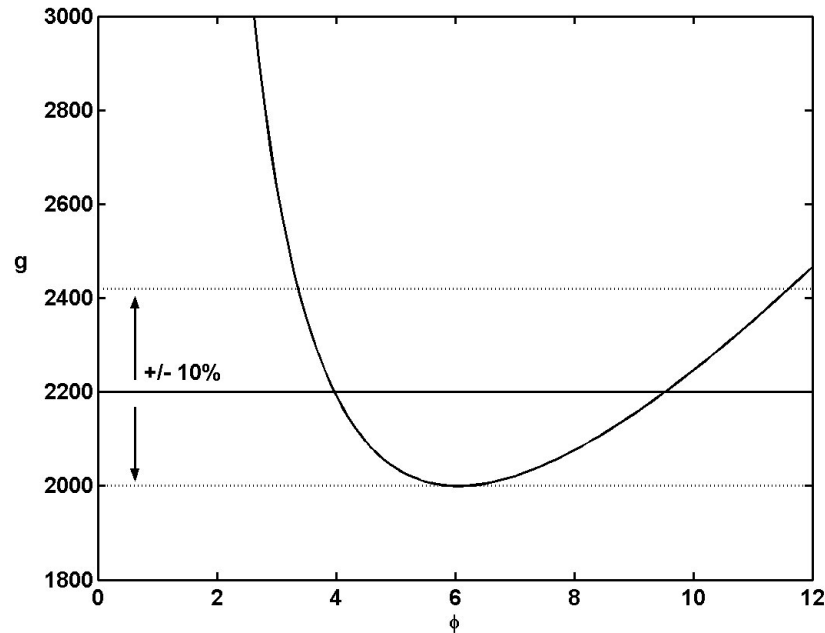


**Figure 1.5** Plot of  $g(\phi)$  illustrating maximum error of 10% in the range of 3.5-11.5 eV.

#### 1.4.4 Field Emitter Fabrication

Field emitters were initially made most often of refractory metals, like molybdenum and tungsten [48-51], primarily due to their high melting point and mechanical toughness. However, microfabrication techniques of the electronics industry were eventually applied extensively to produce field emitter structures [52-57]. In a continuing effort to improve field emitter performance, the use of *thin films* or *coatings* on the surfaces of field emitters has been studied in great detail [38,39,58-63]. Effects on emission characteristics such as threshold voltage, stability, and electron energy

distribution [61,64] as well as the changes in these properties as a function of thickness have been investigated [59].

## **1.5 FIELD EMISSION FROM DIAMOND**

There has been much interest in the use of diamond in field emission applications [33, 34, 37-39, 58, 59, 65-70]. The high thermal conductivity of diamond combined with its insulating properties and low (even negative) electron affinity make it an attractive candidate for field emission devices. To maximize the effectiveness of diamond coatings, and better understand the mechanisms responsible for emission through diamond, a number of thickness effect studies have been performed [33,59,65]. Zhirnov et al have shown field emission behavior of diamond powder coated silicon and molybdenum field emitters to be dependent on the thickness of the diamond coating [59]. Field emission measurements through diamond of varying thickness, ranging from ~100nm - 200nm up to 0.5 $\mu$ m - 1 $\mu$ m, were taken. It was observed that emission current was suppressed with increasing diamond thickness. The current suppression was attributed to negative charging in the diamond layer; the amount of charge within the diamond during emission is proportional to the diamond thickness. The thicker diamond contains more uncompensated charge and thus results in stronger current suppression. A similar study was later performed using two types of diamond coatings: hot filament chemical vapor deposited (HFCVD) and microwave plasma-enhanced chemical vapor deposited (MPCVD) [33]. The HFCVD diamond was observed to suppress emission with increasing thickness (from 0.2 $\mu$ m - 2 $\mu$ m), similar to diamond powder coatings, although the thickness

effect for HFCVD diamond was attributed to the dependence of emission on the electric field at the diamond-vacuum interface. The MPCVD diamond coatings, however, demonstrated little or no thickness effect, with emission current threshold being nearly constant for a range of coating thickness (0.1 $\mu\text{m}$  to 2.4 $\mu\text{m}$ ). The proposed mechanism suggested emission occurred at the diamond grain boundary – vacuum interface, thus thickness of the coating was not a significant factor. It should be noted, however, that various types of diamond prepared by different means could have significantly different structures, making direct comparisons quite difficult. Other thickness effect studies have observed maximum current (that required the destruction of the field emitter) to increase as a function of thickness, with coatings ranging from 0.5 $\mu\text{m}$  to 2 $\mu\text{m}$  [65].

While the above studies, as well as others, have offered insight into the mechanisms responsible for emission through diamond, and have demonstrated the effectiveness of diamond in enhancing emission current, they are limited to relatively *large* amounts of diamond, with coating thickness on the order of hundreds of nanometers to microns. Emission enhancement with decreasing thickness has only been demonstrated down to  $\sim 100\text{nm}$ . The question remains: *what is the ultimate lower limit of diamond thickness that will yield an improvement in emission characteristics?* By addressing this question, not only may maximum emission enhancement be achieved, but also more basic questions can be more suitably addressed when dealing with a system that is inherently less complex; namely a single crystal of diamond on the tip of a field emitter as opposed to a *thick* coating that contains many crystallites and grain boundaries and a more complex morphology.

## **1.6 SUMMARY**

As materials of ever-decreasing size are being utilized in science and industry, it becomes increasingly important to understand the properties of materials at such small scales. A material's size can affect both electronic and physical properties, and ultimately determine the applications where the material may prove useful. This research will focus on the study of nanometer-scale diamond particles and the effect of a particle's size on its properties. The origins of this work are in field emission, and the use of diamond for improving field emission characteristics. However, although field emission comprises a large part of this research, it is more appropriately viewed as a tool with which to study nano-scale materials, along with the other complementary techniques (e.g. SEM, TEM, EELS) used in this research.

## 1.7 REFERENCES

- 1 J. Liu and J. Hren, *SEM and Field Emission Study of Silicon Field Emitter Array*, Proceedings of the Electron Microscopy Society of America, Boston, 1140 (1992).
- 2 U. T. Son, J. Liu, A. N. Stepanova, G. J. Wojak, J. J. Hren, K. J. Bachmann, E. I. Givargizov, *Formation of SiC on the Atomically Sharp Si Tips: A Combined Study by FIM, FEM, and TEMI*, International Field Emission Symposium, Halifax, N.S., August (1992).
- 3 J. Liu, J. J. Hren, C. T. Sune, G. W. Jones, and H. F. Gray, *Field Emission Imaging Study of Silicon Field Emitters*, International Conference on Vacuum Microelectronics, Vienna, July (1992).
- 4 J. Liu, J. J. Hren, U. T. Son, G. W. Jones, and C. T. Sune, *Field Emission from Silicon through Stable Contaminant Layers*, Applied Surface Science **67** (1-4) 48 (1993).
- 5 J. Liu, V. Zhirnov, G. Wojak, A. Myers, W. Choi, J. Hren, S. Wolter, M. McClure, B. Stoner, and J. Glass, *Electron Emission from Diamond Coated Silicon Field Emitters*, Applied Physics Letters **65** (22) 2842 (1994).
- 6 J. Liu, A. F. Myers, S. M. Camphausen, M. T. McClure, J. J. Cuomo, and J. J. Hren, *Crystalline and Amorphous Diamond Coatings on Silicon Field Emitters*, Applications of Diamond Films and Related Materials: Third International Conference, 57 (1995).

- 7 A. F. Myers, J. Liu, W. B. Choi, G. J. Wojak, and J. J. Hren, *High Resolution TEM Study of Diamond Formation on Silicon and Molybdenum Emitter Surfaces*, Proceedings of the Materials Research Society, **354** 449 (1995).
- 8 W. Choi, J. Cuomo, V. Zhirnov, A. Myers, and J. Hren, *Field Emission from Silicon and Molybdenum Tips Coated with Diamond Powder by Dielectrophoresis*, Applied Physics Letters, **68** 720 (1996).
- 9 V. V. Zhirnov, W. B. Choi, J. J. Cuomo, J. J. Hren, *Diamond Coated Silicon and Molybdenum Field Emitters: Thickness Effect*, Applied Surface Science **94/95** 123-128 (1996).
- 10 A. F. Myers, S. M. Camphausen, J. J. Cuomo, and J. J. Hren, *Characterization of Amorphous Carbon Coated Silicon Field Emitters*, Journal of Vacuum Science and Technology B **14** (3) 2024 (1996).
- 11 W. B. Choi, J. Liu, M. T. McClure, A. F. Myers, V. V. Zhirnov, J. J. Cuomo, and J. J. Hren, *Field Emission from Diamond Coated Molybdenum Field Emitters*, Journal of Vacuum Science and Technology B **14** (3) 2050 (1996).
- 12 J. Liu, V. V. Zhirnov, W. B. Choi, G. J. Wojak, A. F. Myers, J. J. Cuomo, and J. J. Hren, *Electron Emission from a Hydrogenated Diamond Surface*, Applied Physics Letters **69** (26) 23 December (1996).
- 13 R. Schlessler, M. T. McClure, W. B. Choi, J. J. Hren, and Z. Sitar, *Energy Distribution of Field Emitted Electrons from Diamond Coated Molybdenum Tips*, Applied Physics Letters **70** (12) 24 March (1997).

- 14 L. E. Brus, *A Simple Model for the Ionization Potential, Electron Affinity, and Aqueous Redox Potentials of Small Semiconductor Crystallites*. *Journal of Chemical Physics* **79** (11) 5566 (1983).
- 15 L. E. Brus, *Electron-Electron and Electron-Hole Interactions in Small Semiconductor Crystallites: The Size Dependence of the Lowest Excited Electronic State*. *Journal of Chemical Physics* **80** (9) 4403 (1984).
- 16 R. T. Collins, P.M. Fauchet, and M.A. Tischler, *Porous Silicon: From Luminescence to LEDs*. *Physics Today*, **50** 24 (1997).
- 17 L. T. Canham, *Silicon Quantum Wire Array Fabrication by Electrochemical Dissolution of Wafers*. *Applied Physics Letters*, **57** 1046 (1990).
- 18 S. Vepřek, *Electronic and Mechanical Properties of Nanocrystalline Composites when Approaching Molecular Size*. *Thin Solid Films* **297** 145-153 (1997).
- 19 T. Trindade, *Nanocrystalline Semiconductors: Synthesis, Properties, and Perspectives*. *Chemistry of Materials* **13** 3843 (2001).
- 20 F. W. Wise, *Lead Salt Quantum Dots: The Limit of Strong Quantum Confinement*. *Accounts of Chemical Research* **33** (11) 773 (2000).
- 21 Y. A. Suna Wang, W. Mahler, and R. Kasowski, *PbS in Polymers. From Molecules to Bulk Solids*. *Journal of Chemical Physics* **87** (12) 7315 (1987).
- 22 C. Q. Sun, T. P. Chen, B. K. Tay, S. Li, H. Huang, Y. B. Zhang, L. K. Pan, S. P. Lau, and X. W. Sun, *An Extended 'Quantum Confinement' Theory: Surface-coordination Imperfection Modifies the Entire Band Structure of a Nanosolid*. *Journal of Physics D: Applied Physics* **34** 3470 (2001).

- 23 R. Tsu, D. Babić, L. Ioriatti Jr., *Simple Model for the Dielectric Constant of Nanoscale Silicon Particle*. Journal of Applied Physics **82** (3) 1327 (1997).
- 24 L. W. Wang and A. Zunger, *Pseudopotential Calculations of Nanoscale CdSe Quantum Dots*. Physical Review B **53** 9579 (1996).
- 25 L. W. Wang and A. Zunger, *Dielectric Constants of Silicon Quantum Dots*. Physical Review Letters **73** 1039 (1994).
- 26 M. Lannoo, C. Delerue, and G. Allan, *Screening in Semiconductor Nanocrystallites and Its Consequences for Porous Silicon*. Physical Review Letters **74** 3415 (1995).
- 27 R. Berman, *Physical Properties of Diamond*. Oxford University Press (1965).
- 28 J. E. Field, *Properties of Diamond*. Academic Press, New York, (1979).
- 29 M. Ohring, *The Materials Science of Thin Films*, Academic Press, Inc., San Diego (1992).
- 30 R. C. Weast, *CRC Handbook of Chemistry and Physics*, CRC Press, Boca Raton, FL, (1978)
- 31 H. Liu and D.S. Dandy, *Diamond Chemical Vapor Deposition – Nucleation and Early Growth Stages*, Noyes Publications, New Jersey (1995).
- 32 E. Kohn, W. Ebert, A. Aleksov, A. Denisenko, M. Adamschik, P. Schmid, *Diamond Technology for Electronics and MEMS: Review of Status and Perspectives*. Proceedings of 23<sup>rd</sup> International Conference on Microelectronics (MIEL 2002) Vol.1, Niš, Yugoslavia (2002).
- 33 A. R. Krauss, et al, *Electron Field Emission for Ultrananocrystalline Diamond Films*. Journal of Applied Physics **89** (5) 2958 (2001).

- 34 W. P. Kang, J. L. Davidson, A. Wisitsora-at, D.V. Kerns, and S. Kerns, *Recent Development of Diamond Microtip Field Emitter Cathodes and Devices*. Journal of Vacuum Science and Technology B **19** (3) 936 (2001).
- 35 M. Sakamoto, J. G. Endriz, and D. R. Scifres, *120W CW Output Power from Monolithic AlGaAs (800nm) Laser Diode Array Mounted on Diamond Heatsink*. Electron. Lett. **28** (2) 197 (1992).
- 36 S. Weiss, E. Zakel, and H. Reichl, *Mounting of High Power Laser Diodes on Diamond Heatsinks*. IEEE Transactions on Components, Packaging, and Manufacturing Technology – Part A **19** (1) 46 (1996).
- 37 J. H. Jung, B. K. Ju, Y. H. Lee, J. Jang, and M. H. Oh, *Enhancement of Electron Emission Efficiency and Stability of Molybdenum-Tip Field Emitter Array by Diamond Like Carbon Coating*. IEEE Electron Device Letters **18**(5) 197 (1997).
- 38 V. V. Zhirnov, *Emission Mechanism and Optimum Parameters of Diamond Cold Cathode*. Technical Digest of IVMC '97. 10<sup>th</sup> International Vacuum Microelectronics Conference, Kyonghu, Korea: Electronic Display Industrial Research Association of Korea. 485-488 (1997).
- 39 V. V. Zhirnov, E. I. Givargizov, and P. S. Plekhanov, *Field Emission from Silicon Spikes with Diamond Coatings*. Journal of Vacuum Science and Technology B, **13** (2) 418-421 (1995).
- 40 E. Kohn, W. Ebert, M. Adamschik, P. Schmid, A. Denisenko, *Diamond Based MEMS Devices*. IEEE Journal of New Diamond & Frontier Carbon Technology, **11** 81-100 (2001).

- 41 R. Gomer, *Field Emission and Field Ionization*. 1961, New York: Originally published by Harvard Univ. Press, Cambridge. Reprinted by American Institute of Physics, 1993.
- 42 S. M. Sze, *Physics of Semiconductor Devices*, John Wiley & Sons, New York (1981).
- 43 A. Modinos, *Field, Thermionic, and Secondary Electron Emission Spectroscopy*. 1984, New York: Plenum Press.
- 44 R. H. Fowler and L.W. Nordheim, Proc. R. Soc. London A **119** 173 (1928).
- 45 A. Modinos, Surface Science **70** 52 (1978).
- 46 J. W. Gadzuk and E.W. Plummer, Reviews of Modern Physics **45** 487 (1973).
- 47 T. Utsumi, *Keynote Address: Vacuum Microelectronics: What's New and Exciting*. IEEE Transactions on Electron Devices **38** (10) 2276-2283 (1991).
- 48 I. Brodie and C. A. Spindt, *Vacuum Microelectronics*. Advances in Electronics and Electron Physics. Vol. 83. 1992: Academic Press. 1-106.
- 49 A. Kaneko, T. Kanno, K. Tomii, M. Kitagawa, and T. Hirao, IEEE Transaction of Electron Devices **38** (10) 2395 (1991).
- 50 C. A. Spindt, I. Brodie, L. Humphrey, and E. R. Westerberg, *Physical Properties of Thin-Film Field Emission Cathodes with Molybdenum Cones*. Journal of Applied Physics **47**(12) 5248 (1976).
- 51 D. Stewart and P. Wilson, Vacuum **30** 527 (1980).
- 52 P. A. Chen, W. X. Chen, and Z. P. Huang. *The Characteristics of Silicon Field Emission Triode in 9<sup>th</sup> International Vacuum Microelectronic Conference* (1996).

- 53 V. V. Zhirnov, *Emission Mechanism and Optimum Parameters of Diamond Cold Cathode*. Technical Digest of IVMC '97. 10<sup>th</sup> International Vacuum Microelectronics Conference, Kyonghu, Korea: Electronic Display Industrial Research Association of Korea. 485-488 (1997).
- 54 V. V. Zhirnov, E. I. Givargizov, N. N. Chubun, and A. N. Stepanova, *Field Emission Lamps Based on Diamond Coated Silicon Emitters*. Technical Digest of IVMC '97. 10<sup>th</sup> International Vacuum Microelectronics Conference, Kyonghu, Korea: Electronic Display Industrial Research Association of Korea 490 (1997).
- 55 S. E. Huq, M. Huang, P. R. Wilshaw, and P. D. Prewett. *Fabrication of Gated Polycrystalline Silicon Field Emitters* in 9<sup>th</sup> International Vacuum Microelectronics Conference, St. Petersburg: IEEE/EDS (1996).
- 56 J. H. Lee, S. W. Kang, S. G. Kim, Y. S. Song, K. I. Cho, and H. J. Yoo. *A New Fabrication Method of Silicon Field Emitter Array with Local Oxidation of Polysilicon and Chemical-Mechanical Polishing* in 9<sup>th</sup> International Vacuum Microelectronics Conference, St. Petersburg: IEEE/EDS (1996).
- 57 H. S. Uh, S. J. Kwon, J. D. Lee, and H. S. Park. *Fabrication and Characterization of Gated n+ Polycrystalline Silicon Field Emitter Arrays* in 9<sup>th</sup> International Vacuum Microelectronics Conference, St. Petersburg: IEEE/EDS (1996).
- 58 V. V. Zhirnov, A. B. Voronin, E. I. Givargizov, and A. L. Meshcheryakova, *Emission Stability and High Current Performance of Diamond-Coated Si Emitters*. Journal of Vacuum Science & Technology B **14** (3) 2034 (1996).

- 59 V. V. Zhirnov, W. B. Choi, J. J. Cuomo, and J. J. Hren, *Diamond Coated Si and Mo Field Emitters: Diamond Thickness Effect*. *Applied Surface Science* **94/95** 123 (1996).
- 60 J. O. Choi, J. W. Huh, Y. H. Choi, M. J. Kim, H. Kim, Y. R. Cho, and H. S. Jeong, *Field Emission Properties of Diamondlike Carbon Films Made by a Novel Laser Evaporation Technique*. *Journal of Vacuum Science & Technology B* **16** (3) 199 (1998).
- 61 W. B. Choi, R. Schlessler, G. Wojak, J.J. Cuomo, Z. Sitar, and J. J. Hren, *Electron Energy Distribution of Diamond-Coated Field Emitters*. *Journal of Vacuum Science & Technology B* **16** (2) 716 (1998).
- 62 W. B. Choi, J. Liu, M. T. McClure, A. F. Myers, V. V. Zhirnov, J. J. Cuomo, and J. J. Hren, *Field Emission from Diamond Coated Molybdenum Field Emitters*. *Journal of Vacuum Science & Technology B* **14** (3) 2050 (1996).
- 63 W. B. Choi, J. J. Cuomo, V. V. Zhirnov, A. F. Myers, and J. J. Hren, *Field Emission from Silicon and Molybdenum Tips Coated with Diamond Powder by Dielectrophoresis*. *Applied Physics Letters* **68** (5) 720 (1996).
- 64 M. Hajra, N. N. Chubun, A. G. Chakhovskoi, C. E. Hunt, K. Liu, A. Murali, S. H. Risbud, T. Tyler, and V. V. Zhirnov, *Field Emission Characterization of Silicon Tip Arrays Coated with GaN and Diamond Nanoparticle Clusters*. *Journal of Vacuum Science and Technology B* **21** (1) 458 (2003).
- 65 V. V. Zhirnov, C. Lizzul-Rinne, G. J. Wojak, R. C. Sanwald, J. J. Cuomo, and J. J. Hren, *Optimizing High-Current Yields from Diamond Coated Field Emitters*. *Journal of Vacuum Science and Technology B* **19**(1) 17 (2001).

- 66 C. Wang, A. Garcia, D. C. Ingram, M. Lake, and M. E. Kordesch, *Electron. Lett.* **27**, 1459 (1991).
- 67 N. S. Xu, Y. Tzeng, and R. V. Latham, *J. Phys. D* **26**, 1776 (1993).
- 68 M. W. Geis, J. C. Twichell, and T. M. Lyszczarz, *J. Vac. Sci. Technol. B* **14**, 2060 (1996).
- 69 V. V. Zhirnov and J. J. Hren, *MRS Bull.* 23, 42 (1998).
- 70 T. A. Railkar, W. P. Kang, H. Windischmann, A. P. Malshe, H. A. Naseem, J. L. Davidson, and W. D. Brown, *Crit. Rev. Solid State Mater. Sci.* **25**, 163 (2000).

## CHAPTER 2

### SAMPLE PREPARATION

#### 2.1 INTRODUCTION

In order to facilitate the manipulation and isolation of nanoscale objects, an appropriate substrate must be employed. Such a substrate must allow for individual particles (a few nanometers in diameter) to be *placed* in a position where they are: 1) readily observable (e.g. by electron microscopy) and 2) sufficiently isolated from their surroundings so that detailed compositional and structural analysis can be performed. Ultra-sharp needles, with curvature radii less than 100nm, are well suited for such a purpose.

#### 2.2 ETCHING

Ultra-sharp needles were formed by electrochemical etching of metal wire [1]. Both molybdenum and aluminum wires were used.

##### 2.2.1 Molybdenum

Molybdenum was chosen because its refractory properties are well suited for field emission [2, 3]. Lengths (~30mm) of 125 micron diameter molybdenum wire were cut and crimped inside ~15mm lengths of copper tubing for ease of handling. A concentrated solution of KOH was prepared in a 25mL beaker. Placed in the beaker was a platinum

electrode, which was connected to ground. A positive 10-15 volt bias was applied to a single wire, which was then dipped into the solution (Figure 2.1). Etching progresses rapidly, and the wire breaks within ~1 minute. Upon breaking, the wire was immediately removed from solution to prevent further etching (and blunting) of the tip; one or two quick dips in solution follows this step to remove material at the tip that may have been deformed due to the huge stresses present during the final moments of etching (because of the small cross-sectional area of the wire just prior to breaking). The process results in molybdenum tips with typical radii of curvature less than 100nm down to ~20nm. It should be noted that in addition to molybdenum, etching is used to form ultra-sharp tips from a number of other materials, including tungsten, aluminum, and silicon [4-12], all of which can provide substrates for nanoscale studies.

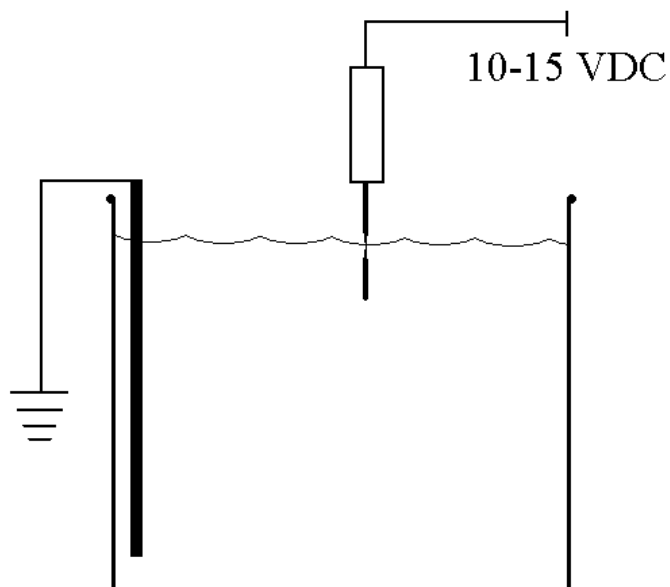


**Figure 2.1** Schematic of electrochemical etching of metal wire to form sharp needles.

While molybdenum tips of radii less than 100nm were successfully fabricated, it is worth noting that the nature of molybdenum, namely its numerous oxides that can readily form during etching, often resulted in a low *success rate*. The complex nature of electrochemical etching, and the numerous variables contributing to the etching rate (i.e. electric field, concentration, localized mixing, temperature, etc.) also made reproducibility difficult. The resulting etched samples varied drastically from one to the next, despite having been etched using seemingly identical conditions (Figure 2.2). The formation of thick layers of oxide frequently spoiled an etched tip, as can be seen in (Figure 2.3), which is an extreme case of oxide formation; specific etching conditions for this sample differed

in that the amount of etching solution was very small (a droplet suspended in a platinum loop); this technique often resulted in excessive amounts of oxide formation, but similar oxide formation (though to a lesser extent) occurred with the etching process illustrated in Figure 2.1. The molybdenum sample in this figure was examined in a scanning electron microscope, revealing unknown *contaminants*. Energy-dispersive spectrometry (EDS) was utilized to identify the unknown substances. As can be seen in the EDS spectrum (Figure 2.4), along with molybdenum peaks, there is a strong presence of oxygen (indicating the formation of molybdenum-oxide) as well as potassium (apparently KOH used for etching that failed to rinse from the crevices in the oxide). The difficulties associated with molybdenum sample preparation, namely the unpredictable formation of unwanted oxides, suggested that another material might better serve as a substrate for the nanoscale study of diamond.

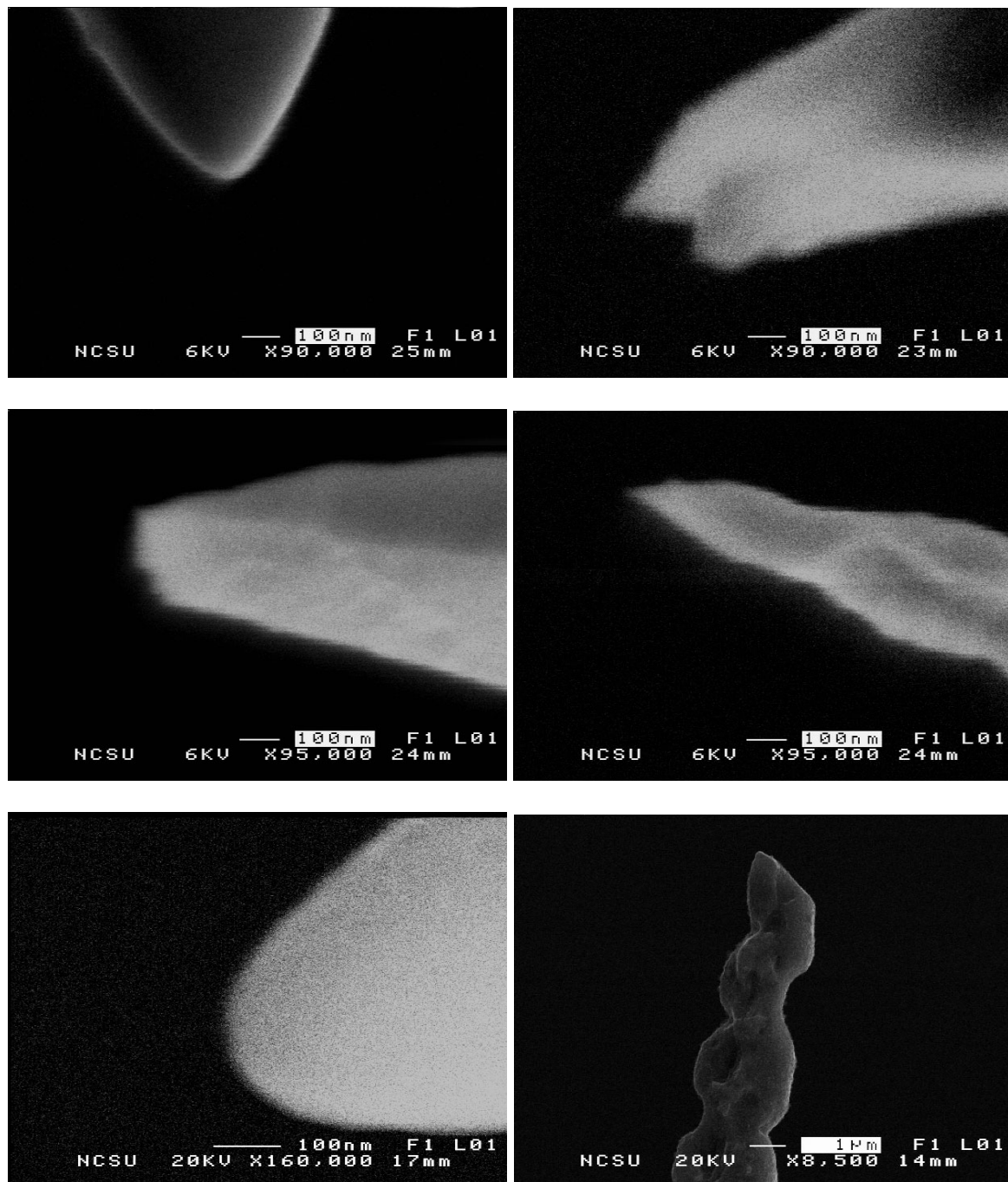


**Figure 2.2** Scanning electron micrographs of several molybdenum samples etched under identical conditions, but yielding varying results.



**Figure 2.3** Scanning electron micrograph of etched molybdenum wire illustrating the formation of oxide.

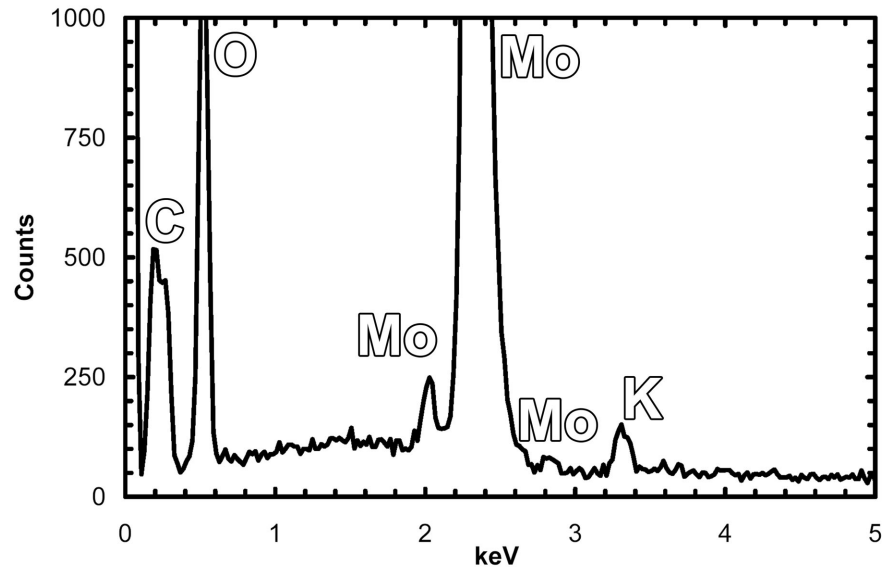


**Figure 2.4** X-ray energy-dispersive spectrum taken from sample in Figure 2.3. Oxygen peaks indicate oxide formation, while potassium is residue (from etching in KOH) trapped in the cracked oxide.

### 2.2.2 Aluminum

While molybdenum was chosen because of its refractory properties, and as such has been the material of choice, along with tungsten, for field emission experiments for decades, field emission optimization was not the focus of this work. Consequently, aluminum was included, despite having a much lower melting point ( $T_{\text{melt, Al}} = 660^{\circ}\text{C}$ ,  $T_{\text{melt, Mo}} = 2617^{\circ}\text{C}$ ; a high melting point is desirable for field emission in order to withstand the heating caused by high current densities) and being very soft (the aluminum, being much softer, is more difficult to handle from a practical standpoint).

The etching of aluminum samples was similar to that of molybdenum. The differences being the etching solution used for aluminum was a 20% perchloric / 80%

methanol mix, cooled to  $-30^{\circ}\text{C}$  in a dry-ice bath. The voltage applied was 15-20VAC (not DC, as for molybdenum), while the *dipping* method used for aluminum was the same as for molybdenum.

Although field emission optimization was not the focus of this work, the aluminum would have to provide reasonable amounts of current in order to utilize field emission as a *tool* for studying the nanodiamond. As such, an aluminum needle was tested for field emission and failure current (Figure 2.5). The aluminum was able to reliably produce more than one microamp of current (failure occurred at  $\sim 5$  microamps, not shown in figure). This result prompted the use of aluminum for field emission studies.

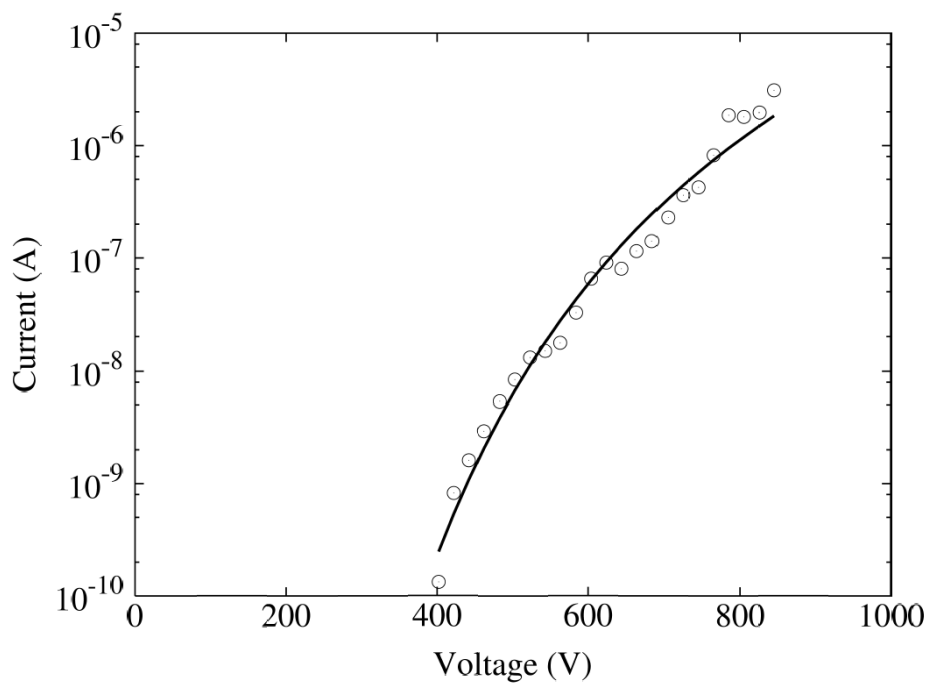


**Figure 2.5** Current-voltage measurements for an aluminum field emitter.

Maximum current exceeded one microamp (failure occurred at  $\sim 5$  microamps).

### 2.3 DIAMOND DEPOSITION

The diamond used in this work was produced by explosive detonation, which yields nanometer sized (1-10nm) diamond crystallites known as shock-synthesized *nanodiamond*. The process of shock-synthesizing nanodiamond involves detonating an explosive mixture, a process whose high temperature and pressure yields a number of byproducts, including diamond; a general reaction can be written as:



A common compound used for diamond shock-synthesis is TNT ( $C_6H_2CH_3(NO_2)_3$ ), which is detonated in a non-oxidizing medium (e.g. Ar,  $N_2$ , etc.). Various types of nanodiamond are distinguished by the post-treatment of the detonation soot, and are summarized in Table 2.1. Nanodiamond is the smallest known form of diamond matter, of which many properties are still unknown.

Diamond particles were deposited onto the tips via pulsed electrophoresis, using a suspension of diamond in ethanol [13]. The suspension was prepared by measuring 2 grams of NdO type (see Table 2.1) diamond powder (which was formed by explosive detonation yielding crystallites from 1-10nm [14]) for every 1 liter of ethyl alcohol; the diamond was combined with the ethanol and placed in an ultrasonic bath (Bransonic B2200R-1, 100W at 52kHz) for 15 minutes to facilitate the dispersion of the nanodiamond. Electrophoretic deposition of the diamond was accomplished by filling a small container with the suspension and applying a pulsed bias to a tip submersed in the suspension (see Figure 2.6). The tip was separated from an electrode, on the bottom of the container, by a

distance of 10mm. The variables that were adjusted to yield the desired amount of diamond deposits were voltage (V), pulse width ( $\tau$ ), and the number of pulses (n); typical values used in this work were  $V = 1-10$  volts,  $\tau = 1$  millisecond, and  $n = 10-10^3$ . Positive bias was applied to the tip because it has been shown that diamond particles within aqueous- and organic- dispersions are charged negatively [15,16], and will thus move toward the anode. It was determined that pulse widths of 1ms, with the number of pulses on the order of one thousand yielded more uniform diamond coverage (Figure 2.7). It is believed that the high number of pulses facilitates the breaking up of diamond agglomerates that form in suspension and otherwise deposit on the needle. Several transmission electron micrographs are also shown as examples of deposited diamond nanoparticles in Figure 2.8. The electrophoretic deposition technique was also extended to arrays (Figure 2.9), where an array of silicon emitters was coated to demonstrate the scalability of this technique; although not studied in this work, the diamond-coated arrays were used in another field emission study (see reference 17), which demonstrated an increase in emission (a decrease in threshold voltage) upon the deposition of nanodiamond (Figure 2.9). These results suggest that the technique of electrophoretic deposition of nanodiamond may be a viable means to improve field emission in scalable (commercial) devices.

**Table 2.1** Summary of various types of detonation-produced nanodiamond (reproduced from [14]).

ND Type:	Nd	NdP	NdP <sub>1</sub>	NdP <sub>2</sub>	NdO
Crystallite size	1-10 nm	1-10 nm	1-10 nm	1-10 nm	1-10 nm
O, N, H(%)	12-14	2	2	1	2
pH (10% water suspension)	5.6-6.2	4.5-5.5	3.5-4.5	5.6-6.2	1.6-2.0
Density (g/cm <sup>3</sup> )	3.1-3.15	3.2	3.2-3.3	3.1	3.3-3.4
Modification	Standard	High-temperature treatment	High-temperature treatment-top fraction	High-temperature treatment-bottom fraction	Ozone treatment

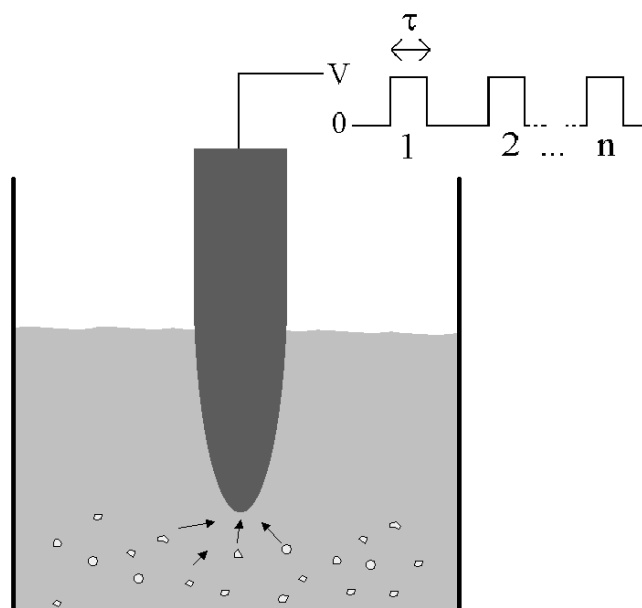


**Figure 2.6** Schematic of electrophoretic deposition of diamond nanoparticles via pulsed bias.

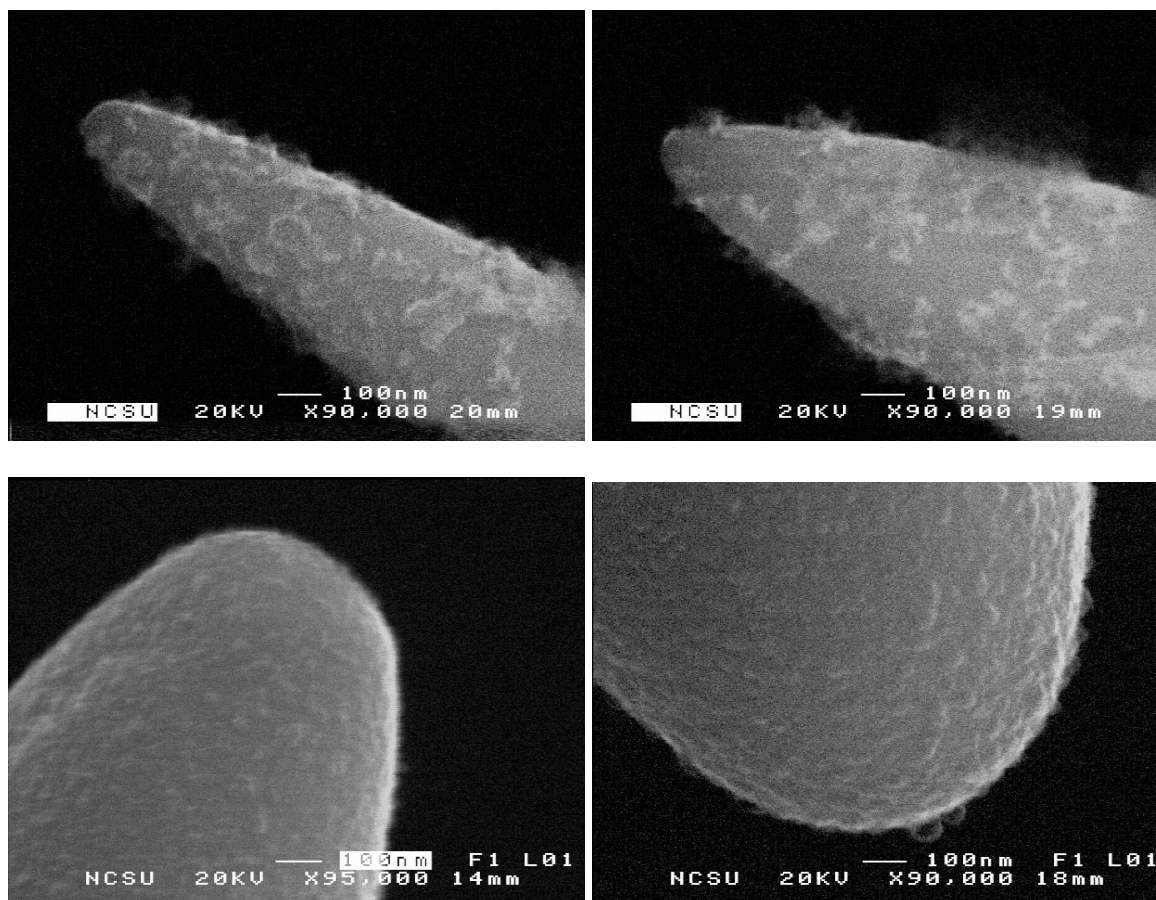
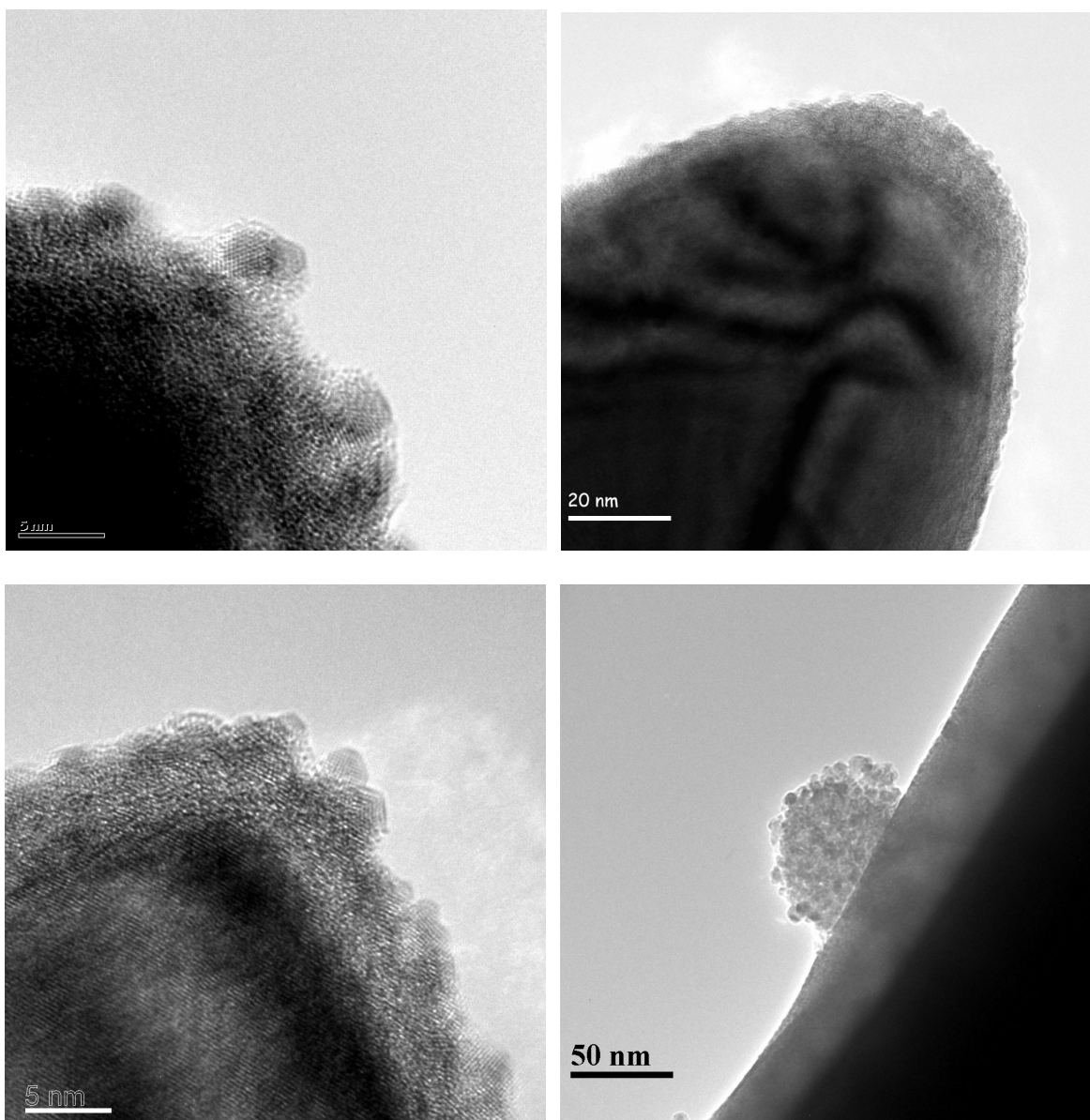
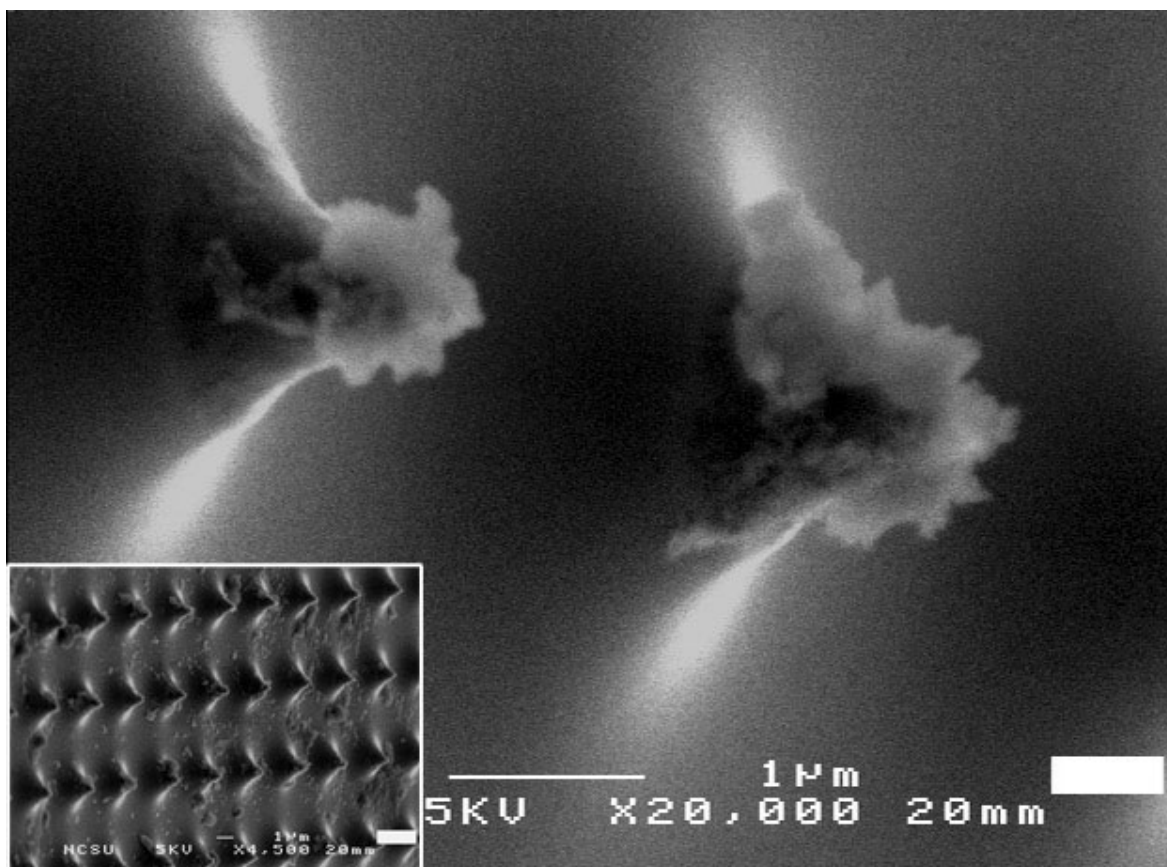


Figure 2.7 Scanning electron micrographs of four molybdenum needles with varying amounts of nanodiamond deposits. The four samples were coated using identical parameters except for number of pulses; the top 2 samples underwent 10 pulses (1ms at +5V), while the bottom 2 samples underwent ~1000 pulses (1ms at +5V).



**Figure 2.8** Transmission electron micrographs of several different molybdenum samples illustrating the deposition of nanodiamond particles on the surface, both isolated particles and agglomerates are seen.



**Figure 2.9** Scanning electron micrograph of diamond-coated array of silicon tips (inset shows array at lower magnification).

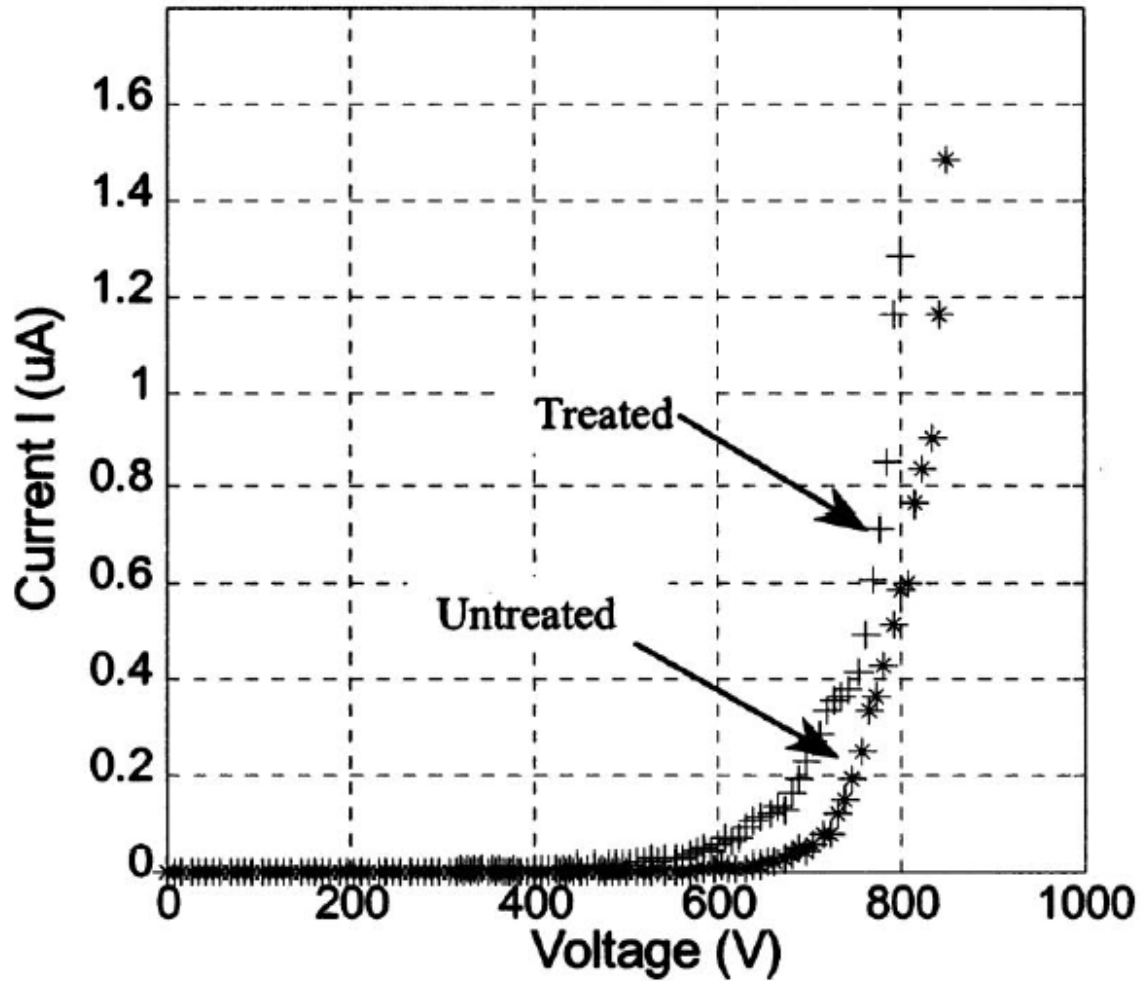


**Figure 2.10** Current-voltage data taken from an un-coated silicon array (*untreated*) and the same array coated with nanodiamond (*treated*).

## 2.4 DIAMOND POWDER CHARACTERIZATION

The NdO type ultra-dispersed nanodiamond powder used in this work was characterized in a transmission electron microscope to determine the composition and morphology of the powder prior to electrophoretic deposition. A diamond powder suspension was prepared as described above; a drop of the suspension was then placed on a *holey-carbon* TEM grid and allowed to dry (sample was heated to 100°C for 1 minute to facilitate drying and removal of possible contaminants), leaving clusters of diamond powder on the grid. A standard TEM sample-prep plasma cleaning (argon/oxygen) was then performed on the grid and sample holder. TEM was then performed (Figure 2.11) as well as electron energy loss spectrometry (Figure 2.12). The portion of diamond powder from which the micrograph and EELS spectrum were taken was overhanging a void in the carbon support film, so there was no contribution to the spectrum from the support film.

The imaged diamond powder (Figure 2.11) revealed clusters of diamond crystallites agglomerated together. While the image is slightly blurred (due to the clusters, overhanging a void in the support film, moving under the influence of the electron beam), the periodic lattice structure of individual crystallites is evident. Furthermore, the EELS spectrum taken from the powder (Figure 2.12) indicates a diamond structure; the series of peaks from ~290 eV to ~340 eV are characteristic of diamond. In addition to diamond bonds ( $sp^3$ ), the shoulder at ~287 eV indicates the presence of non-diamond bonding (i.e.  $sp^2$ ). The  $sp^2$  bonding fraction was estimated to be between 0.15 and 0.25 by measuring the ratio of the  $1s-\pi^*$  peak (~287eV) to that of a published standard [18] (normalized to the  $1s-\sigma^*$  peak at ~294eV); more accurate bonding fraction calculations require a standard to

be used in-situ, highly oriented pyrolytic graphite (HOPG) or preferably a C<sub>60</sub> fullerite [18]. However, the sp<sup>2</sup> bonding fraction was not a critical parameter to be determined, so published data from HOPG and C<sub>60</sub> were used to calculate an approximate sp<sup>2</sup> bonding fraction. The non-diamond carbon was determined to be surrounding the diamond particles (i.e. diamond particles contained in an amorphous carbon medium) and not within the crystallites themselves (see Results section in Chapter 4).

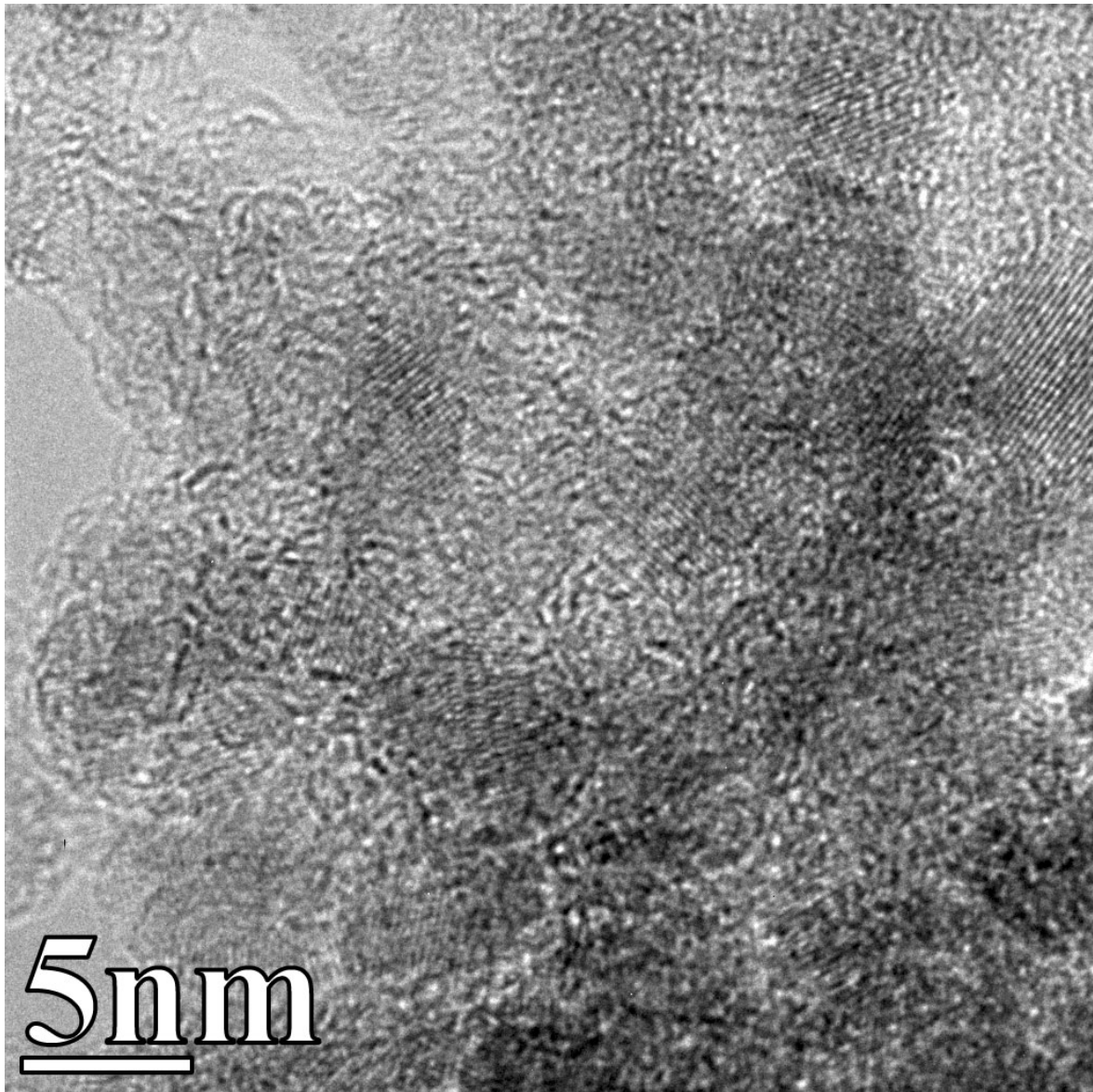


**Figure 2.11** Transmission electron micrograph of nanodiamond powder.

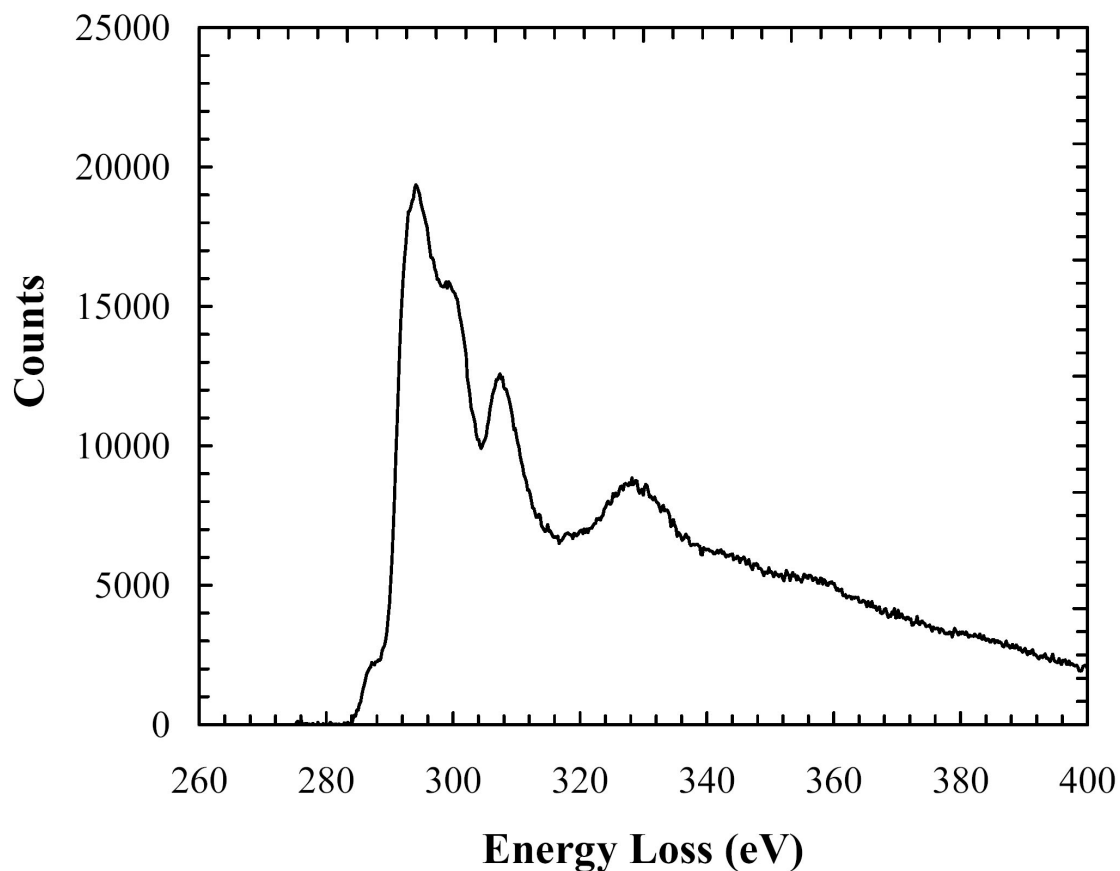


**Figure 2.12** Electron energy loss spectrum taken from nanodiamond powder imaged in Figure 2.11. Shoulder at  $\sim 287$  eV indicates presence of  $sp^2$  bonding, while peaks from  $\sim 290$  eV to  $\sim 340$  eV are characteristic of diamond bonding ( $sp^3$ ).

## 2.5 SUMMARY

Ultra-sharp needles, electrochemically etched to produce radii of curvature less than 100nm, were chosen as the substrate for nanodiamond isolation and characterization. The nature of sharp needles allows for electron microscopy studies (SEM, TEM, FEM) to be performed with no further sample preparation. Such techniques are also non-

destructive, making a series of experiments possible. The high fields ( $>\sim 10^7$  V/cm) and large field gradients ( $>\sim 10^{12}$  V/cm/cm) produced at the tip apex under applied bias allow small amounts of nanodiamond to be deposited over an area from which field emission measurements can be taken and which is readily observable using electron microscopy. The diamond powder to be deposited was characterized prior to deposition, and its composition determined, using transmission electron microscopy and electron energy loss spectrometry.

## 2.6 REFERENCES

- 1 E. W. Müller, and T. T. Tsong, *Field Ion Microscopy: Principles and Applications*, American Elsevier Publishing (New York, 1969).
- 2 I. Brodie and C. A. Spindt, *Vacuum Microelectronics*. Advances in Electronics and Electron Physics. Vol. 83. 1992: Academic Press. 1-106.
- 3 C. A. Spindt, I. Brodie, L. Humphrey, and E. R. Westerberg, *Physical Properties of Thin-Film Field Emission Cathodes with Molybdenum Cones*. Journal of Applied Physics **47**(12) 5248 (1976).
- 4 B. Halpern and R. Gomer, *Field Emission through Hydrogen and Helium Layers*. Journal of Chemical Physics **51**, 3043 (1969).
- 5 T. Engel and R. Gomer, *Adsorption of Oxygen on Tungsten: Field Emission from Single Planes*. Journal of Chemical Physics **52**, 1832 (1970).
- 6 L. Dong, J. Jiao, D. W. Tuggle, J. M. Petty, S. A. Elliff, and M. Coulter, *ZnO nanowires formed on tungsten substrates and their electron field emission properties*. Applied Physics Letters **82**, 1096 (2003).
- 7 J. C. She, N. S. Xu, S. Z. Deng, Jun Chen, H. Bishop, S. E. Huq, L. Wang, D. Y. Zhong, and E. G. Wang, *Vacuum Breakdown of Carbon-Nanotube Field Emitters on a Silicon Tip*. Applied Physics Letters **83**, 2671 (2003).
- 8 D. Elswick, J. Hren, P. Kotula, D. Wall, and N. Missert, *Localized Corrosion Initiation in Passive Thin Films*, 201st Meeting of The Electrochemical Society (ECS), Philadelphia, PA, May 12th, 2002.

- 9 V. V. Zhirnov, E. I. Givargizov, and P.S. Plekhanov, *Field Emission from Silicon Spikes with Diamond Coatings*. Journal of Vacuum Science and Technology B, **13** (2) 418-421 (1995).
- 10 V. V. Zhirnov, E. I. Givargizov, N. N. Chubun, and A. N. Stepanova, *Field Emission Lamps Based on Diamond Coated Silicon Emitters*. Technical Digest of IVMC '97. 10<sup>th</sup> International Vacuum Microelectronics Conference, Kyonghu, Korea: Electronic Display Industrial Research Association of Korea 490 (1997).
- 11 V. V. Zhirnov, A. B. Voronin, E. I. Givargizov, and A. L. Meshcheryakova, *Emission Stability and High Current Performance of Diamond-Coated Si Emitters*. Journal of Vacuum Science & Technology B **14** (3) 2034 (1996).
- 12 V. V. Zhirnov, W. B. Choi, J. J. Cuomo, and J. J. Hren, *Diamond Coated Si and Mo Field Emitters: Diamond Thickness Effect*. Applied Surface Science **94/95** 123 (1996).
- 13 W. Choi, J. Cuomo, V. Zhirnov, A. Myers, and J. Hren, *Field Emission from Silicon and Molybdenum Tips Coated with Diamond Powder by Dielectrophoresis*, Applied Physics Letters, **68** 720 (1996).
- 14 V. V. Zhirnov, O. M. Küttel, O. Gröning, A. N. Alimova, P. Y. Detkov, P. I. Belobrov, E. Maillard-Schaller, and L. Schlapbach, *Characterization of Field Emission Cathodes with Different Forms of Diamond Coatings*. Journal of Vacuum Science and Technology B **17**(2) 666 (1999).
- 15 H. L. Shergold and C. J. Hartley, *The Surface Chemistry of Diamond*. International Journal of Mineral Processing **9** 219-233 (1982).

- 16 L. M. Martynov and Yu. I. Nikitin, *Colloid-Chemical and Surface Properties of Synthetic Diamond Powders and Aqueous Dispersions of These Powders*. *Colloid Journal of the USSR* **52** 245-250 (1990).
- 17 M. Hajra, N. N. Chubun, A. G. Chakhovskoi, C. E. Hunt, K. Liu, A. Murali, S. H. Risbud, T. Tyler, and V. V. Zhirnov, *Field Emission Characterization of Silicon Tip Arrays Coated with GaN and Diamond Nanoparticle Clusters*. *Journal of Vacuum Science and Technology B* **21** (1) 458 (2003).
- 18 A. J. Papworth, C. J. Kiely, A. P. Burder, S. R. P. Silva, and G. A. J. Amaratunga, *Electron-energy-loss spectroscopy characterization of the sp<sup>2</sup> bonding fraction within carbon thin films*, *Physical Review B* **62** (19) 628-631 (2000).

## **CHAPTER 3**

### **CHARACTERIZATION TECHNIQUES**

#### **3.1 INTRODUCTION**

In order to better understand the properties of matter at the nanoscale, and to correlate changes in these properties with physical changes in the materials system of interest, a number of techniques must be employed. Morphological and compositional information at a resolution sufficiently high for the scale of the material being studied is necessary. Furthermore, any physical changes undergone by the sample that may affect its properties, either by design or consequence, must subsequently be observable so that these changes may account for the affected properties. Characterization techniques utilized in this work include field electron emission (FE), field emission microscopy (FEM), scanning electron microscopy (SEM), x-ray energy dispersive spectroscopy (EDS), transmission electron microscopy (TEM), and electron energy loss spectrometry (EELS).

In this work, current-voltage (I-V) measurements were made via field electron emission, where the electron emitter is either the sample being studied or serves as the substrate for the sample being studied (i.e. the sample of interest lies on the surface of the emitter). This configuration allows for the effectiveness of a material in improving field emission performance to be measured, e.g. by performing field emission prior- and subsequent to deposition of a material onto the emitter; furthermore, field emission can

provide information on the properties of the deposited material itself by observing the dependence of current on voltage compared to that of the substrate.

Field emission microscopy complements field emission I-V measurements, allowing for direct observation of emitted electrons from the emitter surface, but has limited resolution ( $\sim 2\text{nm}$ ) and is affected by surface adsorbates. Changes to the emitter that may affect field emission can be observed as changes in emission current (intensity of the FEM image) or emission area (size of FEM image).

Scanning electron microscopy was used to characterize etched wires (e.g. determine curvature radii) and diamond deposited samples. Energy dispersive spectroscopy was used in correlation with SEM to determine compositions of etched wires, including oxide formation and surface impurities.

Transmission electron microscopy is an essential part of this study of materials at the nanoscale, providing necessary information on sample morphology and crystallography at a sufficiently high resolution. In addition, the nature of samples used in this work, namely needle-shaped emitters, are *ideal* TEM samples, requiring no further preparation prior to examination in the microscope. Moreover, the emitters can undergo a number of various characterization steps (e.g. FE or FEM) and be examined in the TEM at any point in this process, and as such is one of the key advantages of this study.

Electron energy loss spectrometry is performed in conjunction with transmission electron microscopy, being an extension of the TEM. EELS provides compositional, and even chemical bonding, information on a sample with sub-nanometer resolution; ideally, EELS resolution is that of TEM, but practically a little less (mainly due to sample drift and signal to noise ratio for a specific sample). Such capabilities allow one to identify, or

confirm the absence of, a material, or a given phase of a material, within any sample suitable for TEM.

These techniques, which individually are powerful tools, become increasingly potent when used in conjunction with each other. Each technique being non-destructive allows for characterization by any of the methods to be performed in any order, an arbitrary number of times (3.1).

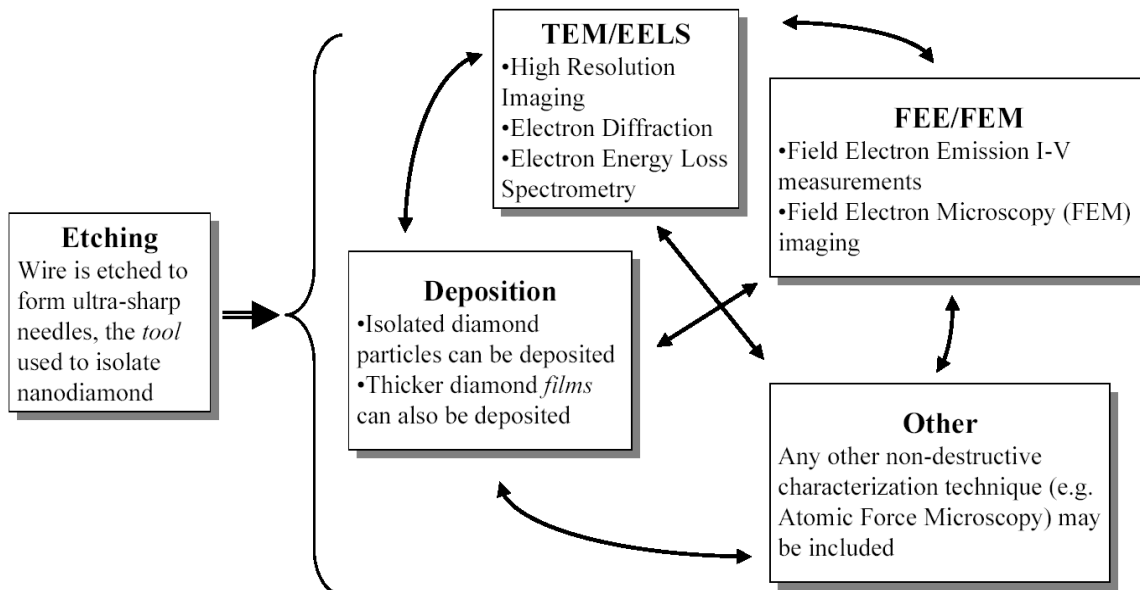


**Figure 3.1** Flowchart illustrating the arbitrary order in which the various characterization techniques can be performed.

### 3.2 FIELD EMISSION MEASUREMENTS

The field emission current-versus-voltage measurements in this study were carried out in the vacuum chamber illustrated in Figure 3.6. The chamber was maintained at a

vacuum between  $1 \cdot 10^{-9}$  and  $5 \cdot 10^{-9}$  torr for all experiments. Initial pumping was accomplished with a turbo pump backed by a mechanical pump. When the pressure reached the micro-torr range, the ion pump (Perkin-Elmer) was turned on to achieve and maintain a vacuum of  $\sim 10^{-9}$  torr. The *main chamber* pumped by the ion pump was isolated from the *load lock* chamber by closing the gate valve (see Figure 3.6), except for initial pumping and sample transfer. The pressure in the main chamber was monitored with an ion gauge (Huntington Mechanical Labs) and controlled with a Varian Multi-Gauge controller. Sample transfer to and from the main chamber and load lock was achieved with magnetically coupled sample transfer rods. Negative electrical bias was applied to the field emission samples by a high voltage power supply (Bertan Associates, model 205A-10R) interfaced with a personal computer via an IEEE-488 interface bus (Bertan Associates, model 200-C488). Current was determined by measuring the voltage drop across a known resistance ( $10 \text{ k}\Omega$  in series with  $100 \text{ k}\Omega$ ), connecting the faraday cup to ground, using a micro-volt meter (Keithley 197A); this configuration was used rather than placing an ammeter in series due to the likelihood of a damaged ammeter as a result of current spikes. When taking field emission measurements, however, any resistance placed in series could potentially affect field emission current; if the resistance is large, at high currents the resistance may limit emission rather than the emitter. It can be easily confirmed that a resistance of  $110 \text{ k}\Omega$  is insufficient to suppress emission in the range of the experiments contained within this work. For the *diode* (the field emission tip and anode) in series with a resistance (Figure 3.2), the effect the resistance has is to increase the voltage required to extract a given amount of current, due to the resistance drop across

the resistor. The greater the resistance, the greater the required *applied* voltage to extract the same amount of current:

$$V_0 = R(aV^2 \exp[-b/V]) + V \quad (3.1)$$

where the expression in parenthesis is the general form of the Fowler-Nordheim equation (i.e. the emitted current),  $V$  is the voltage from the tip to the anode, and  $V_0$  is the applied voltage. Several calculated current voltage curves are plotted in Figure 3.3 for resistances ranging from 0 ohms to 10 mega-ohms. The field emission current is not noticeably affected for resistance values less than 10 mega-ohms. Therefore, the use of the 110 k $\Omega$  resistance will not affect field emission measurements.

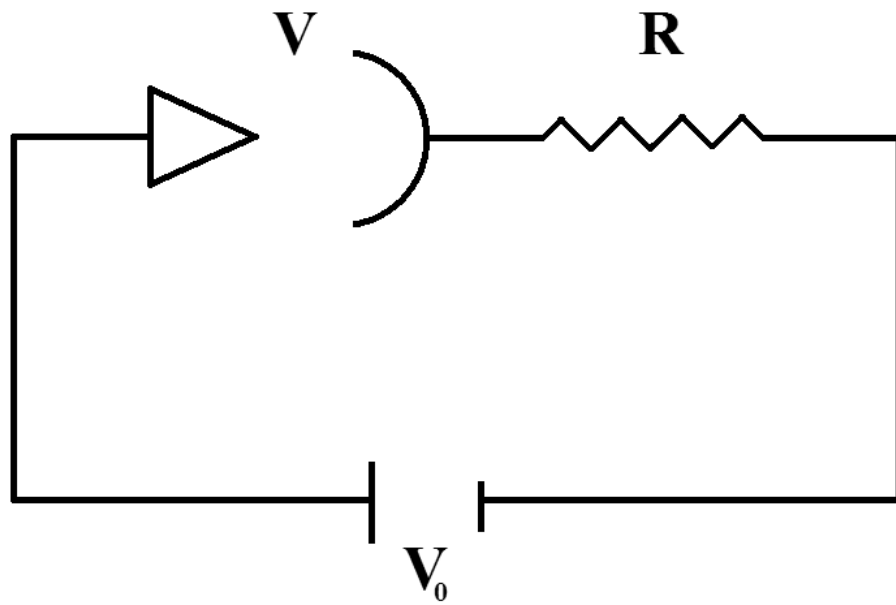


**Figure 3.2** Schematic of *diode* configuration of field emission measurement setup.

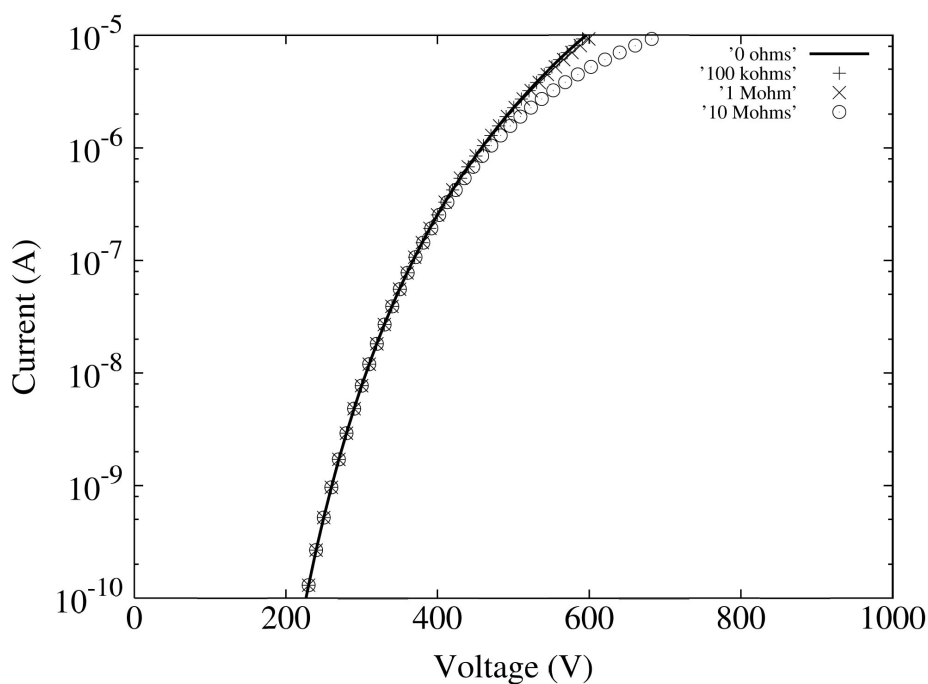


**Figure 3.3** Field emission current voltage curves calculated for various values of resistance in series. Significant deviations from the ideal (zero resistance) do not occur for a resistance less than 10 Mega Ohms.

In acquiring current as a function of voltage, the *threshold voltage* was defined as the voltage at which 0.1 nA of current was extracted from the cathode; this being the lower limit of the instrumentation used to measure current. Maximum current was usually limited to one microamp for molybdenum samples and 0.1 microamps for aluminum samples, to avoid irreversible damage to the emitter, unless specific studies were being conducted to determine current at failure (an example of a molybdenum tip after undergoing failure is shown in Figure 3.4). Furthermore, prior to current voltage data being taken, the field emission tips underwent a *break-in* period, whereby a large current

(approaching the failure current) was extracted over a period of several hours to ensure emission stability and desorption of surface impurities. An example of such a break-in is given in Figure 3.5, where 2 microamps were extracted from a molybdenum field emitter over a period of ~18 hours.

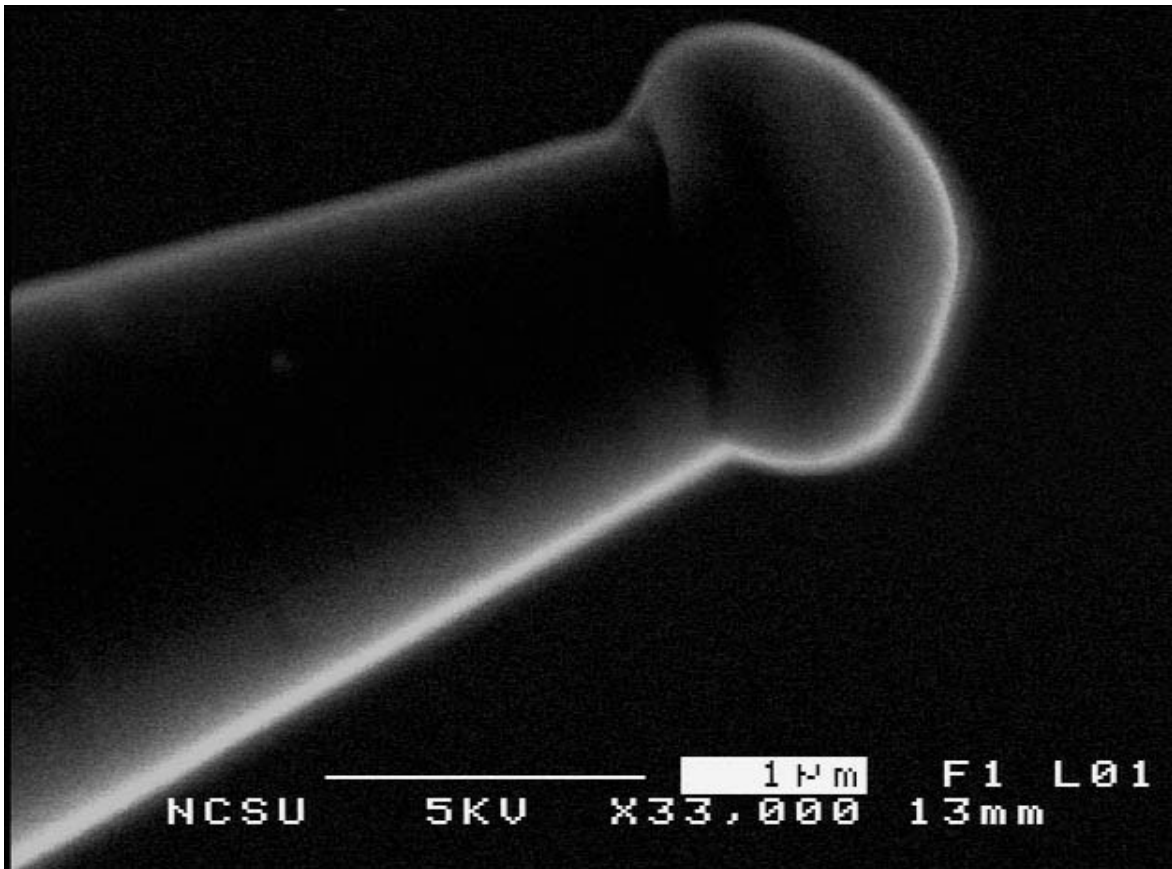


**Figure 3.4** Molybdenum field emission tip after undergoing irreversible damage (generation of excessive heat at high current densities melted the emitter).

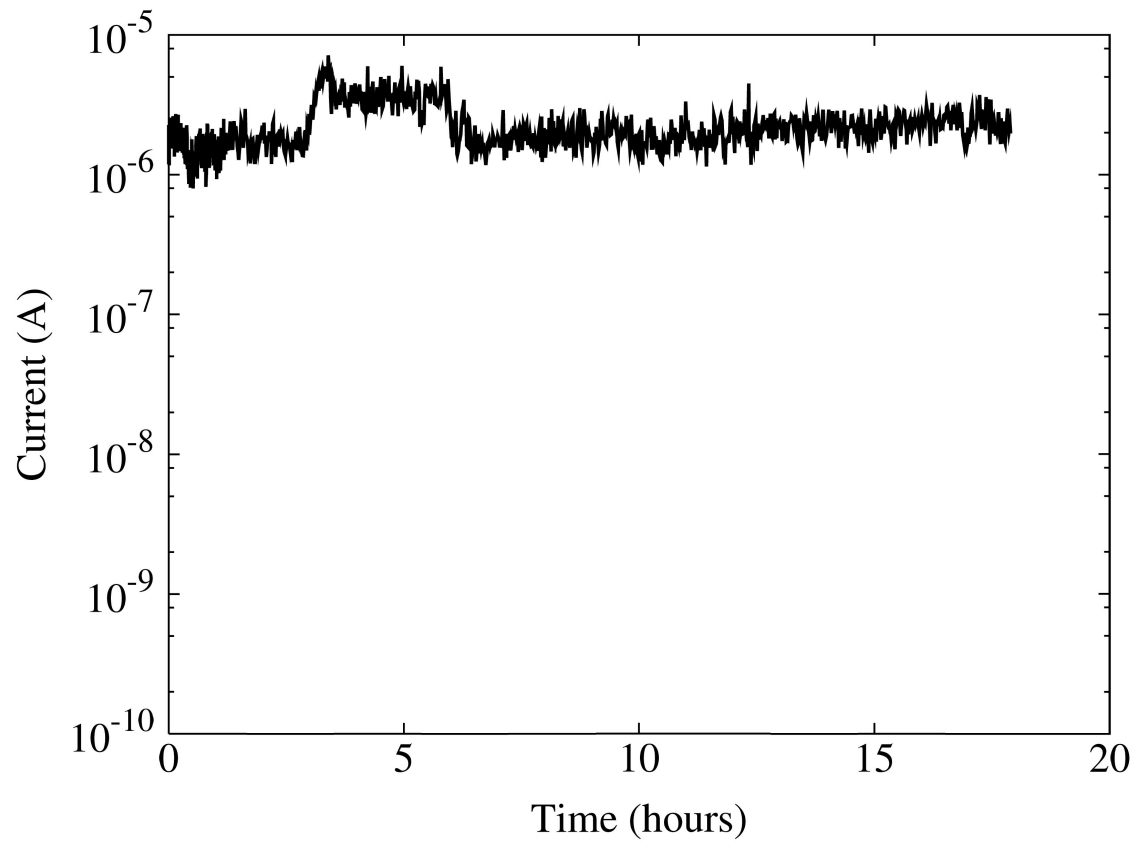


**Figure 3.5** Field emission *break-in* period for a molybdenum field emitter.

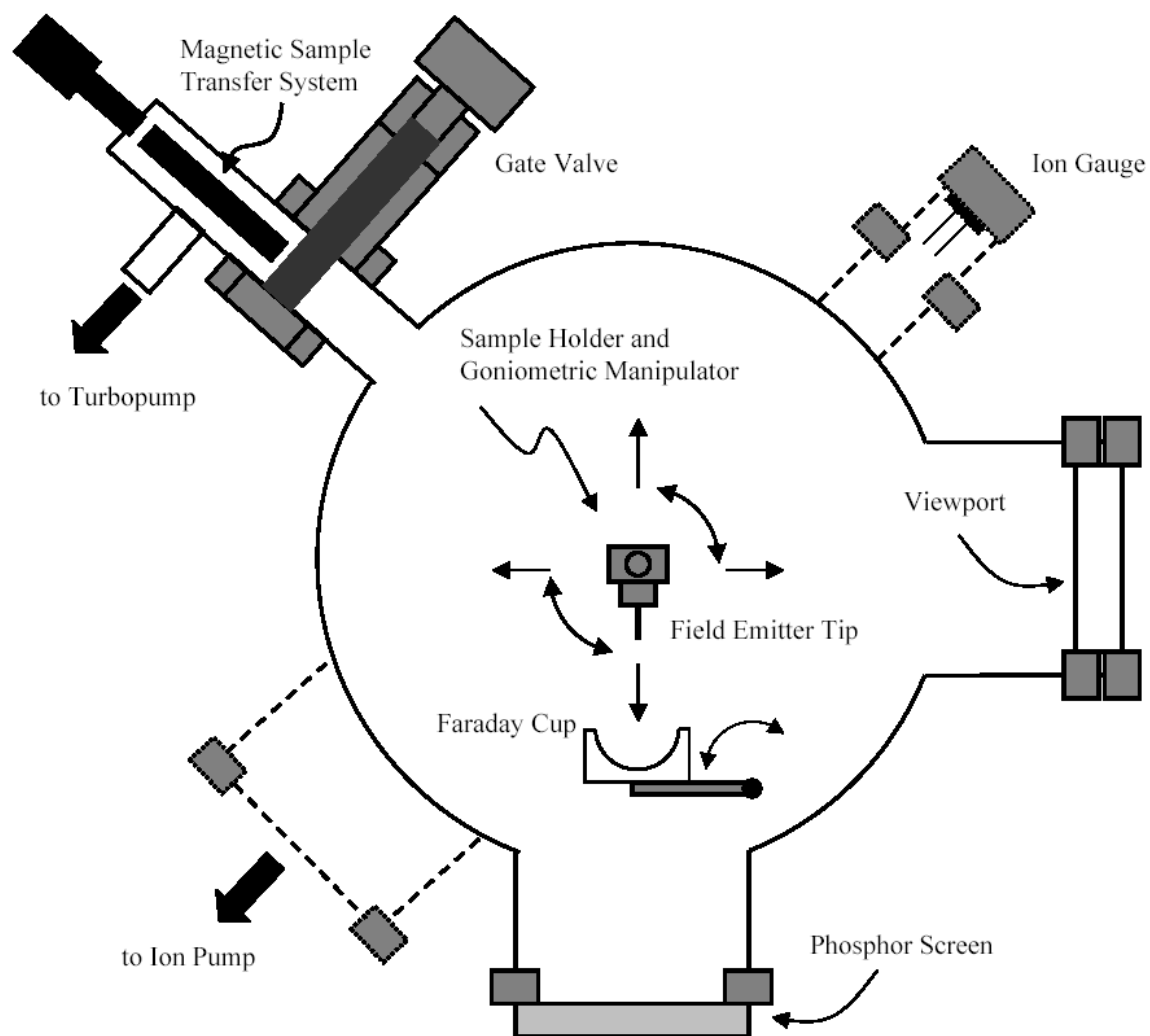


**Figure 3.6** Schematic of vacuum chamber and components used for field emission and field emission microscopy measurements.

### **3.3 SCANNING ELECTRON MICROSCOPY**

A JEOL 6400F field emission scanning electron microscope was used in this work for initial sample characterization. The resolution of this SEM, when operated at 20kV, is  $\sim 3$ nm. As such, the SEM provides insufficient resolution to characterize individual nanodiamond particles. However, the microscope's capacity to hold large numbers of samples (more than 30) made it useful in quickly identifying samples not suitable for field emission (i.e. tips with curvature radii greater than  $\sim 100$ nm). The SEM was thus primarily used for selecting samples with good potential as field emitters (e.g. see Figure 2.2). The SEM was also employed to help identify conditions for optimum diamond deposition. The high sample throughput of the SEM as compared to TEM made it the preferred method for quickly determining the deposition conditions which result in minimum amounts of deposited diamond (e.g. see Figure 2.7).

### **3.4 FIELD EMISSION MICROSCOPY**

#### **3.4.1 The Field Emission Microscope: Theory of Operation**

In 1936, after adding a simple metal heater loop to facilitate the outgasing of a needle-shaped cathode, Erwin W. Müller obtained the first stable field emission images; the field emission microscope was born [1,2]. This new device allowed for direct observation of microscopic crystallographic features, molecules, and even single atoms. The potential was immediately recognized, and the field emission microscope has been a powerful tool in the field of surface science for more than sixty years.

The field emission microscope (FEM) is fairly straightforward in both its design and operation. In its basic form, the FEM consists of a pointed source (the field emitter), the surface of which is the sample under study, positioned in vacuum a distance (on the order of centimeters) from an imaging screen. The screen (typically phosphor-coated) is biased positively (usually grounded) with respect to the emitter, which is negatively biased (Figure 3.7).

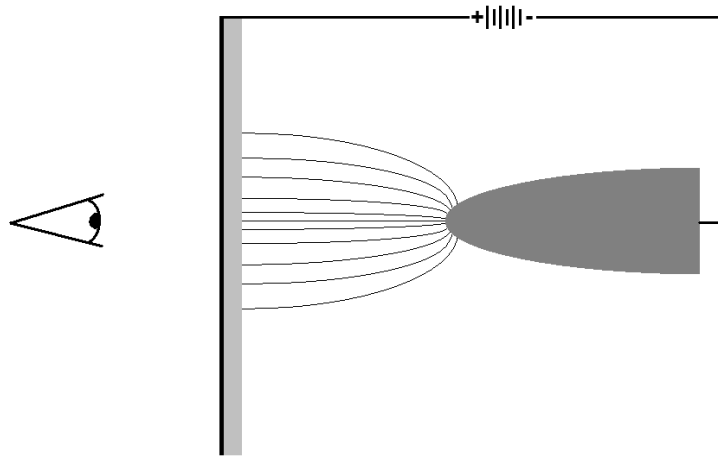


**Figure 3.7** Schematic of field emission microscope, indicating emitter, bias, and imaging screen.

In the presence of a sufficiently intense electric field ( $\sim 5 \text{ V/nm}$ ), a measurable amount of current is extracted from the cathode. The electrons follow an approximately radial path, outward toward the positively biased imaging screen. The electrons excite the phosphor coating on the imaging screen, and the result is a directly observable *image* of the emitting cathode surface. With emitting cathodes having radii of curvature ( $r$ ) less than

100nm, and the imaging screen being a distance ( $R$ ) centimeters away, the magnification,  $M$ , given in equation (3.2), can easily reach  $10^6$ . The  $\beta$  term is an *image compression* factor ( $\sim 1.5$ ) and is a consequence of the electrons not following an ideal radial path (a geometry of perfect concentric spheres would result in a  $\beta$  value of unity).

$$M \approx R/(\beta r) \quad (3.2)$$

The resolution of the FEM is limited by two factors: transverse electron motion and diffraction effects [3]. The transverse energy component  $\varepsilon_t$  of emitted electrons serves to limit the resolution by broadening what otherwise would be a point source (originating from the cathode surface) into a *disc* of diameter  $\delta_t$ , given by equation (3.3), where  $r_t$  is the emitter radius and  $V$  is the applied voltage.

$$\delta_t = 4r_t\beta(\varepsilon_t / eV)^{1/2} \quad (3.3)$$

Diffraction effects further limit resolution, where the emitting source (e.g. an emission site such as a single atom) acts as an aperture to the passing electron wave. The contribution due to diffraction is given in equation (3.4), where  $e$  is the elementary charge and  $m$  the electron rest mass.

$$\delta_{diff} = 2 \left[ \frac{r_t \beta \hbar}{(2emV)^{1/2}} \right]^{1/2} \quad (3.4)$$

The total minimum resolvable object diameter is the sum of equations (3.3) and (3.4). The resulting resolution limit is  $\sim 20\text{\AA}$  for cathodes with radii  $\sim 100\text{nm}$ , and for very sharp tips resolution can reach  $10\text{\AA}$  [3].

Some of the earliest studies involving the FEM made clear how this tool could be exploited; nanometer scale crystallographic regions were observed from various materials, including tungsten, molybdenum, nickel, and copper [2,4]. The potential for measuring activation energies for surface diffusion was realized after evaporating barium onto one side of a cathode, then subsequently heating the cathode during imaging [4]; the initial half-moon image was observed to change with increasing temperature, eventually resulting in full coverage of the cathode by the barium. Self-migration was later measured on tungsten tips; by varying cathode temperature and observing the disappearance of evaporated materials from the surface and field-induced tip deformations, activation energies for surface migration were determined [5]. The field emission microscope has been used in countless studies, including surface reconstruction, adsorption/desorption, and field emission site distribution, on a number of materials, including many metals and oxides, and more recently carbon nanotubes [6-15].

### **3.4.2 Experimental Setup**

Field emission microscopy was performed in the same system, as were field emission current measurements. The faraday cup used as the anode in field emission measurements was attached to a rotary feed-through, allowing it to be moved so as to provide a clear line of sight from the field emitter tip to the imaging screen, with a tip-to-

screen distance of 15cm (Figure 3.6). Negative bias was applied to the field emitter tip as before, with the phosphor-coated imaging screen at ground. A digital camera was used to capture images for later analysis.

### 3.5 TRANSMISSION ELECTRON MICROSCOPY

The sub-nanometer resolution achievable with the transmission electron microscope makes it an invaluable tool in studying nanoscale materials. Such resolution is necessary in field emission studies if any correlations are to be made between field emission measurements and morphology or composition at and near the emitting surface. A JEOL 2010F TEM was used to characterize samples in this study both before and after emission and deposition of nanodiamond. A custom sample holder (Figure 3.8) provided the means to perform non-destructive TEM analysis, where a copper arm tightened by two screws held the needle-shaped samples in place, making *before and after* studies possible.

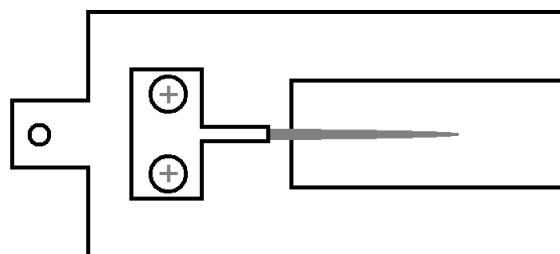


**Figure 3.8** Schematic of custom sample holder used for non-destructive TEM analysis of needle-shaped field emitters.

### 3.6 ELECTRON ENERGY LOSS SPECTROMETRY

Measuring morphology of a field emitter sample can provide a great deal of insight into specifics concerning emission mechanisms responsible for emitted currents.

However, when dealing with materials other than atomically clean metal surfaces, whose properties are *ideal* for the purposes of explaining emission behavior (i.e. in terms of the Fowler-Nordheim model), compositional analysis of the emitter is necessary. Surface adsorbates and oxides can have tremendous effects on emission (9, 15, 16), and compositional analysis of any coatings on the emitter surface is crucial; specific properties of coatings (e.g. whether they are conducting) must be determined in order to understand emission mechanisms. Furthermore, the analysis must provide resolution that is of the same size scale at which emission occurs, this requires sub-nanometer compositional analysis. Electron energy loss spectrometry was employed in this work to address this need for compositional information at the sub-nanometer scale.

When electrons pass through a sample, interacting with it inelastically, they exit the sample with energy less than that with which they entered; the analysis of these electrons (i.e. the energy they lost) can reveal a great deal about the composition of the sample. The *counting* of these electrons at various energy losses to form spectra is the basis of EELS. Collecting EELS spectra in the JEOL 2010F is accomplished with a parallel-collection magnetic prism spectrometer located below the viewing screen. As electrons pass through the sample and travel down the column into the magnetic prism, they are deflected varying amounts (depending on their kinetic energy) in the presence of the magnetic field; upon passing through the prism, the electrons are detected (counted) with a diode array interfaced with a computer for storing the spectra. The energy resolution of the

spectrometer, limited by the electron source, is  $\sim 0.3$  eV, which is sufficient not only to provide compositional information, but also bonding information.

### **3.7 SUMMARY**

The characterization techniques utilized in this work, field electron emission (FE), field emission microscopy (FEM), scanning electron microscopy (SEM), x-ray energy dispersive spectroscopy (EDS), transmission electron microscopy (TEM), and electron energy loss spectrometry (EELS), allowed for non-destructive analysis of isolated nanodiamond particles when deposited on ultra-sharp metal substrates. Electrical characterization, combined with sub-nanometer morphological and compositional analysis, can be carried out in any order and an arbitrary number of times. The use of these techniques in conjunction with each other makes for a powerful materials characterization scheme, which was employed in this research to investigate the properties of nano-meter scale diamond particles.

### 3.8 REFERENCES

- 1 E. W. Mueller, *Beobachtungen über die Feldemission und die Kathodenzerstäubung an thoriertem Wolfram*. Zeitschrift für Physik **106** 172 (1937).
- 2 E. W. Mueller, *Elektronenmikroskopische Beobachtungen von Feldekathoden*. Zeitschrift für Physik **106** 541 (1937).
- 3 E. W. Mueller, *The Imaging Process in Field Ion Microscopy From the FEM to the Atom-Probe*. CRC Critical Reviews in Solid State Sciences, **6** 85 (1976).
- 4 E. W. Mueller, *Weitere Beobachtungen mit dem Feldelektronenmikroskop*. Zeitschrift für Physik **108** 668 (1938).
- 5 E. W. Mueller, *Oberflächenwanderung von Wolfram auf dem eigenen Kristallgitter*. Zeitschrift für Physik **126** 642 (1949).
- 6 R. Gomer, *Field Emission and Field Ionization*, Harvard University, Cambridge, MA (1961).
- 7 E. W. Mueller and T. T. Tsong, *Field Ion Microscopy: Principles and Applications*. Elsevier, New York (1969).
- 8 J. P. Jones, *The Adsorption of Copper on Tungsten*. Proceedings of the Royal Society of London - A **284** (1399) 469-487 (1965).
- 9 P. Schwoebel and G. Hanson, *Localized Field Ion Emission Using Adsorbed Hydrogen Films on <111>-oriented Tungsten Field Emitters*. Journal of Applied Physics **56** (7) 2101-2105 (1984).

- 10 T. Shiota, M. Umeno, K. Dohkuni, M. Tagawa, and N. Ohmae, *Direct Observation of the Field-Stimulated Exoemission Sites at Tungsten Surface Using Field Ion Microscopy*. Journal of Applied Physics **89** (9) 5177 (2001).
- 11 A. Cetronio and J. P. Jones, *Reconstruction at a Metallic Interface Studied by Field Ion and Field Emission Microscopy*. Surface Science **40** 227 (1973).
- 12 B. R. Chalamala and R. H. Reuss, *Field Emission Characteristics of Iridium Oxide Tips*. Journal of Applied Physics **91** (9) 6141 (2002).
- 13 K. A. Dean and B. R. Chalamala, *Field Emission Microscopy of Carbon Nanotube Caps*. Journal of Applied Physics **85** (7) 3832 (1991).
- 14 K. A. Dean and B. R. Chalamala, *Current Saturation Mechanisms in Carbon Nanotube Field Emitters*. Applied Physics Letters **76** (3) 375 (2000).
- 15 K. A. Hata, A. Takakura, and Y. Saito, *Field Emission from Carbon Nanotubes with Clean Surface and Adsorbed Molecules*. AIP Conference Proceedings **590** 113 (2001).
- 16 G. Yang and K. Ken Chin, *Electron Field Emission Through a Very Thin Oxide Layer*. IEEE Transactions on Electron Devices, **38** (10) 2373-2376 (1991).

## CHAPTER 4

### NANODIAMOND ON MOLYBDENUM

#### 4.1 ABSTRACT

Single-crystalline diamond nanoparticles ( $\sim 5$  nm in scale) have been deposited onto molybdenum needles (with radii  $< 100$ nm), and their effects on field emission behavior were measured. Combined transmission electron microscopy observations, field emission measurements, and diamond depositions allowed for direct comparison of the effects of various amounts of nanodiamond coating on the field emission properties of a coated metal field emitter. In the limit, field emission from a single isolated diamond nanoparticle is compared here with that from an uncoated metal emitter and from a coating comprised of several layers of nanoparticles. A model for the observed dependence of emission behavior on the amount of deposited diamond is presented.

## 4.2 INTRODUCTION

Numerous groups have carried out extensive studies of electron emission from diamond over the past several years [1-6], with the first studies of diamond on pointed emitters having been conducted more than a decade ago [7]. In spite of a considerable number of experimental observations and significant theoretical effort, many of the observed emission phenomena are still not understood. It was observed experimentally that coating metal field emitters with diamond films could significantly enhance electron emission. At first, this result appeared counterintuitive. After all, why should putting a dielectric material on top of a conductor make the cold electron emission better rather than worse? This fundamental question is still not entirely resolved. Several explanations have been offered, including negative electron affinity of a diamond surface [2,3,5], emission from conductive surface protrusions on the diamond [4], non-diamond sp<sup>2</sup> inclusions (e.g. graphite) [2], and electron injection at the metal (i.e. back contact) -diamond interface [3,5]. However there remain several obstacles to fully understanding emission from diamond. Experimental results on emission from diamond have been from rather large objects, e.g. multicrystalline diamond films, which are complex materials containing many crystallites, grain boundaries, non-diamond inclusions, impurities, etc. As a consequence, there are multiple emission mechanisms, which depend upon a large number of factors. In this work, an attempt was made to reduce the possible variables by performing experiments with controlled deposits of nanodiamond particles with an individual size of about 5nm. Both the geometry of the underlying metal surface and the diamond particle were observed with atomic resolution in a transmission electron microscope (TEM) before

and after field emission experiments. In the experiments reported here, isolated diamond nanoparticles were deposited onto metal tips, characterized by field emission measurements, and then the resulting data compared to that of the bare metal tip before deposition (on the same specimen).

### **4.3 EXPERIMENTAL**

#### **4.3.1 Sample Preparation**

Sharp, needle-shaped emitters with radii of ~20-100 nm were prepared by electrochemical etching and deposited with diamond as described in Chapter 2. The explosive-type nanodiamond (ND) particles, also called Ultra Dispersed Diamond [8], used in these experiments were 2-5 nm in size. The resulting assembly of nanodiamond particles depended predictably upon applied voltage, suspension concentration, pulse duration, and tip geometry. By employing controlled millisecond pulses, preparing field emitters with either isolated nanodiamond particles, or continuous polycrystalline deposits of varying thickness was possible. In the present study, the reported results are limited to two extremes: a single diamond particle and a thick nanodiamond coating both deposited onto the same metal tip.

#### **4.3.2 Field Emission Measurements**

Field emission measurements were conducted with a Faraday cup as an anode, with a tip to anode spacing of ~10 mm. The vacuum in the chamber during measurements was  $\sim 10^{-9}$  torr. The field emission current-voltage (I-V) characteristics were measured from the same sample with increasing amounts of electrophoretically deposited diamond.

Electrometers interfaced with a PC were used to automate the data acquisition, ramping the voltage between the defined limits (0.1 nanoamps to 1 microamp).

### 4.3.3 Transmission Electron Microscopy Studies

The structure and morphology of the metal tips with and without nanodiamond coatings were investigated at high resolution using a JEOL 2010F TEM, both before and after field emission measurements. A TEM image of an isolated nanoparticle of diamond on a molybdenum tip is shown in Figure 4.1 (this micrograph was taken following emission measurements).

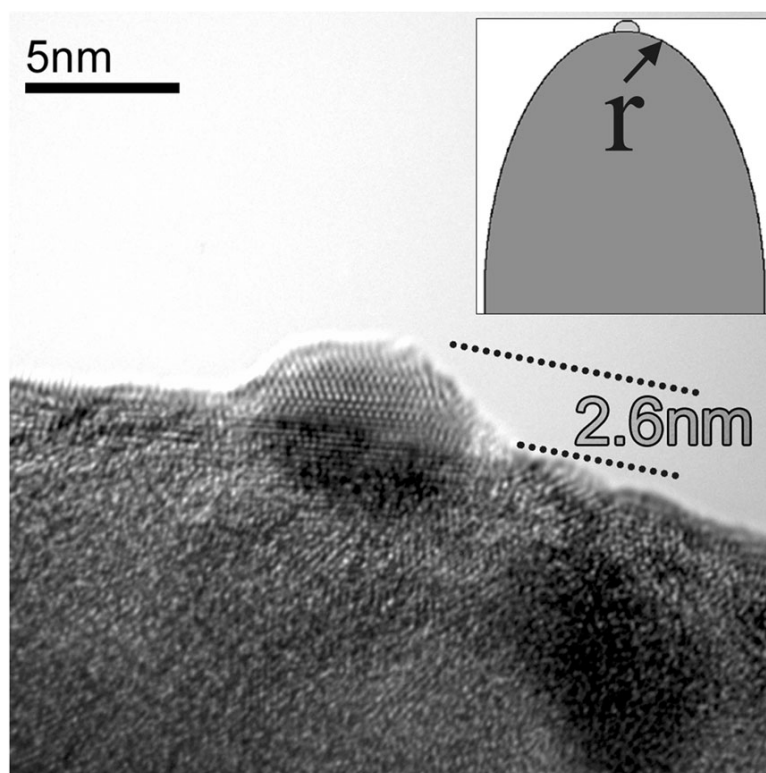


**Figure 4.1** High-resolution transmission electron micrograph of an isolated nanoparticle of diamond on the surface of a molybdenum tip of radius of curvature  $r=50\text{nm}$ .

## 4.4 RESULTS

### 4.4.1 TEM

The results of the TEM observations can be summarized as follows:

1. The geometry of the metal tip showed no measurable changes after emission.
2. The nature of the contact between diamond nanoparticles and the metal tip changed after emission. Before emission, clusters of loosely bound nanodiamond particles were observed on the Mo surface. But after emission, diamond particles (which were all about 5 nm in size) were distributed across the tip surface and apparently tightly bound (possibly embedded) to the underlying substrate (see Figure 4.1).
3. No indication of a graphite phase (sp<sup>2</sup> bonding) was found in the nanodiamond using a high resolution EELS probe (Figure 4.2 ). The sp<sup>2</sup> bond that corresponds to the graphite phase of carbon occurs at about 285eV in the reference spectrum and is not detectable in the EELS spectrum of the ND particle; however, the fine structure of the sp<sup>3</sup> bond, corresponding to the diamond phase, is strongly present (in the range of about 295 eV to 350 eV), indicating that the nanodots are completely carbon in the diamond phase.

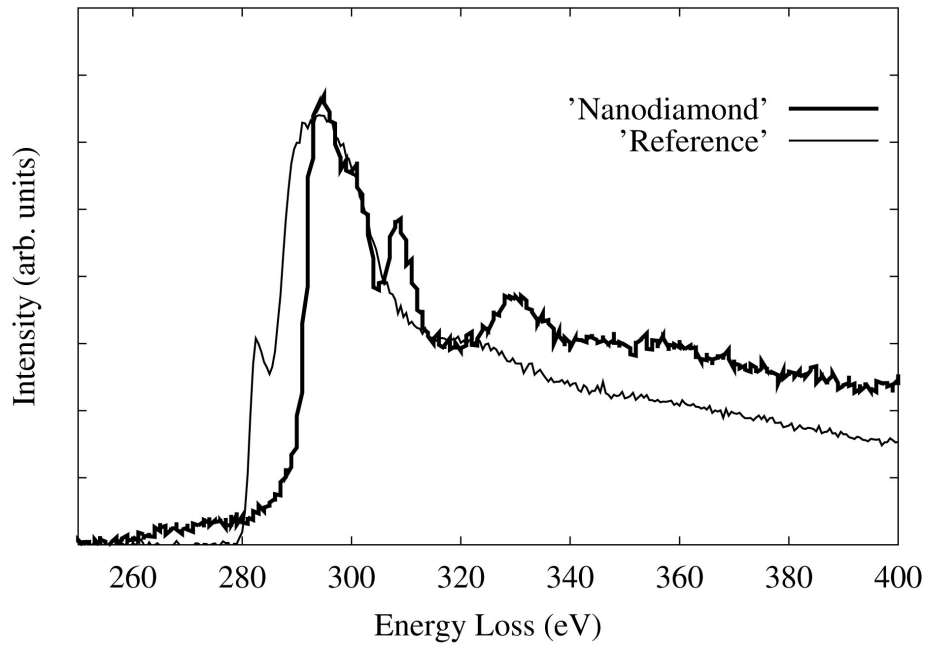


**Figure 4.2** EELS spectrum of nanodiamond particles, compared to standard carbon reference spectrum.

#### 4.4.2 Field Emission

Figure 4.3 summarizes a comparison of three I-V curves from: (1) a bare Mo tip, (2) the same tip after deposition of a single nanodiamond particle (Figure 4.1), and (3) the same sample after repeated deposition resulting in a polycrystalline nanodiamond layer of ~20 nm thickness.

The emission parameters used for this comparison were the emission threshold  $V_{th}$  (corresponding to an emission current of 0.1 nA), and the integral transconductance:

$$g = \frac{I_{\max} - I_{th}}{V_{\max} - V_{th}} \quad (4.1)$$

which is a measure of the average ‘steepness’ of the I-V curve. However, since the current limits are arbitrarily set ( $I_{\max}=1\mu\text{A}$ ,  $I_{\min}=1\text{nA}$ ), the use of the *integral transconductance* is meaningful only for qualitative comparisons between similar samples, and should not be considered a universal *figure of merit*.

Comparing the I-V curves of the bare Mo tip with the same tip with a deposit of one isolated diamond nanoparticle yields a substantial *increase* (~30%) in threshold voltage and the emission curve exhibits *non Fowler-Nordheim behavior* (see the I-V plot in Figure 4.3). However, after the additional deposition of nanodiamond and the formation of a thicker ND film, a *drastic decrease in threshold voltage* (~50%) and an *increase in transconductance* (~115%) are obvious (Figure 4.3). The emission threshold was also below 100 volts for the latter, which is unusually low for a tip-to-anode distance of 1 cm.

Nanodiamond thickness-dependent I-V measurements were performed on several samples with different curvature radii and, correspondingly, different threshold voltages. The range of threshold voltages of bare Mo tips was 170-460 V. In spite of such large differences in threshold voltage, the transconductance of all bare samples was 6.5-8 nA/V, 6-7 nA/V (5-7 % decrease) for isolated ND particles, and 14-17 nA/V (108-115% increase) for ND film. Therefore, the transconductance was found to be a characteristic parameter of coated emitter, relatively independent of variations in geometry. The threshold voltage increased by 20-30% for isolated ND particles, and decreased 20-60 % for the ND film, as compared to the bare tip.

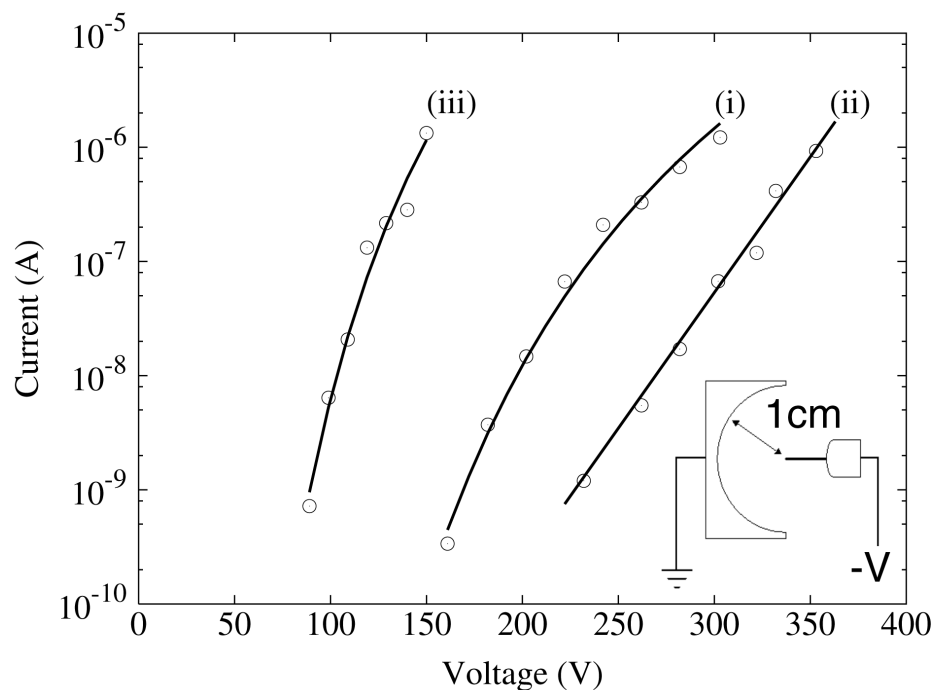


**Figure 4.3** Field emission characteristics from a bare metal tip (i), the tip with a single nanodiamond particle (ii), and the same tip with a nanodiamond film (iii). Inset: schematic of tip-to-anode geometry.

## 4.5 DISCUSSION

### 4.5.1 TEM Studies

High-resolution transmission electron microscopy did not reveal any measurable changes in the emitter geometry, which could account for the observed changes in emission, e.g. no atomic-scale protrusions were observed. Furthermore, no specific features could be seen within the diamond particle, such as non-diamond inclusions or conductive filaments. It was thus concluded that changes in the measured emission properties cannot be explained by such structural changes (as is often suggested [2,9]), but must be due to changes in the electronic properties of the diamond nanoparticles or to

subtle changes at the interfaces between the particle with the metal substrate and/or with the vacuum.

#### **4.5.2 Apparent Work Function and Emission Area**

As discussed in reference [10], the work function and emission area derived from the field emission characteristics employing the Fowler-Nordheim formalism may significantly differ from their actual values. It is thus preferable to use the terms “apparent” or “effective” (work function or area) to emphasize this distinction. The apparent work function and emission area are important tools for relative comparisons of emission properties, since these parameters are functions of the electronic properties of the emitting materials [5].

The structure of Figure 4.1 gives a nearly atomic scale measure of the geometrical parameters of the emitting surface, e.g. physical curvature radius, total area of the diamond nanoparticle, etc. These measures of the nanodiamond emitter, experimental emission parameters, and the values for the apparent work function, as well as the square root of the emission area are summarized in Table 4.1.

**Table 4.1** Geometrical and emission characteristics of molybdenum field emitter with varying amounts of nanodiamond.

Characteristics		Bare Mo	Particle	ND film
Geometrical	Metal tip radius (TEM)	50 nm	50nm	50 nm
	ND Thickness (TEM)	0 nm	2.3 nm	20 nm
Field Emission	$V_{\text{threshold}}$	172 V	222 V	89 V
	$g$	7.63 nA/V	7.09 nA/V	16.4 nA/V
	I-V best fit	<i>F-N:</i> $I(V) = AV^2 \exp(-B/V)$	Not F-N: $I(V) = a \exp(bV)$	<i>F-N:</i> $I(V) = AV^2 \exp(-B/V)$
Fowler-Nordheim Analysis	Work function	4.05 eV	5.57 eV	2.71 eV
	$\sqrt{\alpha}$ (F-N)	1.4 nm	5.7 nm	1.9 nm

#### 4.5.3 The Thickness Effect

It has been experimentally observed that the emission voltage of diamond-coated emitters decreased with decreasing thickness of the diamond coating [11]. These previous experiments were carried out with diamond thickness ranging from 50 nm to 2  $\mu\text{m}$  and these observations are sometimes referred to as the “normal” thickness effect. Typical explanations of such behavior have been associated with the resistive voltage drop across the films or to negative space charge within the insulating diamond coating [11]. One might project that this trend would continue as the diamond coatings became even thinner. However, as Figure 4.3 shows, the deposition of a single isolated diamond particle on a metal tip substantially *increases* the emission voltage, whereas further deposition of diamond particles drastically shifts the emission curve to a lower voltage (e.g. <100 V threshold, even at an emitter-to-anode distance of 1 cm). This behavior is herein referred to as the “anomalous” thickness effect. Recently, a similar anomalous thickness effect was

reported for field emitters coated with AlN of thickness 5-15 nm [12]. Both the bare metal emitter and the thicker continuous diamond film conform to the Fowler-Nordheim equation; i.e.  $I=AV^2 \exp(-B/V)$ . However, the form of the emission characteristics for the same metal emitter, with a single isolated nanodiamond particle follows a relationship given approximately by:  $I= a \exp(bV)$ , i.e. a straight line on a log scale (Figure 4.3). As yet, there is no physical model to explain these behaviors. Since the size of the diamond particle is only  $\sim 5$  nm, it is likely that quantum effects should be taken into account.

#### 4.5.4 Emission Barrier Increase

The observed differences in field emission behavior due to the deposition of a single diamond particle when compared to that of a thicker *film* suggests that some size-dependent materials properties may be at least partly responsible. When considering particles of less than  $\sim 5$  nm in diameter, the quantum nature of matter can become apparent, manifesting itself in a variety of ways [13-25]. One significant change that takes place in semiconductors is an increase in the bandgap energy, as discussed in Chapter 1, where the size-dependent bandgap for a spherical particle of radius R was given as:

$$E_{g,confined} = E_{g,bulk} + \frac{\hbar^2 \pi^2}{2R^2} \left[ \frac{1}{m_e^*} + \frac{1}{m_h^*} \right] \quad (4.2)$$

As particle dimensions shrink, the change in bandgap can be described using this *particle in a (spherical) box* model (Figure 4.4).

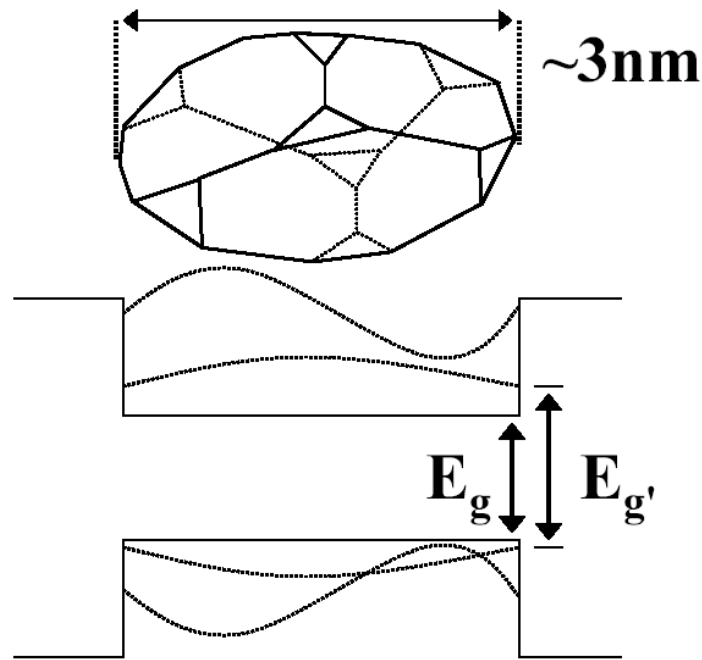


**Figure 4.4** Energy band diagram for a nanometer-size semiconductor; ground state and first excited state for holes and electrons are illustrated schematically. The increase in bandgap due to quantum confinement effects is shown.

According to equation (4.2), the increase in bandgap for a diamond particle 2.6-3nm in diameter (see Figure 4.1) is 1.4-1.1 eV. If one assumes the emission barrier for electrons injected into diamond from a metal to be half of the diamond bandgap ( $E_g=5.4\text{eV}$ ,  $E_{g,\text{confined}}=5.4\text{eV}+1.4\text{eV}$ ), then this translates into an emission barrier increase of up to 0.7 eV. Since field emission is so strongly dependent upon the height of the emission barrier, this can result in substantial suppression of emission. To illustrate this, two current-voltage curves are plotted in Figure 4.5 for ideal metal emitters with work functions

differing by 0.7 eV. Clearly, the increase in threshold voltage is considerable for a 0.7 eV increase in emission barrier.

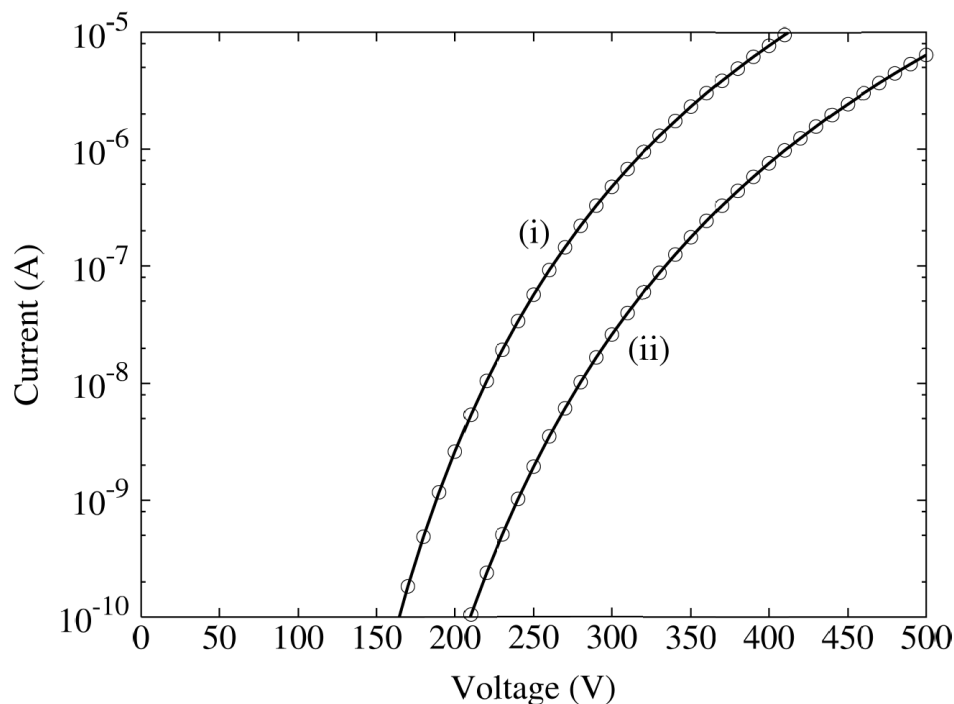


**Figure 4.5** Ideal field emission current from two hypothetical emitters differing only by their emission barriers, i) 4 eV and ii) 4.7 eV.

#### 4.5.5 Electrostatic Effects

In addition to size-dependent bandgap increase (and consequently emission barrier increase), size-dependent electrostatic effects can also contribute to the suppression of emission when considering nano-size particles. In Figure 4.6 the surface electrostatic fields were calculated (finite element method) for a *particle-on-tip* geometry, where a

dielectric particle is *placed* on a metal tip [26]. The fields at the metal-vacuum, metal-particle, and particle-vacuum interfaces are plotted. It can be seen that a *screening* effect takes place, which serves to reduce not only the electric field around the outer edge of the particle at the metal-vacuum interface, but also reduces the field around the inner perimeter of the particle at the metal-particle interface. This reduction in field is a consequence of the size of the particle, and is not seen for a uniform dielectric coating. This local reduction in electric field would serve to suppress emission, noting that the field emission current,  $I$ , is strongly dependent upon the electric field,  $F$ , i.e.  $I \sim \exp(-b/F)$ .

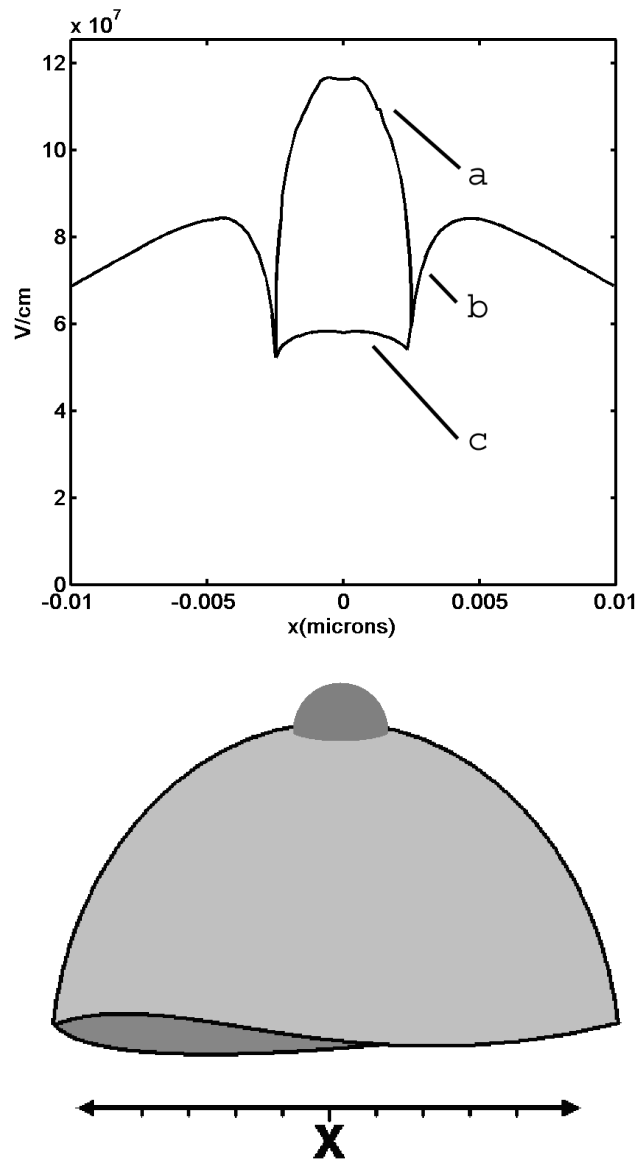


**Figure 4.6** Surface electrostatic field profile (top) computed for a *particle-on-tip* geometry (bottom) indicating the reduction of fields due to *screening* effects. Fields are plotted for a) particle-vacuum, b) metal-vacuum, and c) metal-particle interfaces.

## 4.6 CONCLUSION

Electron emission from a multi-particle nanodiamond coating and an isolated diamond nanoparticle has been measured. The emission characteristics were a complex function of coating thickness. Current-voltage curves shifted to a considerably higher voltage than for the metal substrate for single-particle coatings (a thickness of about 2.6 nm as measured by high resolution TEM) and the emission characteristics exhibited non Fowler-Nordheim behavior. However, for a thicker *film* of ~20 nm, with approximately uniform nanoparticle coverage, the I-V plot was sharply shifted to a voltage much lower than that for the uncoated metal substrate. After emission experiments, high resolution TEM did not reveal the formation of nano-protrusions or graphite inclusions in the diamond particle; however, the particle appeared to be in much better contact with the metal substrate than by deposition alone. The observed *anomalous thickness effect* (the suppression of emission upon deposition of a single diamond particle) is not completely understood, but a possible contribution to the increase in threshold voltage is the increase in the bandgap (and thus the emission barrier at the metal diamond interface) of the diamond particle due to quantum confinement effects. Further suppression of emission can be attributed to local electric field reduction due to electrostatic screening effects, a consequence of the size of the diamond nanoparticle.

Future work to include emission measurements from single isolated nanodiamond particles of varying size could lead to more insight concerning the emission mechanism, and could support the proposed model of bandgap increase and electrostatic screening. Additional experiments using the same samples with isolated diamond in contact mode in a

scanning tunneling microscope could provide complimentary electrical measurements, as could field emission energy distribution measurements and field emission microscopy.

#### 4.7 REFERENCES

- 1 C. Wang, A. Garcia, D. C. Ingram, M. Lake, M. E. Kordesch, *Cold field emission from CVD diamond films observed in emission electron microscopy*, Electronics Letters **27** 1459, (1991).
- 2 N. S. Xu, Y. Tzeng, and R. V. Latham, *Similarities in the 'cold' electron emission characteristics of diamond coated molybdenum electrodes and polished bulk graphite surfaces*, Journal of Physics D - Applied Physics **26**, 1776 (1993).
- 3 M. W. Geis, J. C. Twichell, T. M. Lyszczarz, *Diamond emitters fabrication and theory*, Journal of Vacuum Science and Technology B **14**, 2060 (1996).
- 4 V. V. Zhirnov, Givargizov E. I., Plekhanov P. S., *Field emission from silicon spikes with diamond coatings*, Journal of Vacuum Science and Technology B **13**, 418 (1995).
- 5 V. V. Zhirnov and J. J. Hren, MRS Bulletin **23**, 42 (1998).
- 6 T.A. Railkar, W.P. Kang, H. Windischmann, A.P. Malshe, H.A. Naseem, J.L. Davidson, W.D. Brown, Critical Rev. Solid State and Mat. Sci. **25**, 163 (2000).
- 7 J. Liu, V. Zhirnov, G. Wojak, A. Myers, W. Choi, J. Hren, S. Wolter, M. McClure, B. Stoner, and J. Glass,
- 8 N. R. Greiner , D. S. Phillips, J. D. Johnson, and F. Volk., Nature **333**, 440 (1988).
- 9 A. V. Karabutov, V. D. Frolov, and V. I. Konov, *Diamond/sp<sup>2</sup>-bonded carbon structures: quantum well field electron emission?*, Diamond and Related Mat. **10**, 840 (2001).

- 10 V.V. Zhirnov, C. Lizzul-Rinne, G.J. Wojak, R.C. Sanwald, J.J. Hren ,  
*“Standardization” of field emission measurements*, Journal of Vacuum Science and  
Technology B **19**, 87 (2001).
- 11 V.V. Zhirnov, C. Lizzul-Rinne, G.J. Wojak, R.C. Sanwald, J.J. Cuomo, J. J. Hren,  
*Optimizing high-current yields from diamond coated field emitters*, Journal of  
Vacuum Science and Technology B **19**, 17 (2001).
- 12 D. Kang, V. V. Zhirnov, R. C. Sanwald, J.J. Hren, and J.J. Cuomo, *Field Emission  
from Ultra Thin Coatings of AlN on Mo emitters*, Journal of Vacuum Science and  
Technology B **19**, 50 (2001).
- 13 L. E. Brus, *A Simple Model for the Ionization Potential, Electron Affinity, and  
Aqueous Redox Potentials of Small Semiconductor Crystallites*. Journal of  
Chemical Physics **79** (11) 5566 (1983).
- 14 L. E. Brus, *Electron-Electron and Electron-Hole Interactions in Small  
Semiconductor Crystallites: The Size Dependence of the Lowest Excited Electronic  
State*. Journal of Chemical Physics **80** (9) 4403 (1984).
- 15 R. T. Collins, P..M. Fauchet, and M.A. Tischler, *Porous Silicon: From  
Luminescence to LEDs*. Physics Today, **50** 24 (1997).
- 16 L. T. Canham, *Silicon Quantum Wire Array Fabrication by Electrochemical  
Dissolution of Wafers*. Applied Physics Letters, **57** 1046 (1990).
- 17 S. Vepřek, *Electronic and Mechanical Properties of Nanocrystalline Composites  
when Approaching Molecular Size*. Thin Solid Films **297** 145-153 (1997).
- 18 T. Trindade, *Nanocrystalline Semiconductors: Synthesis, Properties, and  
Perspectives*. Chemistry of Materials **13** 3843 (2001).

- 19 F. W. Wise, *Lead Salt Quantum Dots: The Limit of Strong Quantum Confinement*. *Accounts of Chemical Research* **33** (11) 773 (2000).
- 20 Y. A. Wang, W. Mahler, and R. Kasowski, *PbS in Polymers. From Molecules to Bulk Solids*. *Journal of Chemical Physics* **87** (12) 7315 (1987).
- 21 C. Q. Sun, T.P. Chen, B.K. Tay, S. Li, H. Huang, Y.B. Zhang, L.K. Pan, S.P. Lau, and X.W. Sun, *An Extended 'Quantum Confinement' Theory: Surface-coordination Imperfection Modifies the Entire Band Structure of a Nanosolid*. *Journal of Physics D: Applied Physics* **34** 3470 (2001).
- 22 R. Tsu, D. Babić, L. Ioriatti Jr., *Simple Model for the Dielectric Constant of Nanoscale Silicon Particle*. *Journal of Applied Physics* **82** (3) 1327 (1997).
- 23 L. W. Wang, and A. Zunger, *Pseudopotential Calculations of Nanoscale CdSe Quantum Dots*. *Physical Review B* **53** 9579 (1996).
- 24 L. W. Wang, and A. Zunger, *Dielectric Constants of Silicon Quantum Dots*. *Physical Review Letters* **73** 1039 (1994).
- 25 M. Lannoo, C. Delerue, and G. Allan, *Screening in Semiconductor Nanocrystallites and Its Consequences for Porous Silicon*. *Physical Review Letters* **74** 3415 (1995).
- 26 D. L. Jaeger, V. V. Zhirnov, and J. J. Hren, *Electrostatic Fields Affecting Metal Emitters Coated with Diamond Nanoparticles and Clusters*. 14<sup>th</sup> International Vacuum Microelectronics Conference (IVMC), Davis, CA, August 13<sup>th</sup>-16<sup>th</sup>, 2001.

## CHAPTER 5

### NANODIAMOND ON ALUMINUM

#### 5.1 ABSTRACT

Single-crystalline nanodiamond particles ( $\sim 5\text{nm}$  in diameter) have been deposited on an aluminum needle (curvature radius  $\sim 50\text{nm}$ ). Field emission current-voltage measurements were taken, as were field emission microscopy images. The changes in field emission behavior due to varying amounts of deposited diamond were investigated. The diamond nanoparticles and aluminum substrate were characterized in both scanning electron and transmission electron microscopes, compositional analysis was conducted using x-ray energy dispersive spectroscopy and electron energy loss spectrometry.

## 5.2 INTRODUCTION

For decades, refractory metals, namely tungsten and molybdenum, have been the choice materials for field emission cathodes [1-4]. Materials such as aluminum, with a low melting point and low hardness, have been avoided with the reasoning that such materials cannot withstand the extremely high current densities, potentially destructive local heating, and high stress due to large fields and field gradients present during field emission.

However, aluminum can withstand currents extracted from a single emitter in excess of 1 microamp (Figure 2.5) without failure (comparable to that of molybdenum emitters) and field emission studies from aluminum have been conducted (e.g. [5,6]), though such studies are small in number. Furthermore, it has been demonstrated that adding diamond to field emitters can raise the maximum current; this is attributed to the high thermal conductivity of diamond maintaining lower temperatures at the emitting surface [e.g 7].

When considering a material to serve as a field emission cathode, being a nano-scale device (field emission occurs at scales on the order of a nanometer), attention must be given to the material as well as the surface. In the case of aluminum, there exists a stable *native* oxide on the surface with a thickness of 3 to 5 nanometers. Some properties of aluminum and aluminum oxide are summarized in Table 5.1 [8-10]. When the scale of the aluminum sample approaches that of the native oxide, the properties of the oxide can influence the properties of the aluminum/aluminum-oxide *composite* [11,12]. A comparison of the properties of aluminum and its oxide (e.g. melting point and hardness) suggests that the robust nature of the oxide may facilitate the high current densities and high local fields (and field gradients) present during field emission.

In addition to withstanding field emission currents sufficiently large enough to conduct field emission studies, it was found that aluminum tends to etch with a higher *success rate* when compared to molybdenum (etched aluminum needles are in general more uniform with a higher percentage of samples forming curvature radii less than 100 nm and are more often *smooth* along the apex of the tip). The aluminum does not suffer from *unpredictable* oxide formation, as does molybdenum; the native oxide of aluminum forms reproducibly and reliably.

With aluminum serving as the substrate, diamond nanoparticles were deposited in varying amounts, from none (bare aluminum emitter) to a thin *film* (~6-8 nm). At each stage of diamond deposition, field emission current-voltage measurements were taken as well as field emission micrographs; transmission electron microscopy was also used at each stage of deposition as well as before and after field emission. Compositional analyses were conducted using EDS and EELS.

**Table 5.1** Comparison of physical properties of aluminum and aluminum oxide.

Property	Value		Units
	Aluminum	Al <sub>2</sub> O <sub>3</sub>	
Density	2.7	4.0	g/cm <sup>3</sup>
Elastic Modulus	69	370	GPa
Melting Temperature	660	2,015	°C
Hardness	2.75	9.0	Mohs scale

### 5.3 EXPERIMENTAL

#### 5.3.1 Sample Preparation

Sharp, needle-shaped emitters with radii of ~50 nm were prepared by electrochemical etching and varying amounts of nanodiamond particles were deposited as described in Chapter 2. The following experiments were conducted on a single aluminum emitter.

#### 5.3.2 Field Emission and Field Emission Microscopy

The field emission measurements were conducted as described in section 4.3.2. However, as a precaution, the defined maximum current was limited to 0.1 microamps for the aluminum emitter (as compared to 1 microamp for molybdenum) to avoid current-induced damage to the emitter. Vacuum conditions and tip-to-anode geometry were the same as for that of molybdenum:  $1\text{-}5\cdot 10^{-9}$  torr and 1cm radius hemispherical anode.

Field emission microscopy was performed at each stage of diamond deposition. The field emission micrographs were taken in the same system in which field emission current-voltage measurements were taken (Figure 3.6), with a tip-to-screen distance of 15cm. FEM images were obtained immediately after the current-voltage data was taken, and the images were captured with a digital camera.

### **5.3.3 Transmission and Scanning Electron Microscopy Studies**

The structure and morphology of the aluminum tip with and without nanodiamond coatings were investigated at high resolution using a JEOL 2010F TEM, both before and after field emission measurements. A TEM image of the aluminum needle used in this series of deposition and emission experiments is shown in Figure 5.1. Electron energy loss spectrometry was also conducted in the TEM.

Scanning electron microscopy was used to determine if diamond deposition occurred (prior to examining the specimen in the TEM). Also, x-ray energy dispersive spectroscopy was conducted in the SEM on the aluminum substrates for compositional analysis.

## **5.4 RESULTS**

### **5.4.1 Transmission Electron Microscopy**

The aluminum needle was examined in TEM a number of times during this series of experiments: after field emission and prior to diamond deposition, after a first diamond deposition and prior to field emission, and again after field emission, and finally after an additional diamond deposition and field emission experiment.

The bare aluminum needle, from which field emission I-V data was collected, was initially imaged in TEM to determine its morphology, in particular the radius of curvature at the emitter apex, and to determine whether damage was caused as a result of field emission. The electron micrograph in Figure 5.1 was used to determine the radius of curvature to be 50nm, and the micrograph also confirms that the emitter suffered no damage as a result of field emission.

The aluminum needle then underwent a first diamond deposition, after which the emitter was examined in SEM (Figure 5.2) to determine whether diamond was in fact deposited (SEM was used initially because it is less time consuming compared to TEM). Following SEM, the aluminum needle was then examined in TEM to more closely investigate the deposited diamond (Figures 5.3 and 5.4). The micrographs reveal clusters of loosely bound diamond particles distributed across the surface of the aluminum needle (the clusters were apparently loosely bound because of their observed motion under the influence of the electron beam in the TEM). The clusters have a tendency to decrease in size the closer they are located to the apex of the tip. This can be explained by the increased electric field (and field gradient) near the tip apex, which serves to de-agglomerate the nanodiamond clusters during deposition.

The diamond-coated needle then underwent field emission, and was again imaged in the TEM. The micrographs following emission (Figures 5.5, 5.6, and 5.7) reveal that most of the diamond was stripped from the emitter as a result of field emission; however, some amorphous carbon remained, which can be seen in Figures 5.6a and 5.6b at the nanoparticle-aluminum interface, and again in Figures 5.7f and 5.7g. Furthermore, the nanoparticles (appearing darker than the aluminum needle) marked in Figure 5.5 as *a-g*,

and imaged at higher magnification in Figures 5.6 and 5.7, were determined to be platinum, by electron energy loss spectrometry (Figure 5.8) and x-ray energy dispersive spectroscopy (Figure 5.9). The particle in Figure 5.7h, however, is apparently diamond, due to the difference in contrast to the platinum, as well as the lattice spacing. The source of the platinum was later determined to be an unwanted byproduct of the electrochemical etching process, where material from the platinum electrode used in etching was deposited onto the etched aluminum needle (see Appendix for more information regarding the deposition of platinum onto aluminum).

A second diamond deposition was performed, which was then followed by field emission current-voltage measurements as well as field emission microscopy. The emitter was then examined in TEM a final time. The micrographs (Figures 5.10, 5.11, and 5.12) indicate a thin diamond *film* was deposited, with a thickness of  $\sim 6-8$  nm, while larger diamond clusters appear away from the emitter apex.

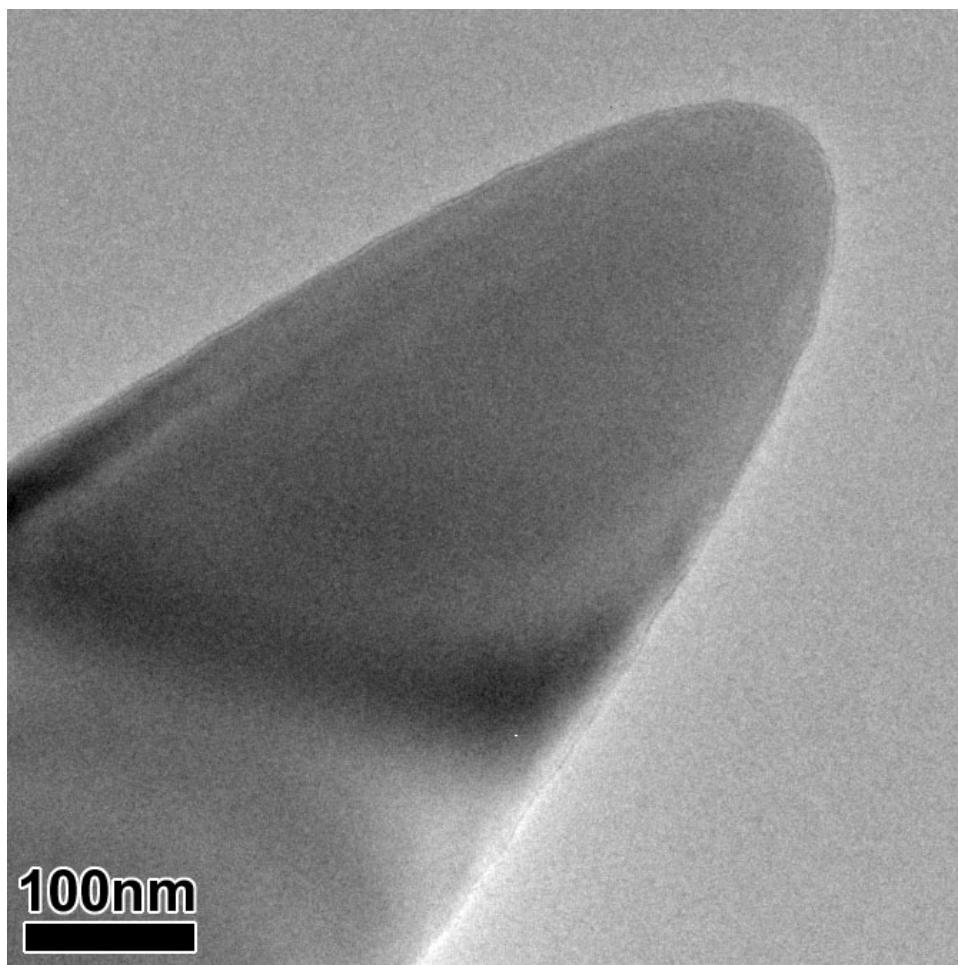


**Figure 5.1** Transmission electron micrograph of electrochemically etched aluminum needle after field emission.

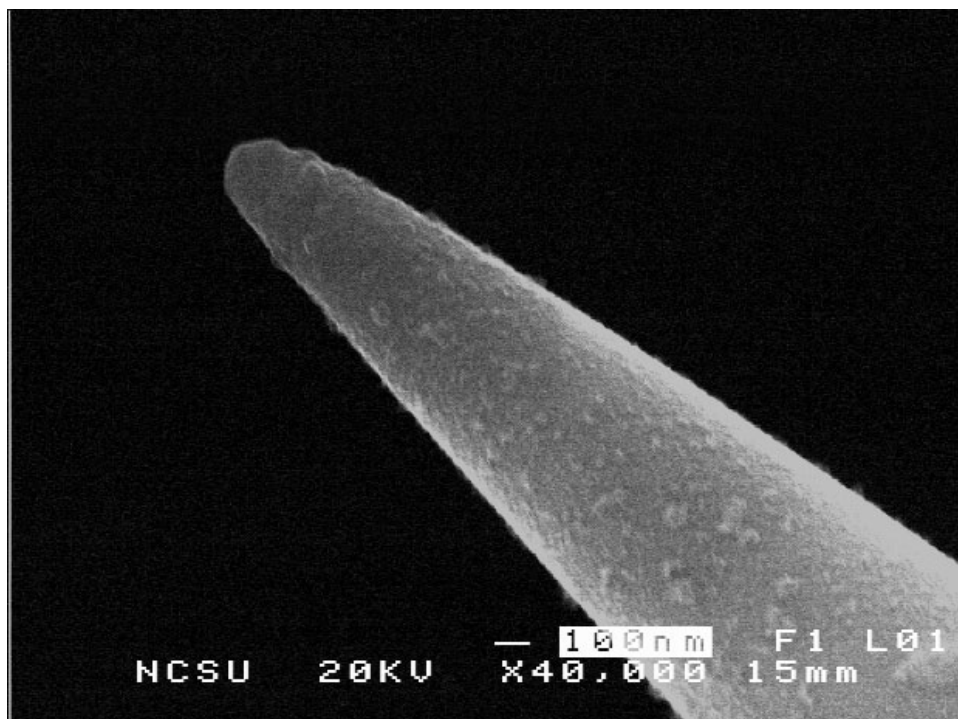


**Figure 5.2** Scanning electron micrograph of aluminum needle with electrophoretically deposited nanodiamond.

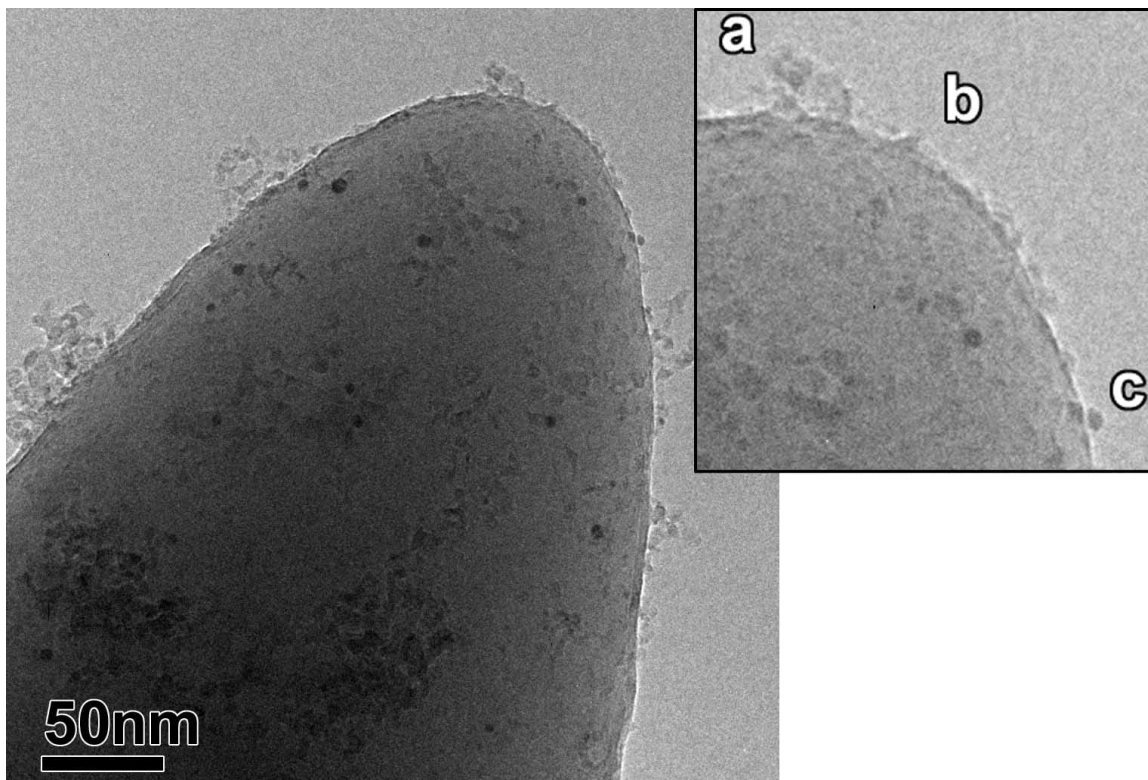


**Figure 5.3** Transmission electron micrograph of aluminum needle with electrophoretically deposited nanodiamond. Inset marks areas where higher magnification images were taken, which correspond to the micrographs in Figure 5.4.

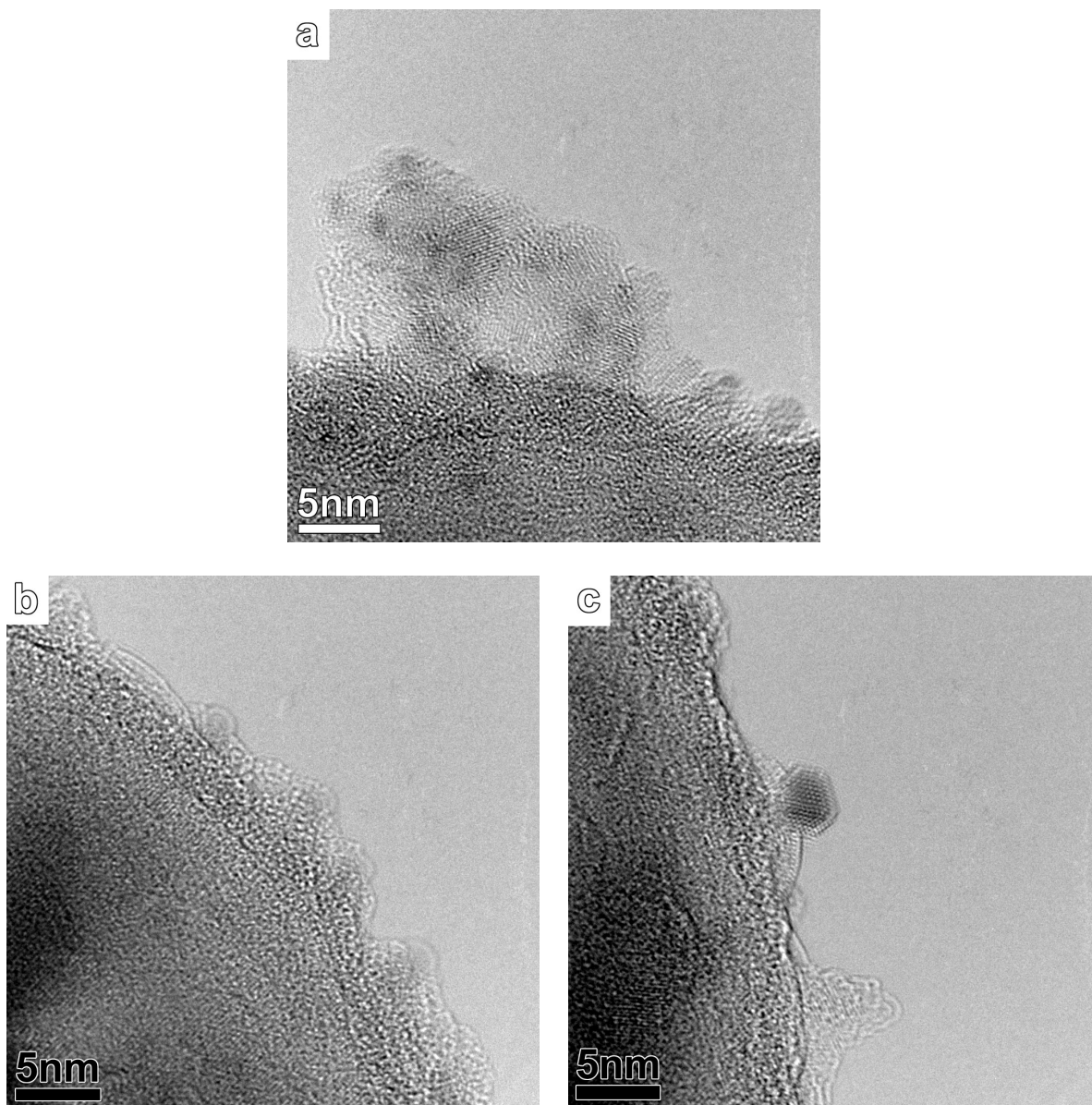


**Figure 5.4** Transmission electron micrographs of diamond-deposited aluminum needle, corresponding to areas marked in the inset in Figure 5.3.

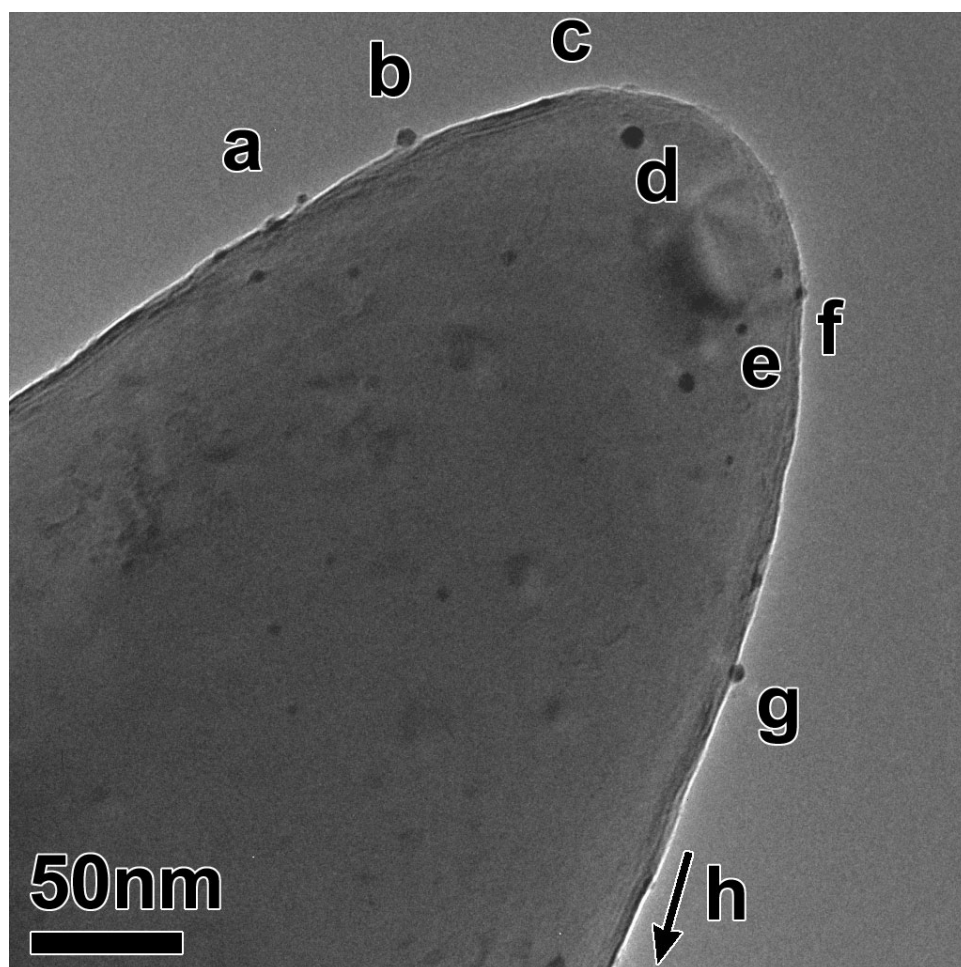


**Figure 5.5** Transmission electron micrograph of aluminum needle after undergoing nanodiamond deposition and field emission. Labels indicate areas where higher magnification images were taken, which correspond to the micrographs in Figures 5.6 and 5.7.

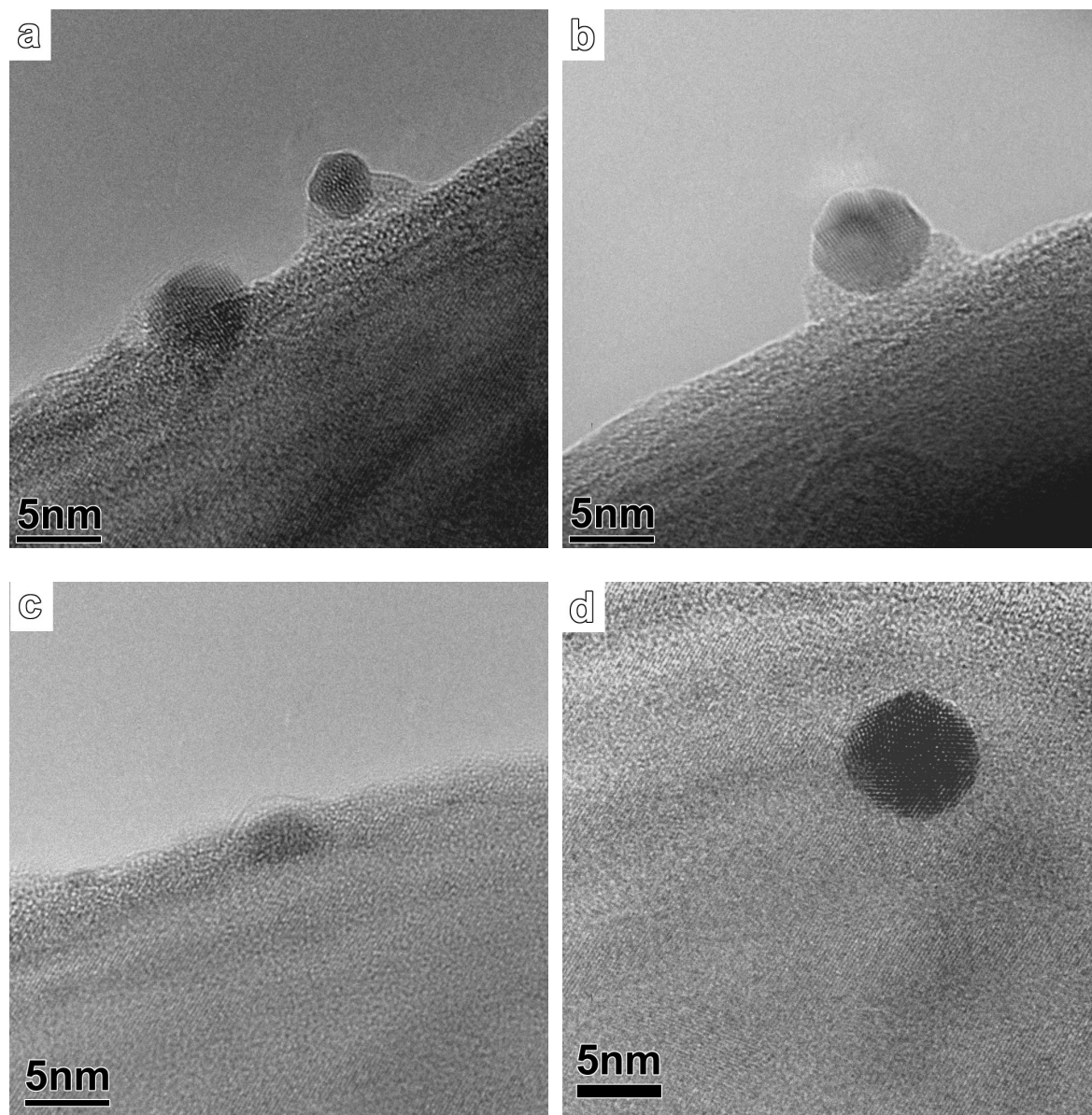


**Figure 5.6** Transmission electron micrographs corresponding to areas (a) – (d) marked on the image in Figure 5.5.

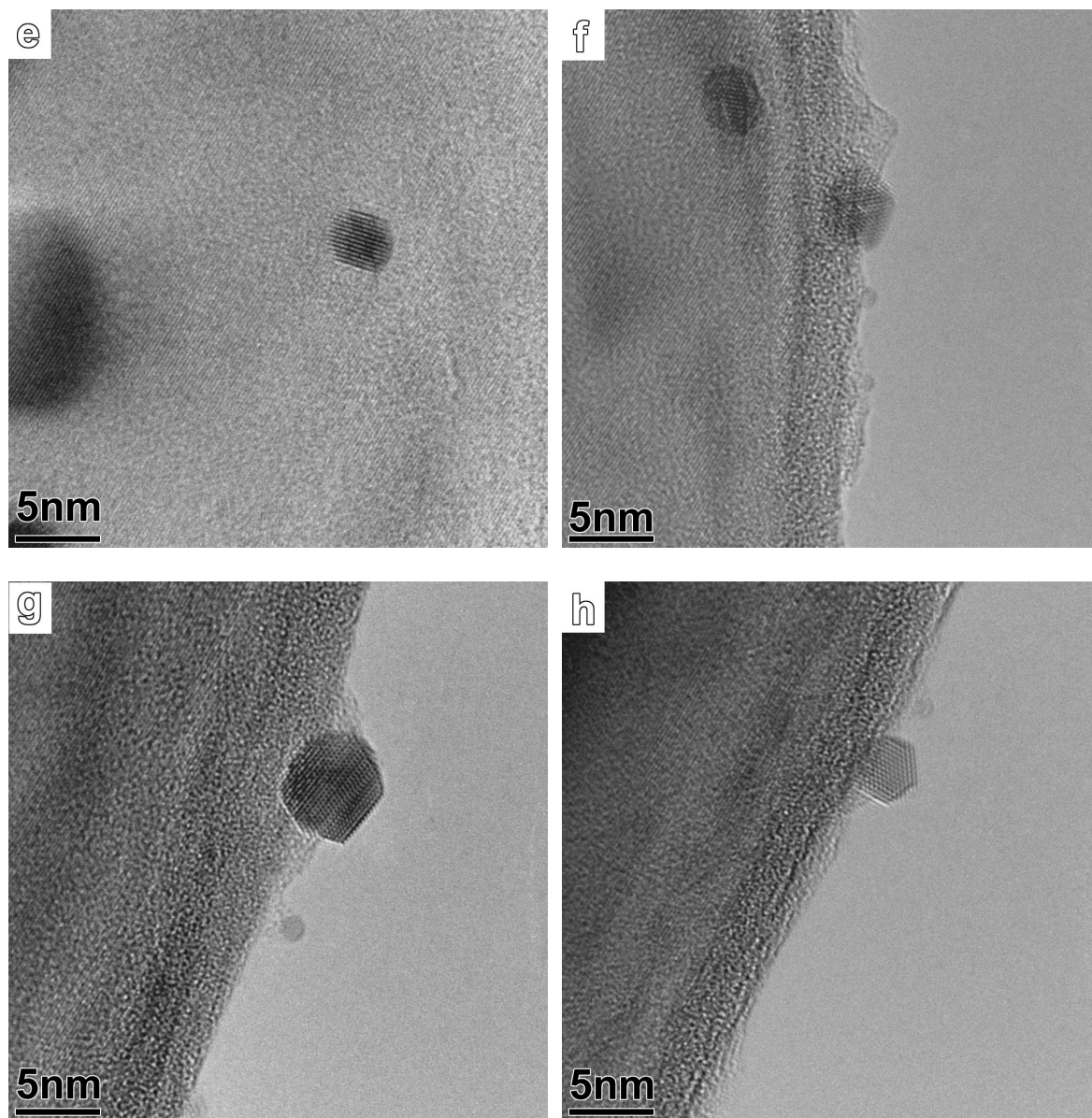


**Figure 5.7** Transmission electron micrographs corresponding to areas (e) – (h) marked on the image in Figure 5.5.

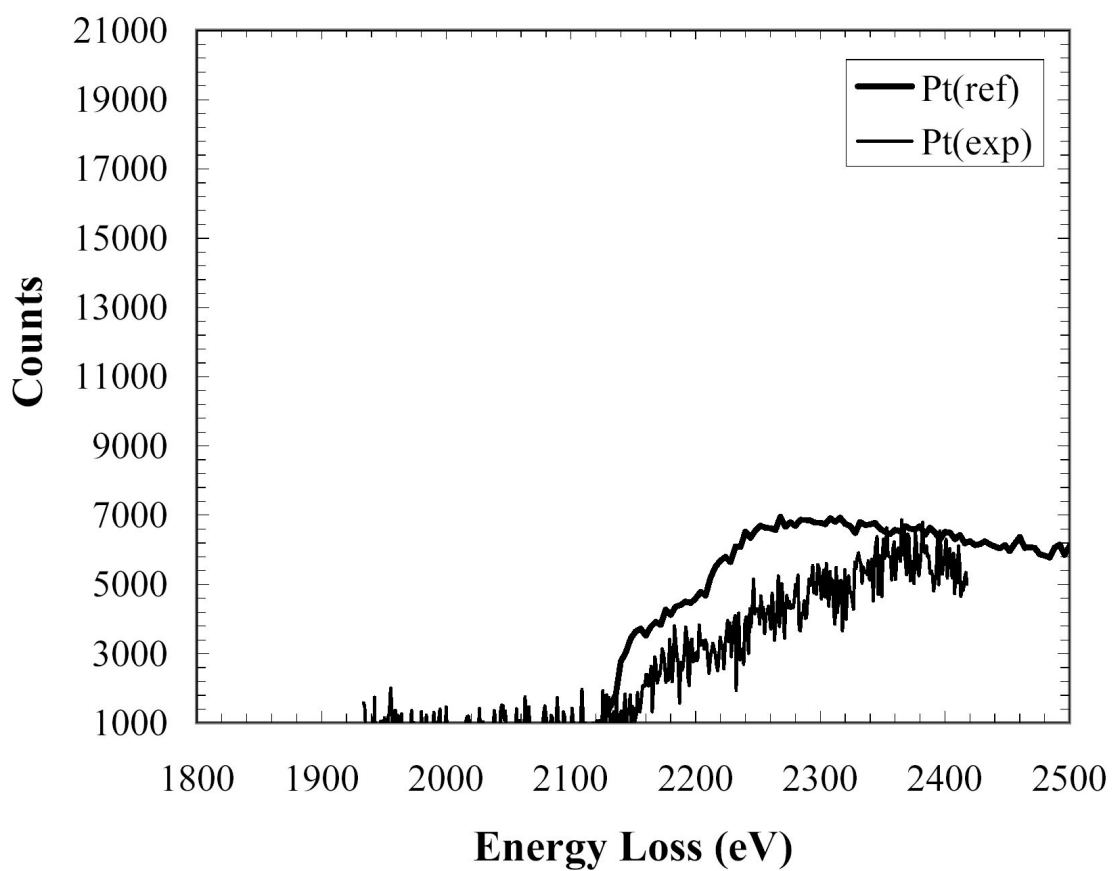


**Figure 5.8** Electron energy loss (core loss) from platinum nanoparticles in Figure 5.5.

Experimental data and reference spectrum are plotted.

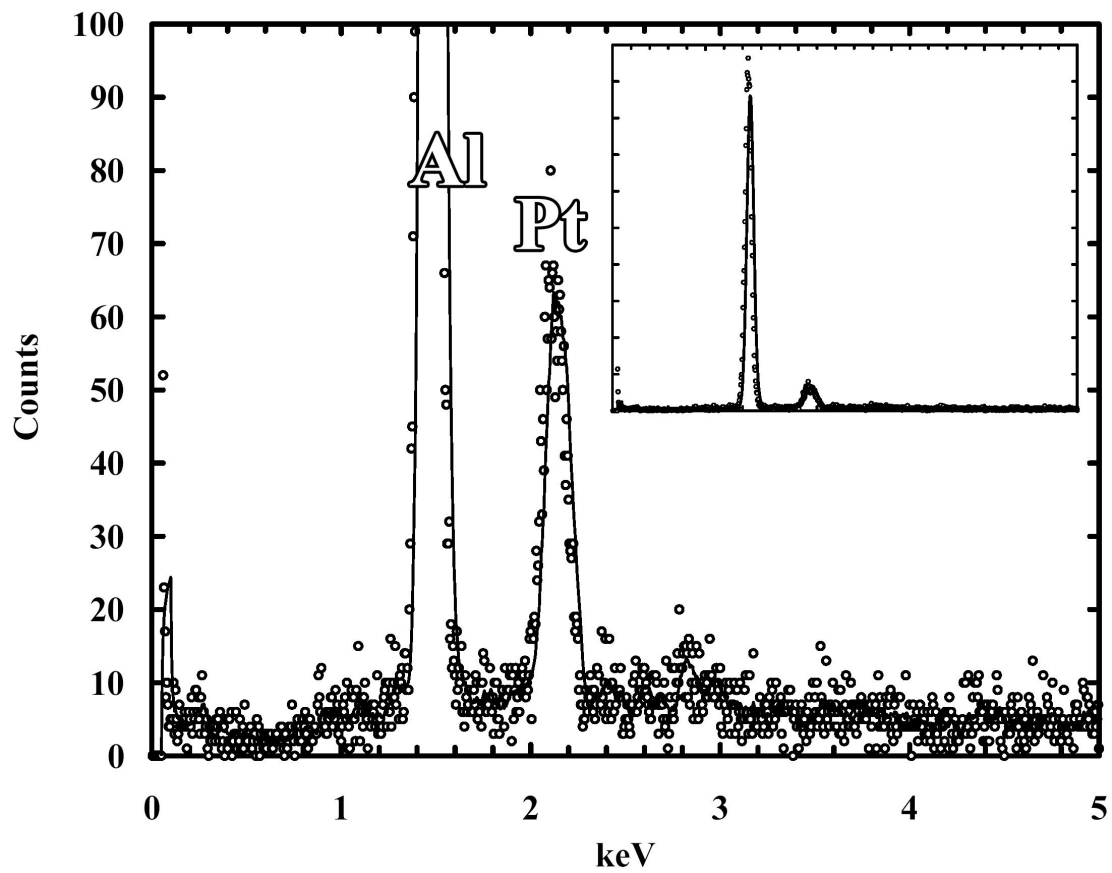


**Figure 5.9** X-ray energy-dispersive spectrum taken from aluminum needle after field emission (sample in Figure 5.5). Presence of platinum is apparent; inset: spectrum normalized to height of aluminum peak. .

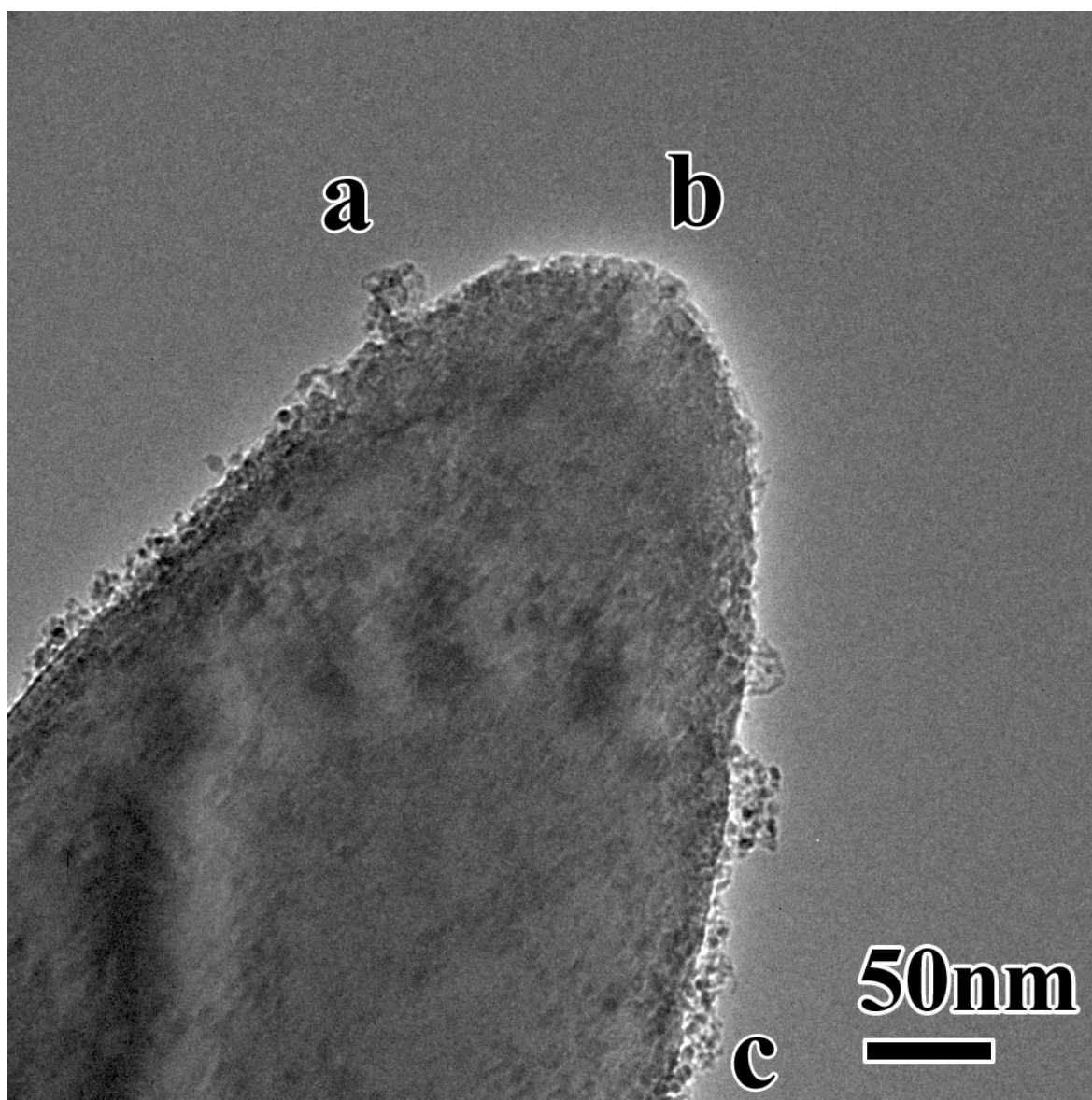


**Figure 5.10** Transmission electron micrograph of aluminum emitter following a second diamond deposition and field emission. Labels indicate areas where higher magnification images were taken, which correspond to the micrographs in Figure 5.11.

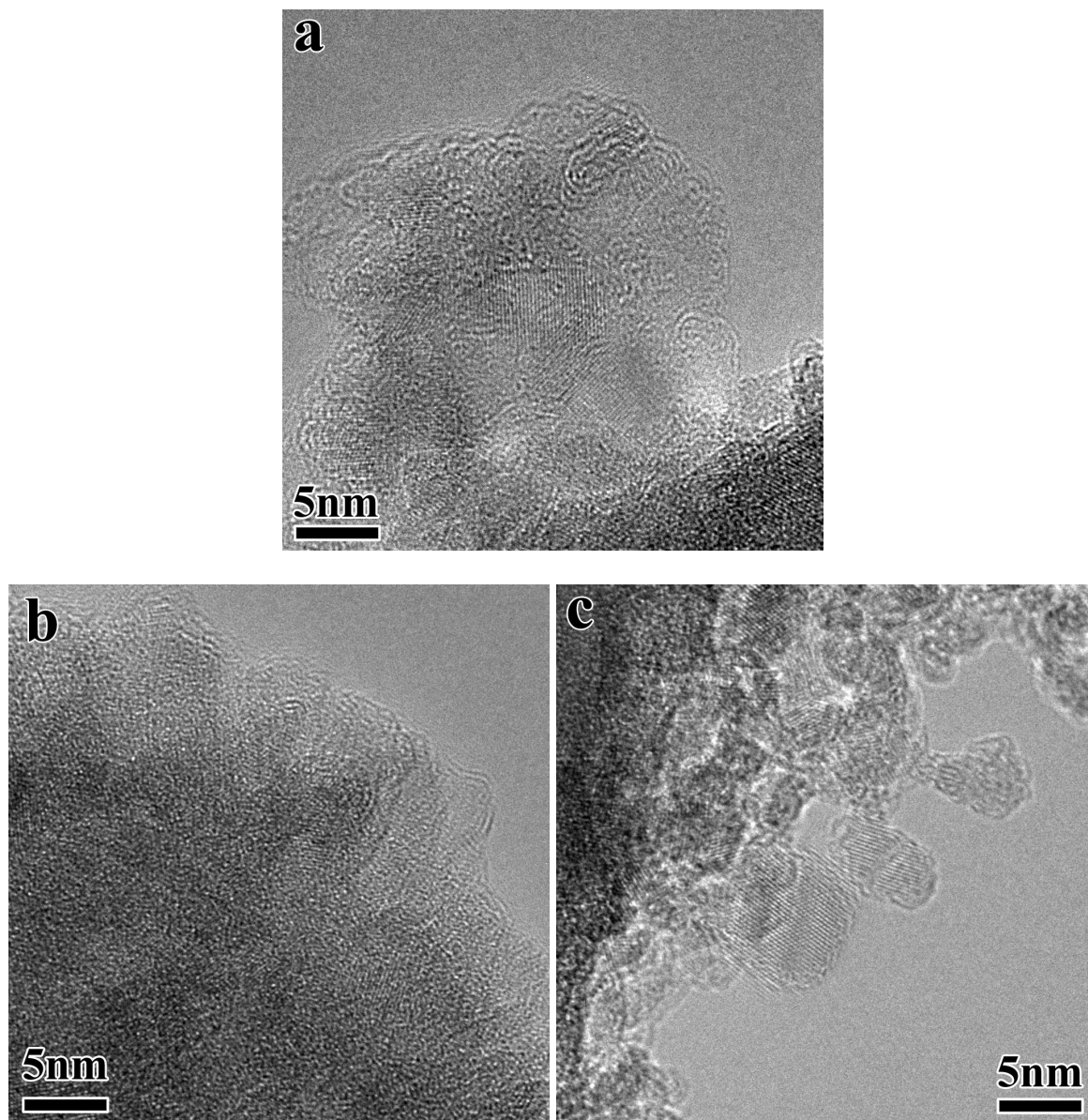


**Figure 5.11** Transmission electron micrographs corresponding to areas (a) – (c) marked on the image in Figure 5.10.

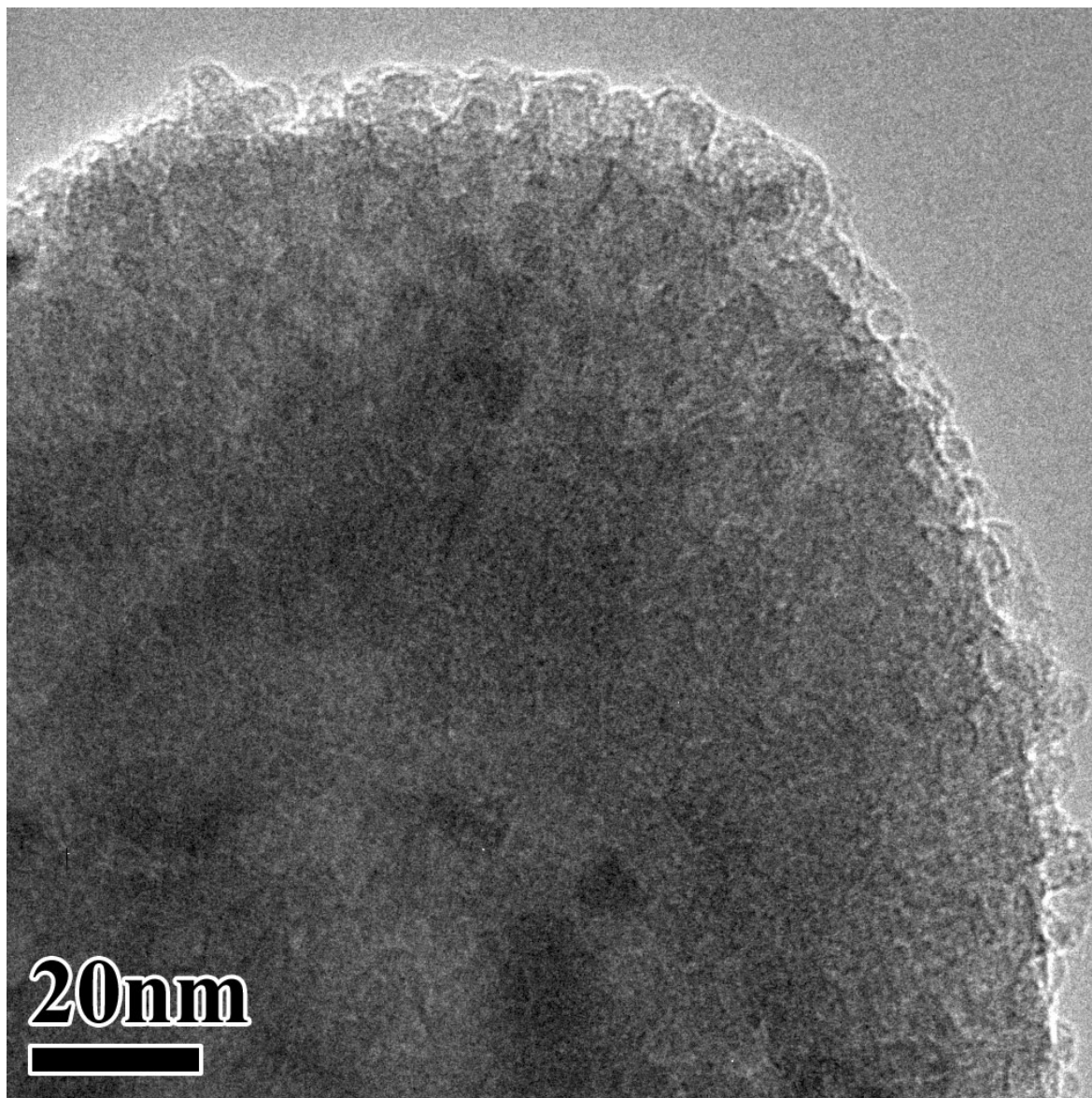


**Figure 5.12** Transmission electron micrograph of the apex of the needle seen in Figure 5.10. The presence of a thin diamond *film* (~6-8 nm) is apparent.

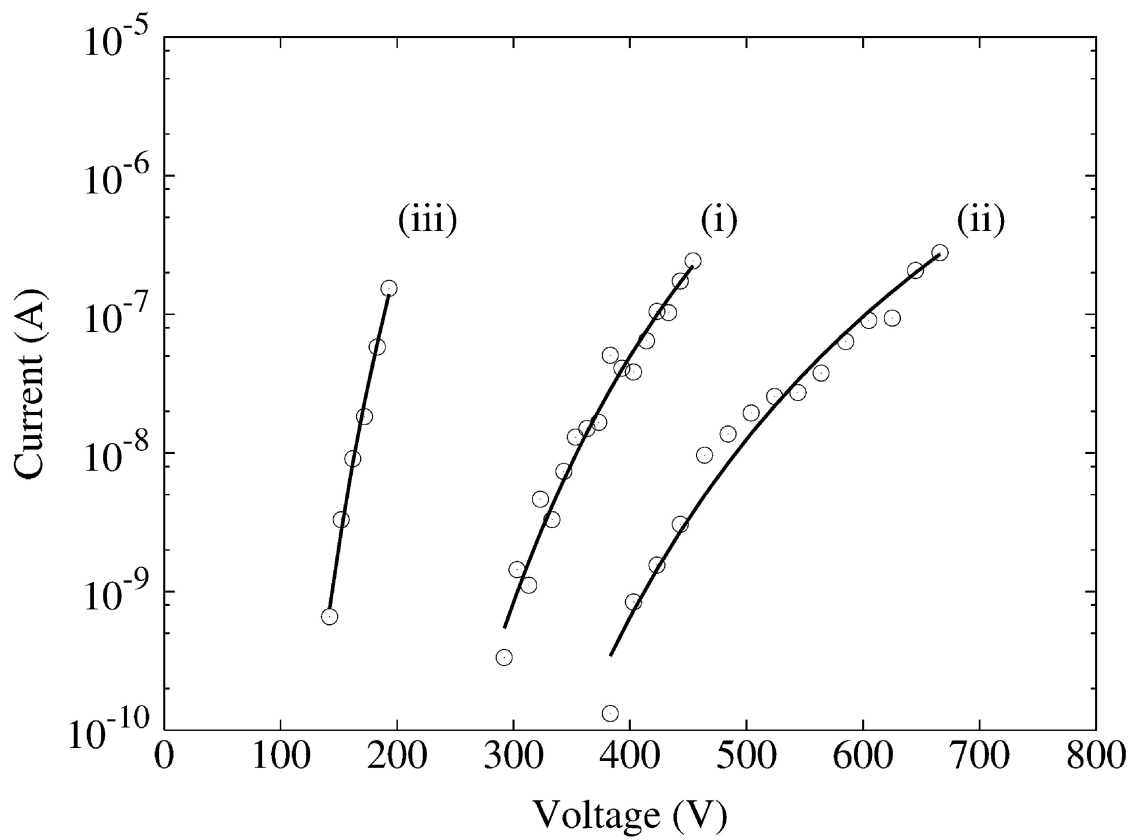
### 5.4.2 Field Emission

Figure 5.13 summarizes a comparison of the three I-V curves from: i) a bare aluminum tip, ii) the same tip after undergoing a single diamond deposition, iii) the same sample after a repeated deposition resulting in a polycrystalline nanodiamond layer of ~ 6-8 nm in thickness. The emission parameters used for this comparison are identical to those used in Chapter 4, with the exception of maximum current, which for aluminum was set at 0.1 microamps (to avoid damage to the aluminum emitter). As was the case for the molybdenum field emission data in the previous chapter, since the current limits are arbitrarily set ( $I_{\max}=0.1\mu\text{A}$ ,  $I_{\min}=1\text{nA}$ ), the use of the *integral transconductance* (equation (4.1)) is meaningful only for qualitative comparisons between similar samples, and should not be considered a universal *figure of merit*.

Comparing the I-V curves of the bare Al tip with the same tip after a single diamond deposition reveals a substantial increase (~34%) in threshold voltage and a decrease (~ 27%) in transconductance. After undergoing a second deposition that resulted in a uniform *film* of diamond (~ 6-8 nm thick), a drastic decrease in threshold voltage was seen (~ 51%, when compared to the bare aluminum emission), as was an increase in transconductance (~ 230%). The emission barrier was also observed to increase (~ 13%) after the initial deposition, and then decrease (~ 30%) upon depositing a second time. A summary of the field emission data and the corresponding Fowler-Nordheim analysis is shown in Table 5.2.

Field emission micrographs were taken at each of the three stages of diamond deposition (Figure 5.14) immediately following field emission current voltage

measurements. The first FEM image, obtained from the bare aluminum emitter (Figure 5.14a), reveals a symmetric pattern typical of a bare metal emitter. The field emission image obtained after the first diamond deposition (Figure 5.14b) is skewed (being off-center suggests emission originated from a point on the emitter that is slightly off axis). The final emission image (Figure 5.14c), obtained from the aluminum emitter coated with a thin diamond *film*, reveals a more uniform emission area that is most intense at the center (the apex of the emitter) [note: the dark pointed feature angled at  $\sim 45^\circ$  toward the center of the image is an artifact, where the phosphor screen was damaged, thus that area would not phosphoresce].



**Figure 5.13** Field emission current voltage measurements taken from an aluminum emitter before and after diamond deposition: i) bare aluminum, ii) single deposition, and iii) two depositions.

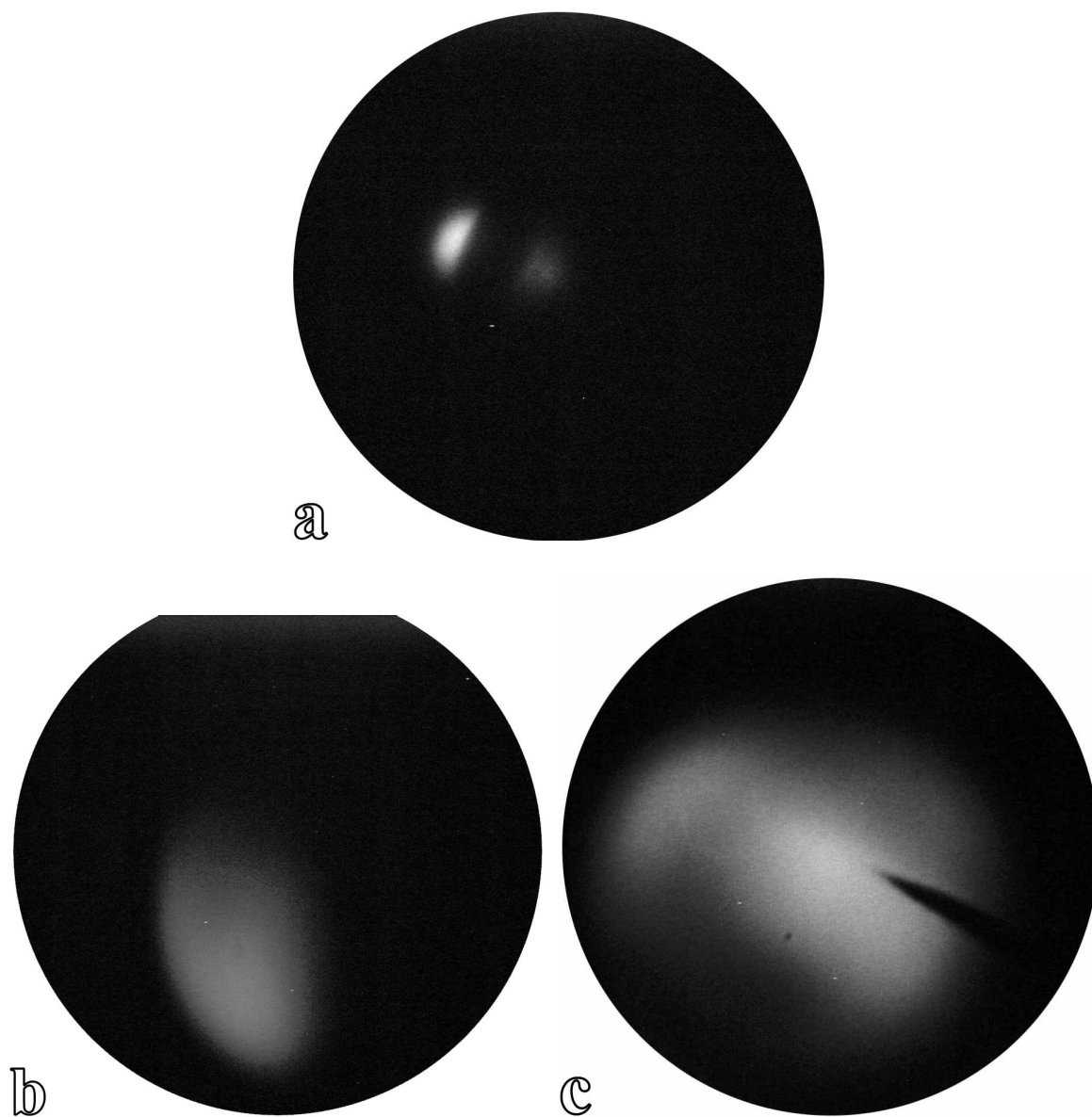


**Figure 5.14** Field emission microscopy images taken from aluminum emitter a) before diamond deposition (Figure 5.1), b) after diamond deposition (Figures 5.3 and 5.5), and c) after a second diamond deposition (Figure 5.12).

**Table 5.2** Geometrical and emission characteristics of aluminum field emitter with varying amounts of nanodiamond.

Characteristics		Bare Al	Particles	ND film
Geometrical	Metal tip radius (TEM)	50 nm	50nm	50 nm
	ND Thickness (TEM)	0 nm	? nm	~6-8 nm
Field Emission	$V_{\text{threshold}}$	265 V	355 V	130 V
	$g$	1.2 nA/V	0.9 nA/V	4.1 nA/V
Fowler-Nordheim Analysis	Work function	4.20 eV	4.74 eV	2.95 eV
	$\sqrt{\alpha}$ (F-N)	1.2 nm	1.0 nm	8.0 nm

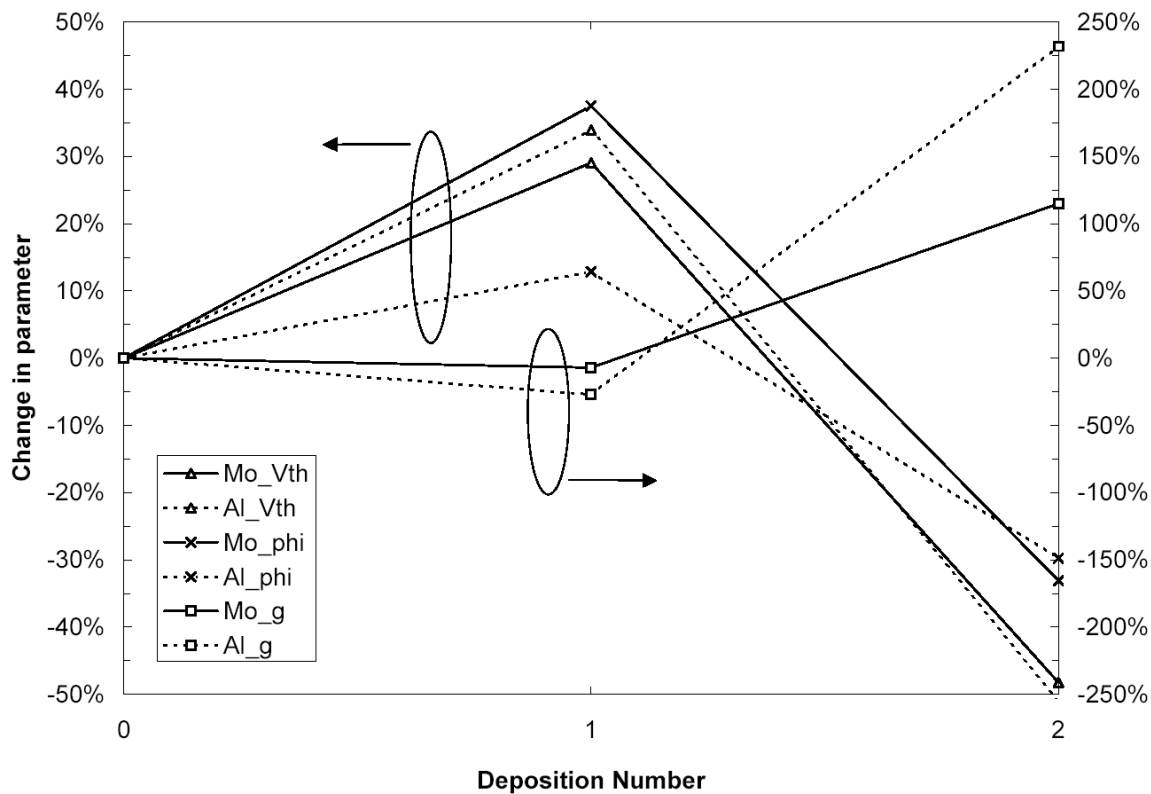


**Figure 5.15** Comparison of change in emission parameters (relative to bare metal emitter) for molybdenum emitter with diamond (data from table 4.1) and aluminum emitter with diamond (data from table 5.2). Depositions are as follows: 0 = bare metal emitter, 1 = single diamond coating (isolated nanoparticle(s)), and 2 = thin diamond *film*. Emission parameters considered are: threshold voltage (“Vth”), emission barrier (“phi”), and integral transconductance (“g”).

## 5.5 DISCUSSION

### 5.5.1 Transmission Electron Microscopy

High-resolution transmission electron microscopy did not reveal any measurable changes in the emitter geometry, which could account for the observed changes in emission, e.g. no atomic-scale protrusions were observed. While platinum nanoparticle contaminants (resulting from the electrochemical etching of aluminum using a platinum electrode, see Appendix) were observed on the aluminum emitter, their presence cannot explain the changes in emission behavior, as the particles were present on the emitter prior to any diamond deposition, and any effect the platinum may have had would have been observed in the initial field emission experiments.

### 5.5.2 Field Emission

The observed changes in field emission behavior due to the addition of diamond to the emitter surface are nearly identical to those observed for molybdenum. Figure 5.15 summarizes the effects of each deposition on various emission parameters (threshold voltage, emission barrier, and integral transconductance) for both the aluminum emitter and the molybdenum emitter (Chapter 4). As was the case for molybdenum coated with diamond, the emission from aluminum deposited with isolated diamond particles was suppressed (compared to that of the bare aluminum emitter). Upon additional diamond deposition (i.e. the formation of a thin *film*), field emission drastically increased (i.e. a decrease in threshold voltage, and increase in transconductance). The similarity in emission behavior observed for diamond-coated aluminum to that of molybdenum suggests a similar mechanism is responsible. It is thus suggested that an increase in

surface barrier height (see section 4.5.4) and a decrease in emission area (see section 4.5.5) are the responsible mechanisms for the observed emission behavior.

## 5.6 CONCLUSION

Electron emission from a multi-particle nanodiamond coating and isolated diamond nanoparticles has been measured. Field emission current-voltage data was taken at each stage of diamond deposition, as were field emission micrographs and transmission electron micrographs. The emission characteristics were a complex function of coating thickness. Field emission micrographs reveal emission site changes (origin of emitted electrons on emitter surface) for increasing amounts of deposited diamond. Current-voltage curves shifted to a considerably higher voltage than for the metal substrate for the initial coating. However, for a thicker film of ~6-8 nm, with nearly uniform nanoparticle coverage, the I-V plot was sharply shifted to a voltage much lower than that for the uncoated metal substrate. Similar field emission behavior was observed with diamond-coated molybdenum in earlier experiments and attributed to an emission barrier increase (due to quantum confinement effects) and a decrease in emission area (due to electrostatic effects); the same model is attributed to the emission behavior observed from the diamond-coated aluminum in this series of experiments.

Future work to include emission measurements from single isolated nanodiamond particles of varying size could lead to more insight concerning the emission mechanism, and could support the proposed model of bandgap increase and electrostatic screening. Additional experiments using the same samples with isolated diamond in contact mode in a

scanning tunneling microscope could provide complimentary electrical measurements, as could field emission energy distribution measurements and field emission microscopy.

## 5.7 REFERENCES

- 1 R. Gomer, *Field Emission and Field Ionization*. 1961, New York: Originally published by Harvard Univ. Press, Cambridge. Reprinted by American Institute of Physics, 1993.
- 2 I. Brodie and C. A. Spindt, *Vacuum Microelectronics*. Advances in Electronics and Electron Physics. Vol. 83. 1992: Academic Press. 1-106.
- 3 I. Brodie and C. A. Spindt, *Vacuum Microelectronics*. Advances in Electronics and Electron Physics. Vol. 83. 1992: Academic Press. 1-106.
- 4 C. A. Spindt, I. Brodie, L. Humphrey, and E. R. Westerberg, *Physical Properties of Thin-Film Field Emission Cathodes with Molybdenum Cones*. Journal of Applied Physics **47**(12) 5248 (1976).
- 5 Ch. Renner, Ph. Niedermann, and Ø. Fischer, *Enhanced Field Emission Investigation of Aluminum*, IEEE Transactions on Electrical Insulation **24** (6) 911-916 (1989).
- 6 Ming-Chi Kan, Jow-Lay Huang, J. C. Sung, Ding-Fwu Lii, and Bao-Shun Yau, *Field emission of micro aluminum cones coated by nano-tips of amorphous diamond*, Diamond and Related Materials **12** 1610-1614 (2003).
- 7 C. Lizzul-Rinne, *Electrodeposition of Lead, Tin, and Lead-Tin Alloys and Their Electronic Applications*, Ph.D. Thesis, N.C. State University (1999).
- 8 I. E. Campbell, *High Temperature Technology*, Electrochemical Society, John Wiley and Sons, New York, USA, 1956.

- 9 G. V. Samsonov (Ed.), *Handbook of the Physicochemical Properties of the Elements*, IFI-Plenum, New York, USA, 1968.
- 10 W. D. Callister Jr., *Materials Science and Engineering – An Introduction*, 3<sup>rd</sup> edition, New York, USA, John Wiley and Sons, 1994.
- 11 M. T. Saif, S. Zhang, A. Haque, and K. J. Hsia, *Effect of native Al<sub>2</sub>O<sub>3</sub> on the elastic response of nanoscale Al films*, *Acta Materialia* **50** 2779-2786 (2002).
- 12 N. G. Chechenin, J. Böttiger, and J. P. Krog, *Nanoindentation of amorphous aluminum oxide films*, *Thin Solid Films* **304** 70-77 (1997).

## CHAPTER 6

### SUMMARY, CONCLUSIONS, AND FUTURE WORK

#### 6.1 SUMMARY AND CONCLUSIONS

The primary objective of this research, to isolate and characterize diamond nanoparticles on *needle-shaped* metal substrates, was demonstrated. Electrochemically etched needles, the *tools* with which nanodiamond was isolated for study, allowed for a number of non-destructive techniques to be used to characterize the diamond nanoparticles. The composition and morphology of the diamond nanoparticles and metal substrates were determined using a number of techniques, including scanning and transmission electron microscopy, electron energy loss spectrometry, and x-ray energy dispersive spectroscopy. Field emission measurements were also taken from emitters coated with varying amounts of diamond, as were field emission micrographs. The geometry of the metal substrates used (i.e. *needles*) allowed for field emission and field emission microscopy to be performed before and after microstructural analysis and imaging (EDS, EELS, HRTEM), as all the techniques used were non-destructive.

The suppression of field emission due to the presence of a single isolated diamond nanoparticle on the tip of a molybdenum field emitter compared to that of a more uniformly-coated emitter suggests that there is a size dependent effect contributing to emission suppression. It is suggested that quantum confinement, leading to an increase in

the bandgap of the diamond, may contribute to emission suppression for particles less than ~5nm in size. Computer simulations strongly suggest that electrostatic effects, resulting from the small dimensions and morphology of the isolated diamond nanoparticle, appear to further suppress emission by reducing the electric field in the vicinity of the diamond particle: at the metal-vacuum interface, within the particle itself, and at the metal-diamond interface.

The experiments conducted using aluminum as a substrate indicate aluminum needles may be well suited for field emission as well as for serving as *tools* with which to study a variety of nanometer sized particles. Field emission current-voltage measurements were taken and field emission micrographs were obtained, using an electrochemically sharpened aluminum needle as the substrate, with varying deposits of nanodiamond particles. Transmission electron microscopy, electron energy loss spectrometry, and x-ray energy dispersive spectroscopy were used to characterize the diamond and aluminum substrate.

Emission behavior similar to that of the series of experiments conducted with molybdenum were observed, namely suppression of emission with isolated particles on the emitter surface, followed by emission enhancement when a thin layer of diamond particles were deposited.

## **6.2 SUGGESTED FUTURE WORK**

### **Nanodiamond Characterization**

The size-dependent effects used to describe the observed field emission behavior of diamond on molybdenum and aluminum should be further studied using a series of

samples with diamond particles of varying sizes. Such experiments should be used to determine the effect of particle size on emission, and test the suggested model for emission suppression. Simultaneous field emission energy distribution measurements from the isolated diamond particles of various sizes would also help determine the mechanism responsible for emission and the nature of size-dependent emission behavior. Field emission microscopy can also be employed to observe which emission sites are contributing to the total emission current.

Additional electrical measurements can be made on isolated nanoparticles using a scanning-tunneling microscope (STM) in the contact-mode; current-voltage curves using this configuration could offer further insight into the electrical properties of diamond nanoparticles including conductivity and the nature of surface states of nanodiamond [e.g. 1, 2]. Size-dependent measurements could be made on the same samples used for field emission experiments for complementary data. The conductivity of nanodiamond particles could be determined as well as its dependence on particle size.

### **Platinum Nanoparticle Formation**

The observed deposition of platinum on etched aluminum needles and the subsequent formation of platinum nanoparticles following field emission needs further study. A mechanism for the platinum deposition has been proposed, and supported by the experiments conducted to date. However, further studies, e.g. spectroscopy to determine if chlorine ions are present in the etching solution (a necessary condition for the proposed platinum-deposition mechanism), are also needed. The apparent formation of platinum nanoparticles during field emission has been suggested, but needs additional experimental confirmation. Field emission microscopy imaging during the initial *break in* period

performed on field emitters could indicate whether field-induced migration of platinum on the aluminum surface results in platinum nanoparticle formation. Additionally, a series of transmission electron microscopy experiments, using a sample holder capable of applying an electric field in-situ [e.g. 3], where a sample is repeatedly imaged and subjected to an (increasingly intense) electric field could be used to study the formation of the platinum nanoparticles and thereby help determine the mechanism responsible for their formation.

### 6.3 REFERENCES

- 1 M. Cannaefts, M. Nesladek, Z. Remes, C. Van Haesendonck, and L. M. Stals, *Scanning Tunneling Microscopy and Spectroscopy of Non-Doped, Hydrogen Terminated CVD Diamond*, *Physica Status Solidi A*, **181** 77-81 (2000).
- 2 M. Enachescu, D. Schleef, D. F. Ogletree, and M. Salmeron, *Integration of Point-Contact Microscopy and Atomic-Force Microscopy: Application to Characterization of Graphite/Pt(111)*, *Physical Review B* **60** (24) 16913-16919 (1999).
- 3 Z. Xu, X. Tan, P. Han, and J. K. Shang, *In situ transmission electron microscopy study of electric-field-induced microcracking in single crystal  $Pb(Mg_{1/3}Nb_{2/3})O_3 - PbTiO_3$* , *Applied Physics Letters* **76** (25) 3732-3734 (2000).

## APPENDIX

### PLATINUM DEPOSITION ON ALUMINUM

#### A.1 INTRODUCTION

The presence of platinum on the surface of the etched aluminum needle (section 5.4) suggested platinum deposition was occurring during sample preparation. The only source of platinum during sample preparation was the electrode used during electrochemical etching. A mechanism for platinum deposition is proposed, which consists of: 1) the dissolution of platinum in solution, forming the  $\text{PtCl}_6^{2-}$  complex and 2) the plating out of the  $\text{Pt}^{4+}$  ion during the negative half-cycle of the AC etching process. As such, the platinum should thus only be deposited while the aluminum wire serves as the cathode (i.e. the negative half-cycle). Furthermore, any platinum deposited during the cathodic half-cycle would be removed during the anodic cycle, this being when aluminum etching occurs. The deposition of platinum under the above model does not account for the presence of platinum *particles*; it is suggested that the electroplated platinum on the aluminum needle later undergoes surface migration during field emission experiments (due to the high electric field present), forming nanoparticles of platinum; however, no specific experiments were conducted to confirm this, as determining the source of the platinum to avoid its presence was sufficient for this research. To determine if the proposed mechanism was responsible for platinum deposition, a set of samples was etched with

varying conditions: AC, *pulsed* DC (half-wave rectified AC), and AC followed by *pulsed* DC, and then analyzed using x-ray energy dispersive spectroscopy.

## A.2 RESULTS AND DISCUSSION

The aluminum wires etched under varying conditions were examined in the SEM using EDS to determine if platinum was deposited. The results of the various etching conditions were as follows:

- AC etched wire (identical etching conditions as Al needle in section 5.4)
  - Presence of platinum is apparent in the EDS spectrum (Figure A.1). Cl present due to insufficient rinsing after etching. Cu and Zn are x-rays from sample holder in SEM chamber.
- *Pulsed* DC etched wire (Figure A.2)
  - Though the DC etch progressed at a much slower rate, as apparent by blunt appearance of wire in the scanning electron micrograph in Figure A.2, etching did occur.
  - There was no platinum present, as indicated by the two EDS spectra Figures A.4 and A.5; the corresponding areas from which the spectra were taken are indicated in Figures A.2 and A.3, respectively.
- AC followed by *pulsed* DC etched wire (Figure A.6):

- The use of AC was intended to provide faster etching, while the final *pulsed* DC etch was intended to remove more aluminum (although much more slowly) and any platinum which may have been deposited. The AC/DC etch (Figure A.6) resulted in a much sharper sample than the DC etch alone (Figure A.2).
- No platinum was detected as indicated by the EDS spectrum in Figure A.7.

A summary of the etching conditions and corresponding platinum deposition is given in Table A.1. The deposition of platinum onto aluminum during the etching process appears to be due to the mechanism suggested above, and can easily be circumvented using *pulsed* DC etching, or more practically (due to the slow rate of etching for DC biasing) a combination of AC and *pulsed* DC etching.

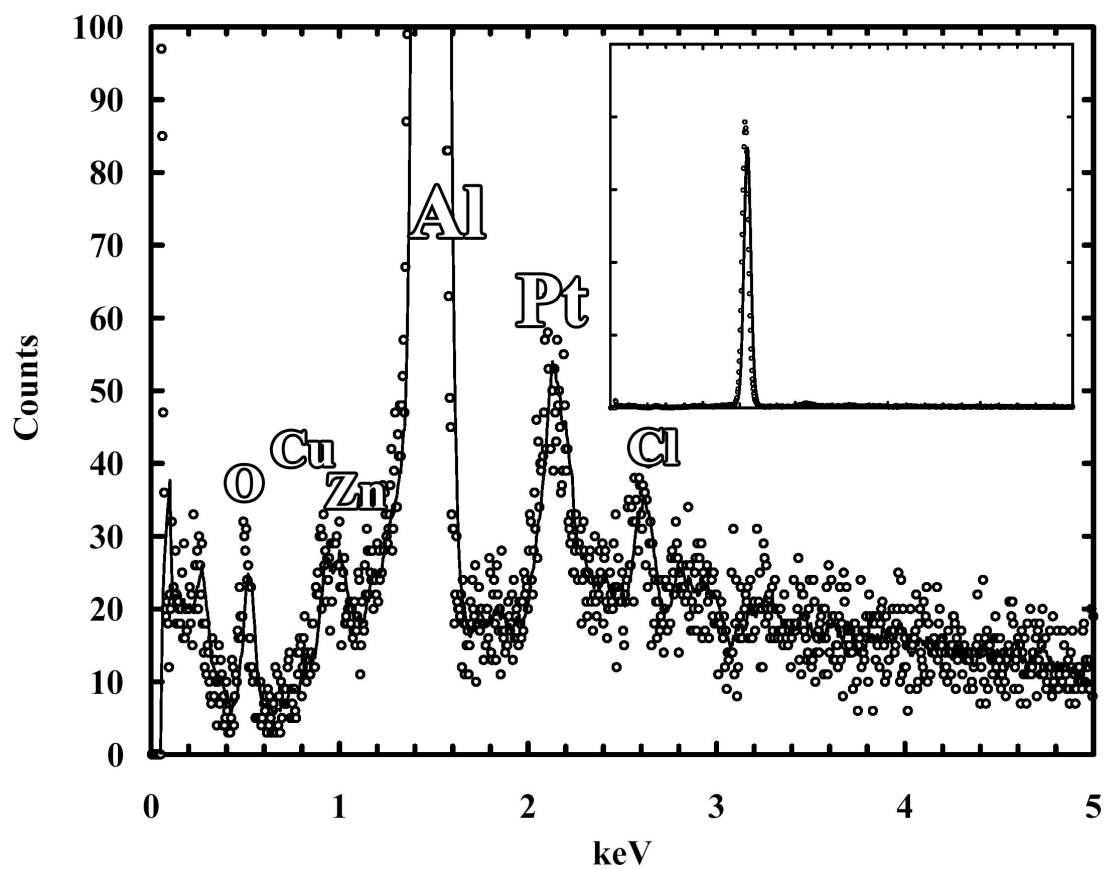


**Figure A.1** X-ray energy-dispersive spectrum taken from an *as prepared* aluminum needle (electrochemically etched, with no field emission or diamond deposition). Presence of platinum is apparent; inset: spectrum normalized to height of aluminum peak. .

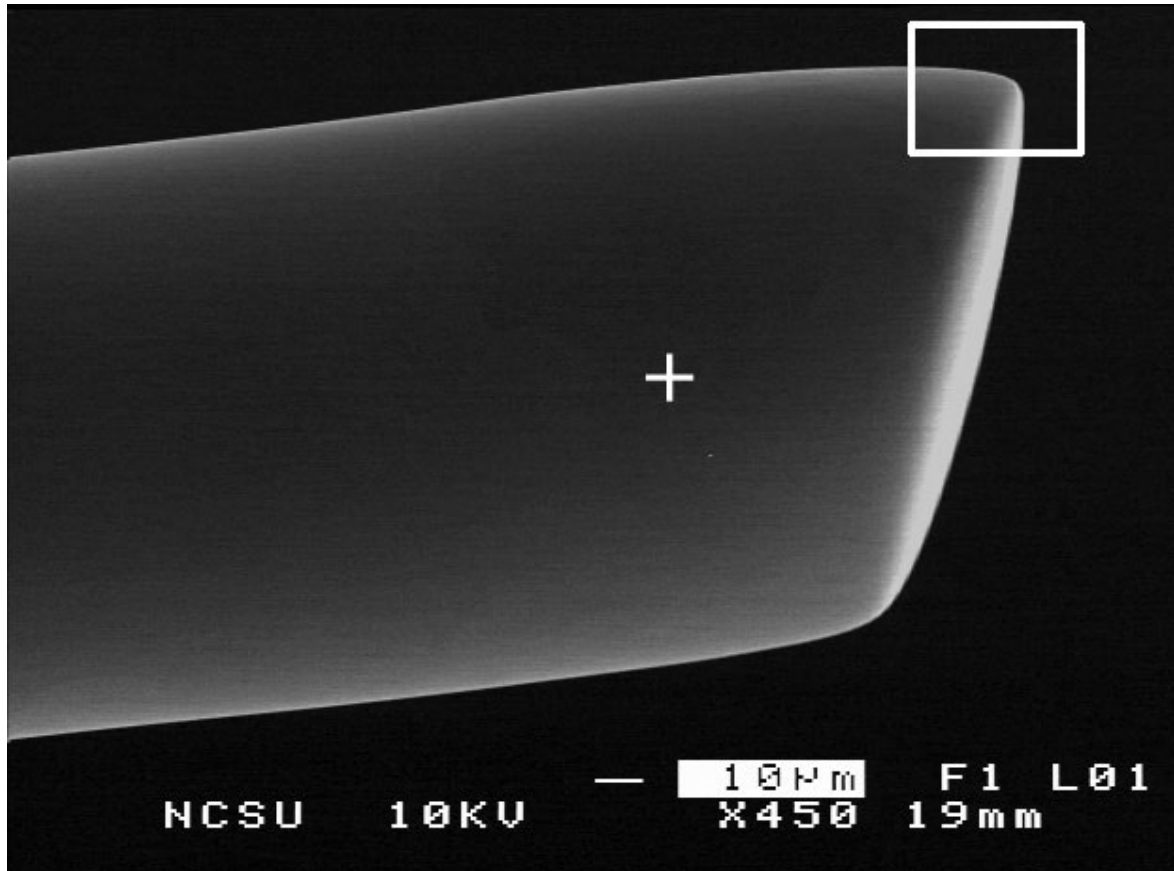


**Figure A.2** Scanning electron micrograph of *pulsed DC-etched* (AC bias half-wave rectified) aluminum wire. The “+” symbol indicates region from which energy dispersive x-ray spectrum was taken (Figure A.4), region enclosed by rectangle indicates where higher magnification image was taken (Figure A.3).

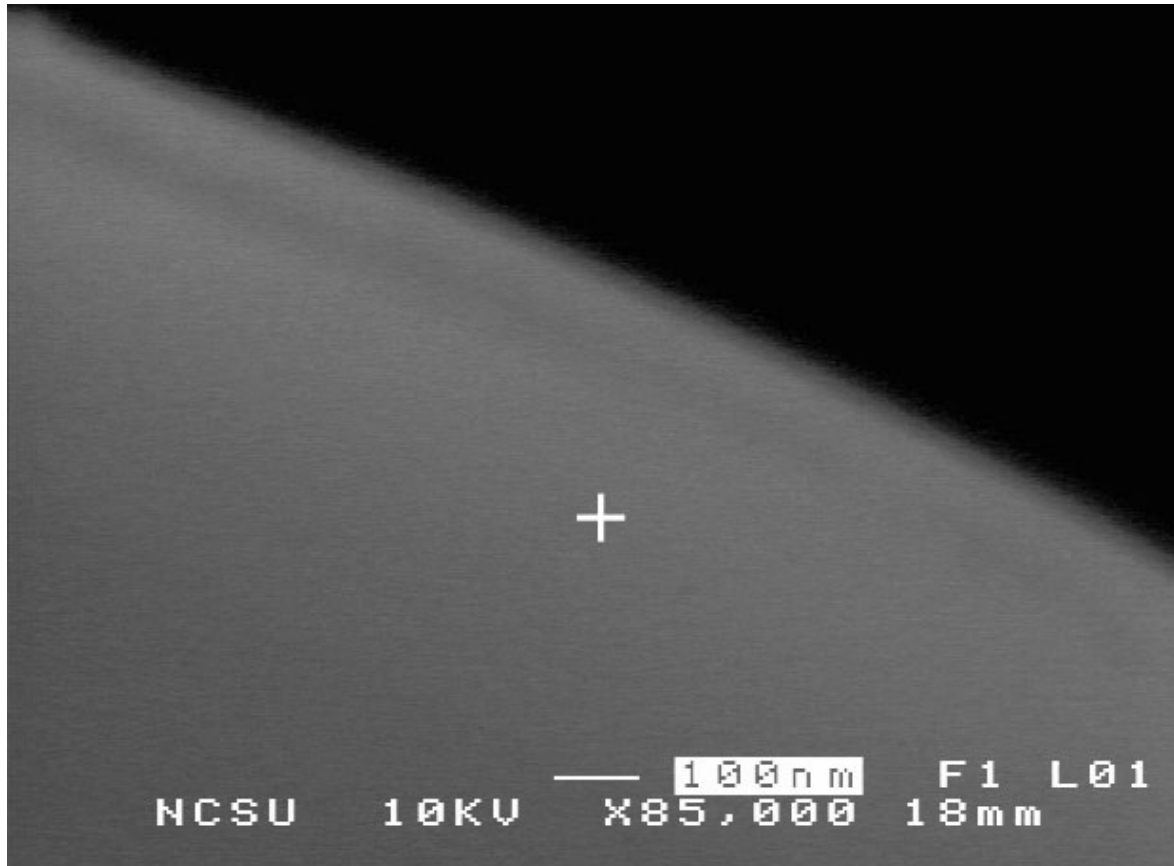


**Figure A.3** Scanning electron micrograph of region denoted in Figure A.2. The “+” symbol indicates region from which energy dispersive x-ray spectrum was taken (Figure A.5).

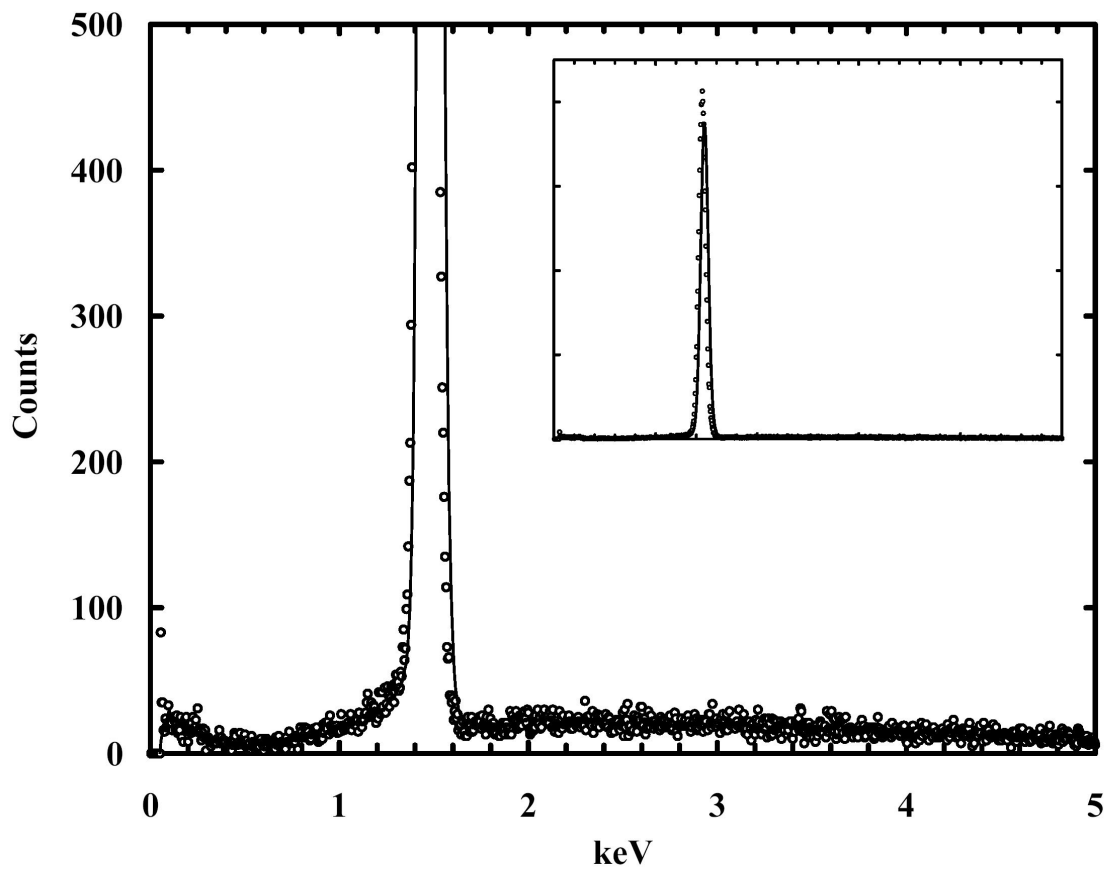


**Figure A.4** Energy dispersive x-ray spectrum taken from region marked by “+” in Figure A.2, aluminum peak (1.5 keV) is the only feature observed. Vertical axis is scaled to illustrate the absence of a weak platinum peak; inset: spectrum normalized to height of aluminum peak.

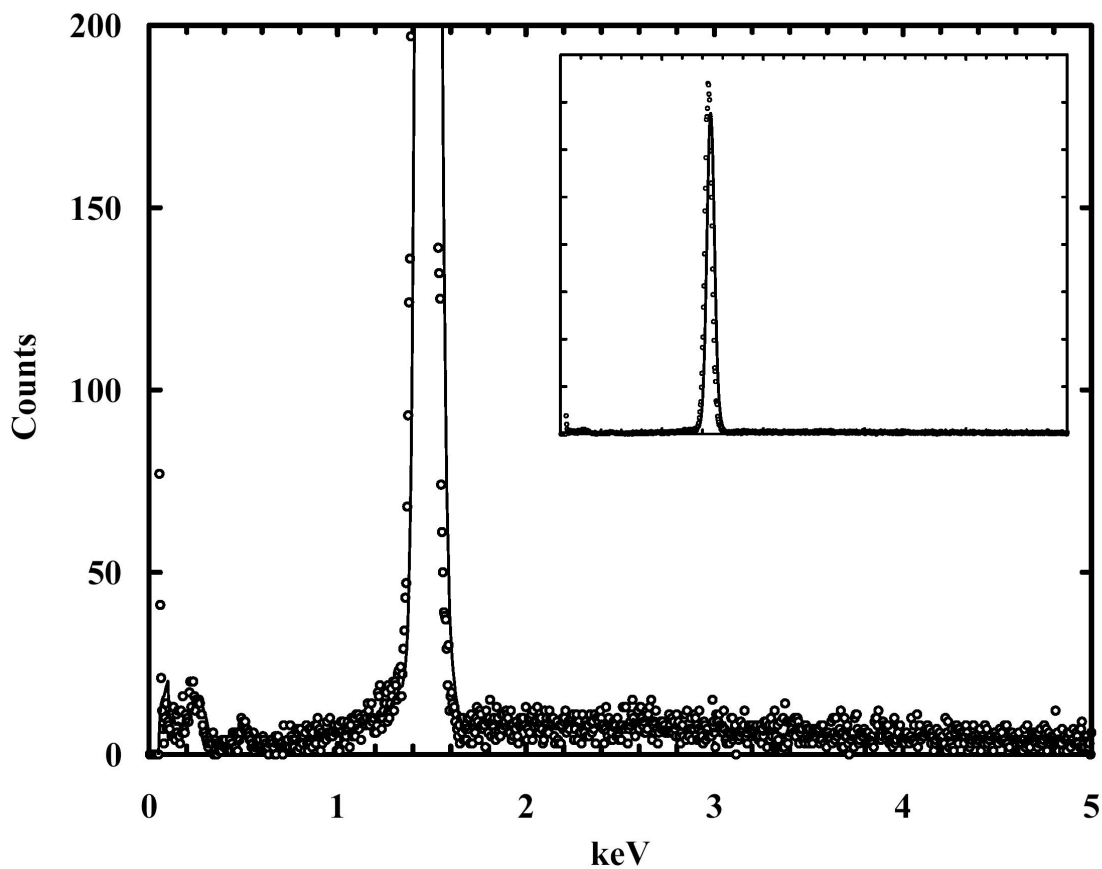


**Figure A.5** Energy dispersive x-ray spectrum taken from region marked by “+” in Figure A.3, aluminum peak (1.5 keV) is the dominant feature; a very weak oxygen peak (0.5 keV) from aluminum-oxide is also seen. Vertical axis is scaled to illustrate the absence of a weak platinum peak; inset: spectrum normalized to height of aluminum peak.

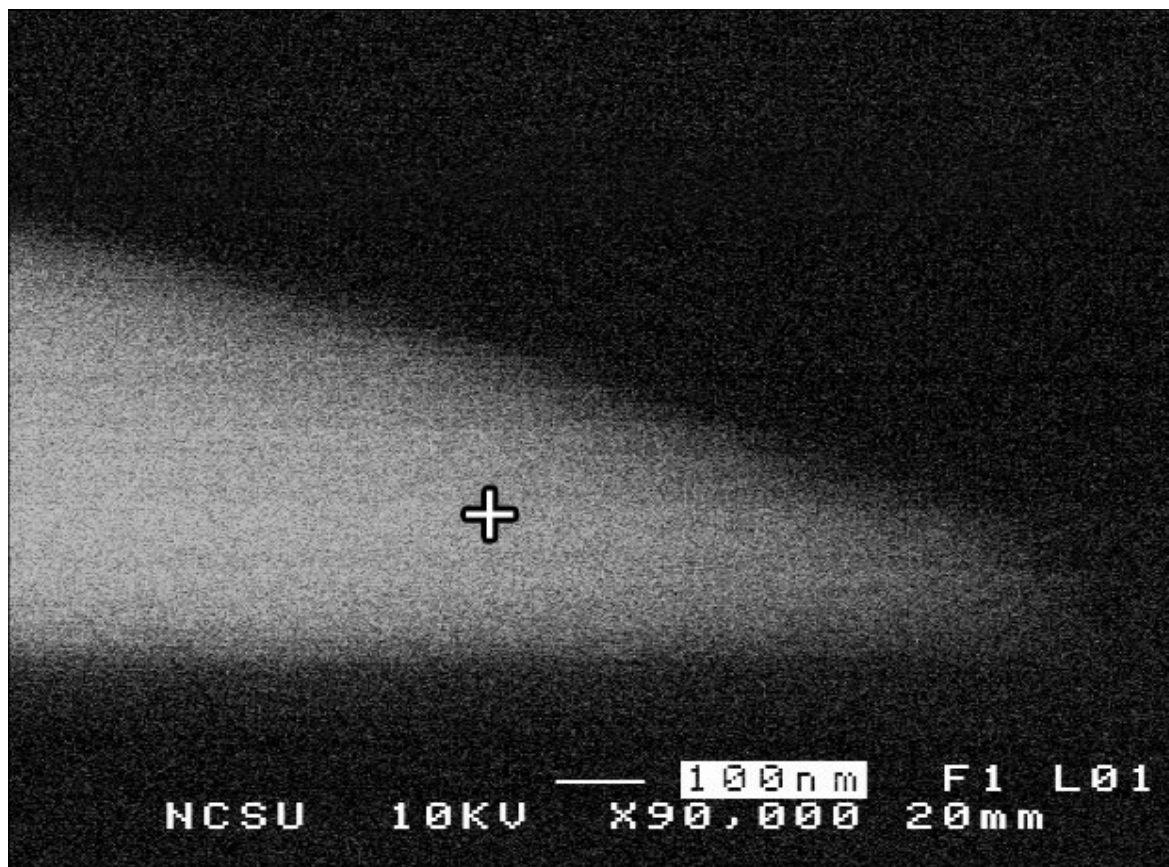


**Figure A.6** Scanning electron micrograph of aluminum wire electrochemically etched using *AC* bias followed by a *pulsed DC* etch (half-wave rectified). The “+” symbol indicates region from which energy dispersive x-ray spectrum was taken (Figure A.7).

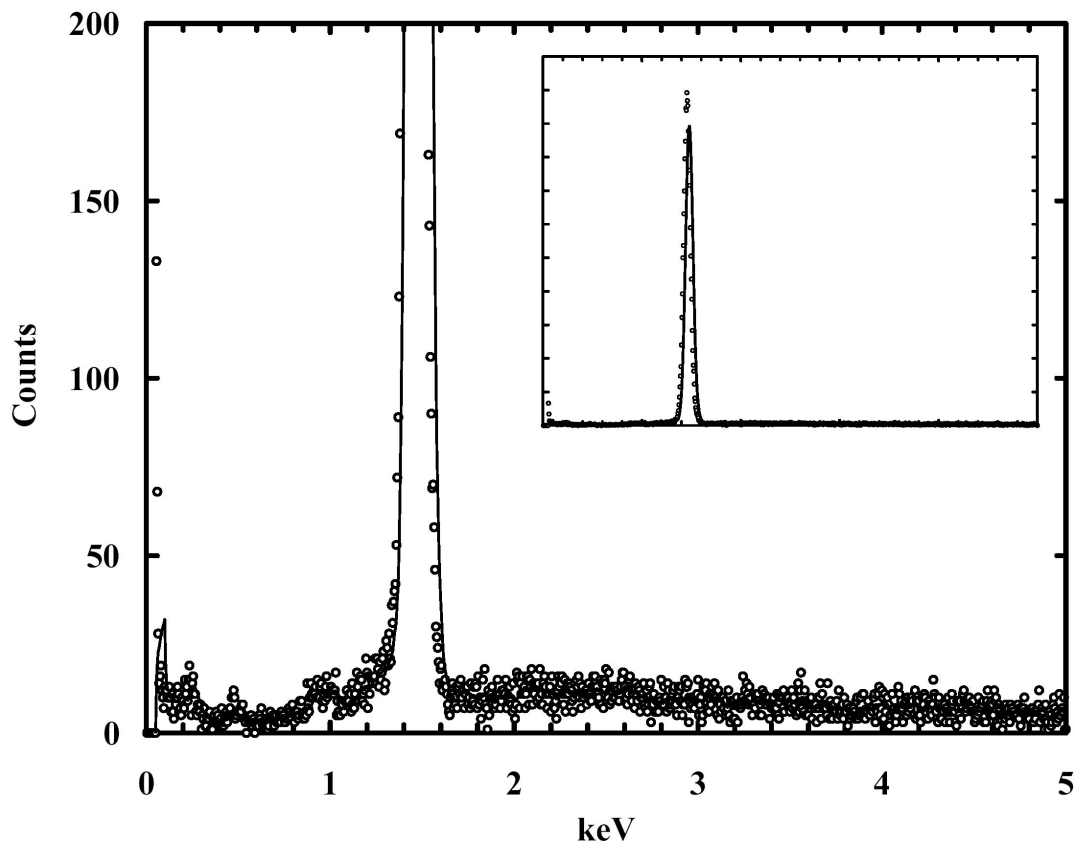


**Figure A.7** Energy dispersive x-ray spectrum taken from region marked by “+” in Figure A.6, aluminum peak (1.5 keV) is the dominant feature; a very weak oxygen peak (0.5 keV) from aluminum-oxide is also seen. Vertical axis is scaled to illustrate the absence of a weak platinum peak; inset: spectrum normalized to height of aluminum peak.

**Table A.1** Summary of aluminum etching conditions and corresponding platinum deposition onto aluminum.

<b>Etching Conditions</b>	<b>Platinum Present</b>
AC (15-20 V)	Yes
<i>Pulsed</i> DC (1/2 wave rectified AC)	No
AC followed by <i>Pulsed</i> DC	No